TU Delft

Master Thesis

Simulations and experiments on coplanar waveguide resonators intersected by capacitively shunted Josephson junctions

A thesis submitted in fulfillment of the requirements for the degree of Master of Science

in the

Steele Lab
Quantum Nanoscience

Author:
Tim van de Veen

Supervisors:
Marios Kounalakis, MSc
prof. dr. Gary Steele

February 9, 2019

TU DELFT

Abstract

Faculty of applied sciences
Quantum Nanoscience

Master of Science

Simulations and experiments on coplanar waveguide resonators intersected by capacitively shunted Josephson junctions

by Tim van de Veen

A single photon interacting with a single atom is the most fundamental form of light interacting with matter and has been extensively studied in the field of Cavity Quantum Electrodynamics (cavity QED). Here, a non-linearity like an atom is coupled to a single mode of the electromagnetic field in a cavity. Another field which explores the quantum mechanical nature of photons is Circuit Quantum Electrodynamics (cQED) where photons are the quantized excitations of a superconducting microwave resonator and non-linearity is introduced by the Josephson junction. Like this, setups analog to that of in cavity QED can be copied to cQED, with a number of differences. For example, the photons propagating in a transmission line are more confined and the circuits are made with conventional lithography techniques, allowing for more freedom in engineering the system parameters.

In the first part of the thesis, we build a numerical model in order to examine the feasibility of quenching the ground state of a coplanar waveguide (CPW) interrupted by a tunable coupling element. Next, by means of experiments and simulations we considered the feasibility of observing experimentally a synchronization effect in a driven CPW with its central conductor interrupted by equally spaced capacitively shunted Josephson junctions (Josephson crystal) based on a recent proposal. Finally, we made a first step in understanding the synchronization from a classical perspective by modelling a Josephson crystal of two junctions as two degenerate non-linearly coupled Duffing oscillators.

Concerning the quenching experiment, we found that the plasma frequency must be tuned faster than 1/f with f the resonance frequency of the CPW, which is in the sub-nanosecond regime and therefore unfeasible with current state the art electronics. We also found that, in contrast to what was claimed in the proposal, the synchronization effect cannot be observed for the parameters common in cQED. One way would be to push the limits of the capacitances to several picofarads. Finally, we found that the non-linear coupling causes the two degenerate non-linearly coupled Duffing oscillator to synchronize, which is a first step in understanding the proposed synchronization effect in a fully classical way.

Acknowledgements

As his support has been invaluable, I owe deep gratitude to Marios Kounalakis for his advice, comments, patience and stimulating me to become a critical independent researcher.
Many thanks to Gary Steele, for his useful physical insights, his advice on approaching difficult physical problems and of course for giving me the opportunity to work in his group.
During the project, I really enjoyed the coffee moments and lunches with my fellow master students and I want to thank them for their support, insights and sense of humor.
Grateful is the right word describing how I feel to my family and friends for always being a place where I feel at home.

Contents

Abstract **iii**

Acknowledgements **v**

1 Introduction **1**
1.1 Light-matter interaction . . . 1
1.2 Ultrastrong coupling in cQED . . . 1
1.3 Thesis outline . . . 2

2 Theory **5**
2.1 Transmission lines . . . 5
2.1.1 Telegrapher's equations . . . 5
2.1.2 Inductance and capacitance per length for a Coplanar Waveguide . . . 7
2.1.3 Lumped element equivalent . . . 8
2.1.4 Coupling to external circuit . . . 10
2.2 Josephson junctions . . . 11
2.3 Hamiltonian description of electromagnetic circuits . . . 13
2.4 Oscillators . . . 13
2.4.1 Harmonic oscillator . . . 13
2.4.2 Coupled harmonic oscillators . . . 14
2.4.3 Duffing oscillator . . . 16

3 Ground state quenching of a CPW **19**
3.1 Quench physics . . . 19
3.2 Intersection of CPW with tunable coupler . . . 20
3.3 Ground state quenching timescales . . . 22

4 Josephson Crystal: Design, fabrication and experimental setup **27**
4.1 Spectrum and off-resonant driving of the Josephson crystal . . . 27
4.2 Designing the Josephson crystal . . . 30
4.2.1 PCB . . . 31
4.2.2 Transmission lines . . . 31
4.2.3 Capacitively shunted junctions . . . 32
Capacitors . . . 32
Junctions . . . 33
4.2.4 Coupling capacitors . . . 34
4.2.5 Designing circuits in `Python` . . . 35
4.3 Fabrication . . . 38
4.4 Experimental setup . . . 39

5 Josephson crystal: Experimental results and analysis **41**
5.1 Experimental results . . . 41
5.1.1 Full spectra at low powers . . . 41
5.1.2 Bare resonator mode . . . 42
5.1.3 Broad peak . . . 46
5.2 Why do we see no tuning? . . . 48
5.2.1 Josephson sub-gap resistance . . . 48
5.2.2 Flux noise . . . 49
5.2.3 Non-linearity . . . 51

6 Mean field simulations of a Josephson crystal **59**
6.1 Mean field simulations . . . 59
6.2 Analytical expressions for flux fluctuations . . . 60

7 Classical model for the Josephson crystal: simulations of two degenerate Duffing oscillators with a purely nonlinear coupling **63**
7.1 Equations of motion . . . 63
7.2 Krylov-Bogoliubov method . . . 66
7.3 Results . . . 67

8 Conclusions and outlook **71**

A Three plus one junction device **73**

B `Python` code **75**
B.1 `stcad` additions . . . 75
B.1.1 CPW . . . 75
B.1.2 Interdigitated capacitor . . . 77
B.2 Chip design . . . 80

C Numerical instability **89**

D Peak in reflection parameters in classical non-linear model **91**

Bibliography **95**

Chapter 1

Introduction

1.1 Light-matter interaction

One of the most fundamental interactions in nature is the light-matter interaction. Reflection of light on a metallic surface, transmission of light through glass and scattering of light from this piece of paper are all manifestations of this same principle. Its most fundamental form is a single photon interacting with a single atom. Such a system has been extensively studied in the field of Cavity Quantum Electrodynamics (cavity QED) [1]. Here, a non-linearity like an atom is coupled to a single mode of the electromagnetic field in the cavity, which can be, for example, a pair of mirrors. As the spacing between different energy levels is different, such a system allows for stimulating transitions where exactly one photon is released or absorbed.

The rate at which the cavity and atom exchange photons, described by the coupling factor g, depends both on the dipole moment of the atom and the electric field strength in the cavity. Therefore, besides placing a strong dipole in the cavity, one can increase the coupling by making high quality factor cavities such that the released photon will bounce back and forward one million times before leaving the cavity [2]. The regime where the rate κ at which a photon leaves the cavity is much smaller than the coupling rate g, is called the strong coupling regime (SCR). This is illustrated in fig. 1.1. Besides being an elegant way of studying the quantum nature of light at the single photon level, strong coupling has applications in the realm of quantum computation too, as it allows for exchanging information between the atom and the photon many times before it is lost [3]. The strong coupling limit has been realized in many different setups, for example with alkali atoms in optical cavities [4] and Rydberg atoms in three-dimensional microwave cavities [5].

1.2 Ultrastrong coupling in cQED

Another field which explores the quantum mechanical nature of photons is Circuit Quantum Electrodynamics (cQED). Here photons are the quantized excitations of a superconducting

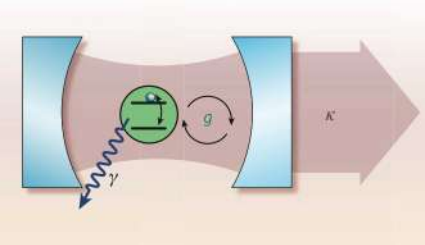

FIGURE 1.1: Two level system inside a cavity. On resonance, the cavity and two-level-system exchange photons at rate g. Photons are leaked to the environment by leaving the cavity at rate κ or by spontaneous decay to other modes at rate γ. Picture adapted from [3].

microwave resonator, like for example a transmission line or a LC circuit [6]. Non-linearity is introduced by the Josephson junction, which behaves as a non-linear inductor. By shunting such an inductor with a capacitor a non-linear spectrum can be made, as with an atom. Like this, setups analog to that of in cavity QED can be copied to cQED, with a number of differences. The photons propagating in a transmission line can only travel in one direction, such that they are well confined but still can travel from place to place [3]. Furthermore, the circuits are made with conventional lithography techniques, allowing for more freedom in engineering the system parameters [7]. The maximum coupling strength in cavity QED experiments is limited by the atoms dipole moments provided naturally, in cQED however the coupling strength can be engineered to be much higher, to the order of the resonator frequencies themselves. Finally, by shunting two Josephson junctions one can make a Superconducting Quantum Interference Device (SQUID) which behaves as a single inductor with its inductance dependent on the magnetic flux through it, allowing for changing the system parameters in situ [8].

In this thesis we will first study quenching the ground state of coplanar waveguide (CPW) with its central conductor interrupted a tunable coupling element consisting of a SQUID shunted with a capacitor. By means of a theoretical model we want to answer the question how fast we need to tune the flux to excite the ground state.

Second, we consider the case where the central conductor of a CPW is interrupted by equally spaced capacitively shunted SQUIDs. It has been theoretically shown that the strong coupling to the non-linearity causes the modes to switch synchronously as function of power when driven by a red-detuned drive [9]. In this thesis we investigate the feasibility of such an experiment by designing, fabricating and measuring a first generation of devices and by simulations. Furthermore, we make a first step in understanding the synchronization effect from a purely classical perspective, modelling a Josephson crystal with two junctions as two degenerate non-linearly coupled Duffing oscillators.

1.3 Thesis outline

This thesis is structured as follows. In chapter 2 we introduce the basic concepts of transmission lines and CPW microwave resonators. Next we introduce the Josephson junction as a non-linear inductor. Then we consider both harmonic and anharmonic oscillators (Duffing oscillator) from a classical perspective. Finally, we use second quantization to quantize the coupled oscillator and the Duffing oscillator.

In chapter 3 we consider a CPW intersected by capacitively shunted Josephson junction, whose frequency can be tuned by an external magnetic field. We quantize this system and simulate the dynamics of the ground-state after a fast change of the resonance frequency. Then, we consider the relevant timescale to excite the ground state to test the experimental feasibility of such an experiment.

In chapter 4, 5, 6 and 7 we consider a CPW intersected by equally spaced multiple capacitively shunted junctions, based on a proposal of Leib and Hartmann [9]. In chapter 4 we describe the design considerations, fabrication and experimental setup for a Josephson crystal consisting of five flux tunable junctions. Based on the same considerations, we fabricate a second device too, with two Josephson crystals consisting of three junctions and one junction respectively.

In chapter 5 we discuss and analyze the results obtained from a first round measurements where we cooled down the CPW intersected with one junction. To explain our data we make both a classical linear and non-linear model (Duffing oscillator) of our device.

In chapter 6 we use the mean-field code provided by Leib to solve the master-equation modelling the dissipative dynamics of the five junction crystal, tuned at the degeneracy point

and driven by a red-detuned drive. We explore the relevant parameters determining the occurrence of the synchronization effect.

To get a better understanding, in chapter 7 we make a first step in approaching the synchronization effect from a classical perspective. We expand our non-linear model from chapter 5 to two degenerate non-linearly coupled Duffing oscillators.

In chapter 8 we summarize our conclusions.

Chapter 2

Theory

2.1 Transmission lines

2.1.1 Telegrapher's equations

In the limit where the size of circuit elements are smaller than the spatial variation of voltage and current, any distributed circuit element can be viewed as a lumped element. The current and voltage can be considered constant across the wires and the system can be solved using conventional circuit analysis. However, when this it not the case, a more general approach is needed in the form of transmission line theory. In this section this is applied to Coplanar Waveguides (CPW) based on the work of Pozar [10].

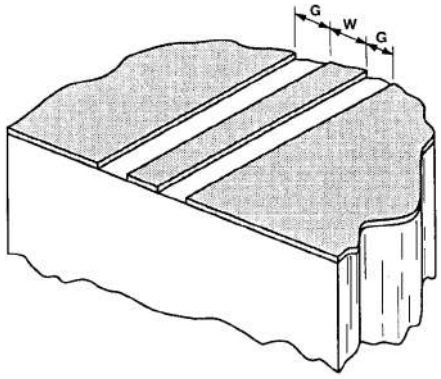

FIGURE 2.1: A CPW is a special case of a transmissionline. It consists of a conducting centrepin with width w seperated from the groundplane by a gap g. Picture adapted from [11].

A coplanar waveguide (CPW) is a special type of transmission line, consisting of a metal strip with width w separated on both sides from the ground by a gap of size g, shown in fig. 2.1.

We model this transmission line as an array of lumped element circuits, as shown in fig. 2.2. The internal loss is modelled as a series resistance per unit length r, the geometrical inductance as an inductance per length l, the capacitance per unit length between the centre pin and the ground as a capacitance per unit length c and the dielectric loss with a conductance per unit length g. By applying Kirchhoff's voltage and current laws and taking $\lim \Delta z \to \infty$ we find the so-called telegraphers equations:

$$\frac{\partial v(z,t)}{\partial z} = ri(z,t) - l\frac{\partial i(z,t)}{\partial t} \tag{2.1}$$

$$\frac{\partial i(z,t)}{\partial z} = -Gv(z,t) - c\frac{\partial v(z,t)}{\partial t} \tag{2.2}$$

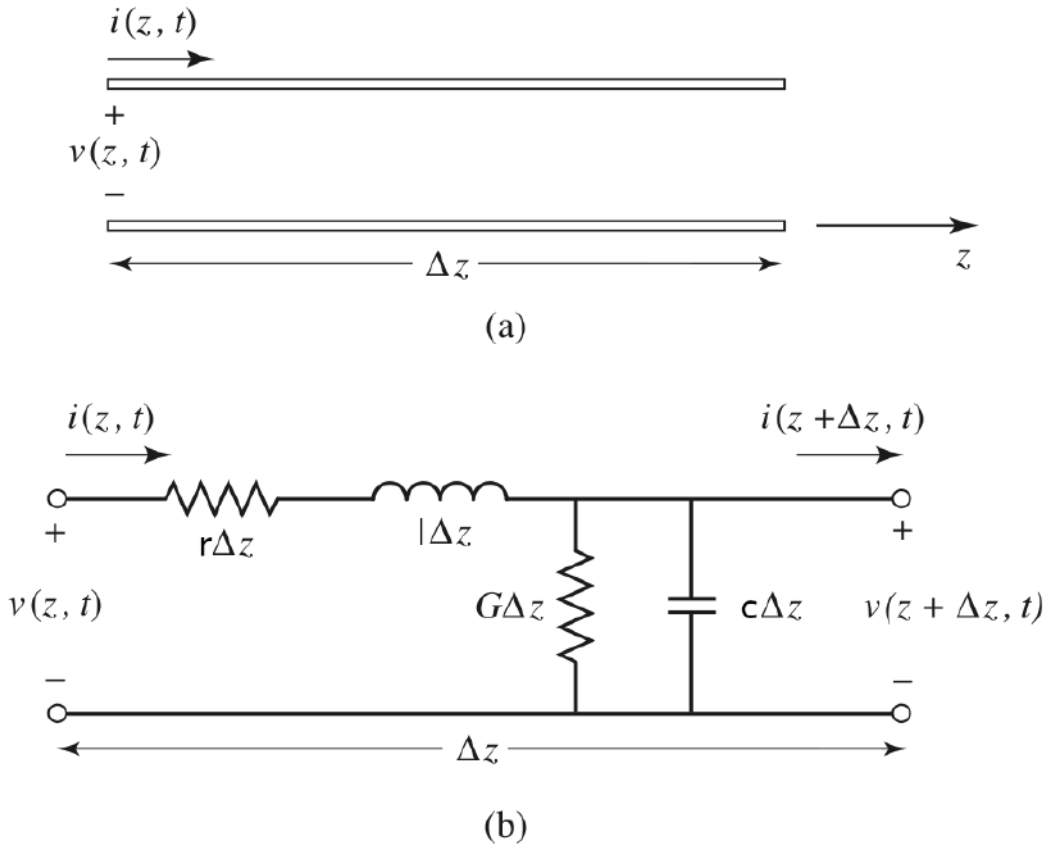

FIGURE 2.2: **a)** We represent a transmission line by two conducting strips with a voltage difference $v(t, z)$ supporting a current $i(t, z)$. **b)** To solve for the voltage $v(t, z)$ and $i(t, z)$ the transmission line is modeled as an infinite array of lumped elements taking into account the loss due to resistance, the geometrical inductance, capacitance to ground and leakage current. Picture adapted from [10].

Plugging in the phasors $v(z,t) = Ve^{i\omega t}$ and $i(z,t) = Ie^{i\omega t}$ we find wave equations for V and I with general solutions:

$$V(z) = V_0^+ e^{-\gamma z} + V_0^- e^{\gamma z} \tag{2.3}$$

$$I(z) = \frac{I_0^+}{Z_0} e^{-\gamma z} - \frac{I_0^-}{Z_0} e^{\gamma z} \tag{2.4}$$

With $Z_0 = \frac{V_0^+}{I_+^0} = -\frac{V_0^-}{I_-^0} = \sqrt{\frac{r+j\omega l}{G+j\omega c}}$ and $\gamma = \sqrt{(r + j\omega l)(G + j\omega c)} = \alpha + j\beta$. Here the real part α is called the attenuation constant as it represents the decay of the fields due to losses. In the special case when there is no loss, i.e. $r = G = 0$ the attenuation constant α is zero and $\beta = \omega\sqrt{lc}$.

We will briefly look at the reflection coefficient for the case a transmission line with impedance Z_0 is ended with an impedance Z_L, shown in fig. 2.3. At the load the we have:

$$Z_L = \frac{V(0)}{I(0)} = \frac{V_0^+ + V_0^-}{V_0^+ - V_0^-} Z_0 \tag{2.5}$$

If we define the reflection coefficient Γ as the ratio of the outgoing amplitude and the ingoing amplitude, we get the following expression:

$$\Gamma = \frac{V_0^-}{V_0^+} = \frac{Z_L - Z_0}{Z_L + Z_0} \tag{2.6}$$

In case $Z_L = 0$ we get a reflection of $\Gamma = -1$. So the signal is completely reflected and undergoes a π phase shift. In case of an infinite impedance we get $\Gamma = 1$. Finally, when the load is matched we have $\Gamma = 0$ and the signal is completely transmitted. This is called impedance matching.

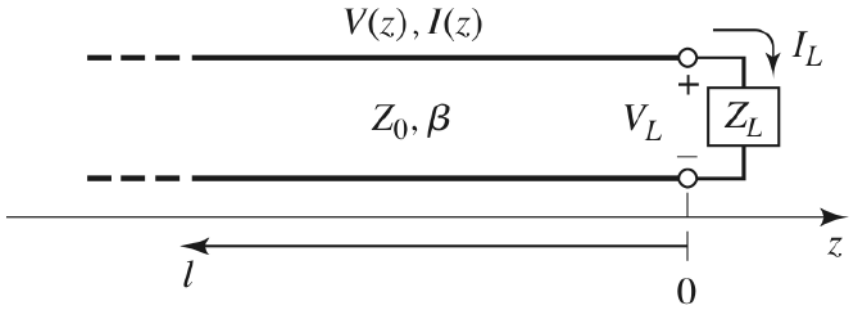

FIGURE 2.3: Transmission line with impedance Z_0 ended with an impedance Z_L. Picture adapted from [10]

2.1.2 Inductance and capacitance per length for a Coplanar Waveguide

For a CPW an analytical expression for the capacitance per unitl length c is given by [12]:

$$c = 4\epsilon_0\epsilon_{\text{eff}}\frac{K(k)}{K(k')} \tag{2.7}$$

Here $\epsilon_{\text{eff}} \approx \frac{1+\epsilon_{\text{substr}}}{2}$ [13], K is the elliptic integral of the first kind, $k = \frac{W}{W+2G}$ and $k^2 + k^{'2} = 1$. The inductance per unit length is the sum of the geometrical inductance and kinetic inductance $l = l_{\text{g}} + l_{\text{k}}$. The geometrical inductance is given by [12]:

$$l_{\text{g}} = \frac{\mu_0}{4}\frac{K(k)}{K(k')} \tag{2.8}$$

The kinetic inductance per unit length depends both on the surface impedance of the substrate l_s and the geometry $l_{\text{k}} = g(d, W, G)l_{\text{s}}$. Here $g(d, W, G)$ is geometrical factor with contributions both from the central conductor and the groundplane [14]:

$$g = g_{\text{ctr}} + g_{\text{gnd}} \tag{2.9}$$

$$g_{\text{ctr}} = \frac{1}{4W(1-k^2)K(k)^2}\left[\pi + \ln\left(\frac{4\pi W}{d}\right) - k\ln\left(\frac{1+k}{1-k}\right)\right] \tag{2.10}$$

$$g_{\text{gnd}} = \frac{1}{4W(1-k^2)K(k)^2}\left[\pi + \ln\left(\frac{4\pi(W+2G)}{d}\right) - \frac{1}{k}\ln\left(\frac{1+k}{1-k}\right)\right] \tag{2.11}$$

With d the thickness of the substrate. This is accurate within 10% for $d < 0.05W$ and $k < 0.8$ [13]. The substrate we use has $k = 0.6$ and $\frac{d}{W} \approx 0.02$.

2.1.3 Lumped element equivalent

Now we look more carefully to an open-ended transmission line. From eq. (2.4) and using that $V_0^- = V_0^+$ ($\Gamma = 1$ because of the open ends) we get for the current and voltage :

$$V(z) = V_0^+ e^{-\gamma z} + V_0^+ e^{\gamma z} = 2V_0^+ \cosh \gamma z \tag{2.12}$$

$$I(z) = \frac{1}{Z_0}\left(V_0^+ e^{-\gamma z} - V_0^+ e^{\gamma z}\right) = -\frac{2V_0^+}{Z_0}\sin(\gamma z) \tag{2.13}$$

For a lossless line we set $\alpha = 0$. We see that the equation above reduces to:

$$V(z) = 2V_0^+ \cos \beta z \tag{2.14}$$

$$I(z) = -\frac{2jV_0^+}{Z_0}\sin(\beta z) \tag{2.15}$$

From this we can define a wavelength and derive a dispersion relation $\lambda \equiv \frac{2\pi}{\beta} = 2\pi\frac{v}{\omega}$. We see that at the end $I = 0$ as expected for an open circuit. Now if we require $I = 0$ at the beginning too we see that this resonator can host waves with:

$$\lambda = \frac{2\ell}{n+1} \tag{2.16}$$

with $n \in \mathbb{N}$. This is called a $\frac{\lambda}{2}$ resonator. Around a resonance this can be modelled as a parallel RLC circuit. Here we will follow the analysis of Pozar and extend it to any mode n. The impedance is given by:

$$Z = \frac{V(z)}{I(z)} = -Z_0 \coth(\alpha + j\beta)\ell = -\frac{\tan\beta\ell \tanh\alpha\ell}{\tanh\alpha\ell + j\tan\beta\ell} \tag{2.17}$$

Now for a general mode n, we expand β around ω_n.

$$\beta \approx \frac{\omega_n}{v} + \frac{\Delta\omega}{v} = \frac{2\pi}{\lambda_n} + \frac{2\pi\Delta\omega}{\lambda_n\omega_n}$$

Using that $\frac{1}{v} = \frac{2\pi}{\lambda_n\omega_n}$. Now assumig a $\frac{\lambda}{2}$ resonator, $\omega_n = (n+1)\omega_0$ and $\lambda_n = \frac{2\ell}{n+1}$. Then:

$$\beta \approx \frac{(n+1)\pi}{\ell} + \frac{\pi\Delta\omega}{\omega_0\ell}$$

Now $\tan\beta\ell \approx \frac{\pi\Delta\omega}{\omega_0}$ and assuming a low loss, $\tanh\alpha\ell \approx \alpha\ell$ we get:

$$Z \approx Z_0 \frac{\frac{1}{\alpha\ell}}{1 + j\frac{\pi\Delta\omega}{\omega_0\alpha\ell}} \tag{2.18}$$

We compare these results with parallel RLC circuit, shown in fig. 2.4a. This circuit has an impedance:

$$Z = \left(\frac{1}{R} + \frac{1}{j\omega L} + j\omega C\right)^{-1} = \left(\frac{1}{R} - \frac{1 + j\omega C}{\omega^2 LC}\right)^{-1} \tag{2.19}$$

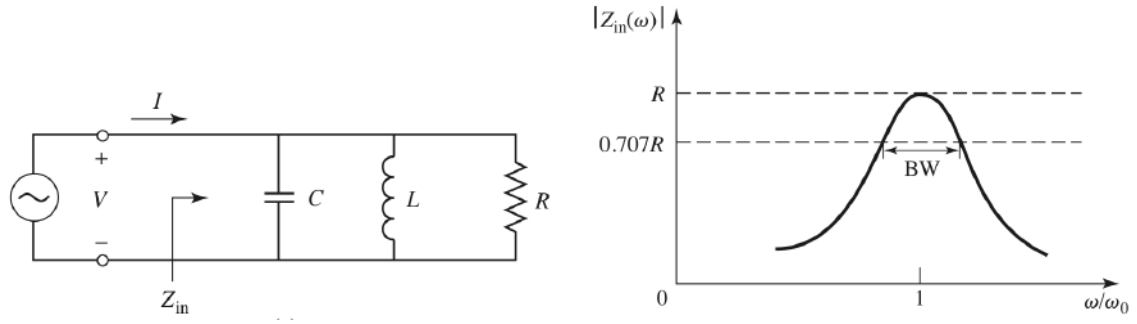

(A) (B)

FIGURE 2.4: (A) A parallel RLC resonator. (B) Resonance of a parallel RLC resonator. Picture adapted from [10]

We see that this has a resonance at $\omega_0 = \frac{1}{\sqrt{LC}}$, shown in fig. 2.4b. Expanding around this resonance we get, using a geometric series:

$$Z \approx \frac{R}{1 + 2j\Delta\omega RC} \tag{2.20}$$

Note that in case $R \to \infty$ we would have had $Z = \frac{1}{2jC(\omega-\omega_0)}$. So we also could have calculated the lossless case first and then substituted $\omega_0 \to \omega_0 + \frac{j}{2RC}$.

The bandwidth BW is defined such that $\text{BW} = \frac{\omega_{l,1/2} - \omega_{r,1/2}}{\omega_0}$ with $\omega_{l,1/2}$ and $\omega_{r,1/2}$ the frequencies where $|Z|^2 = \frac{R^2}{2}$, meaning that the power delivered to circuit is half that of the power at resonance. We see that this yields:

$$\text{BW} = \frac{1}{\omega_0 RC} \tag{2.21}$$

Now we define the quality factor as the ratio between the average energy stored and dissipated:

$$Q = \omega_0 \frac{W_m + W_e}{P_{\text{loss}}} = \omega_0 \frac{2\frac{1}{4}|V|^2 C}{\frac{1}{2R}|V|^2} = \omega_0 RC \tag{2.22}$$

Were we used that on resonance the energy stored in the inductor and capacitor is the same. If we define κ as the absolute bandwidth, i.e. $\kappa = \omega_0 \text{BW}$ we see that this is related to the quality factor as follows:

$$\kappa = \frac{\omega_0}{Q} \tag{2.23}$$

If we compare the results of the open-ended $\frac{\lambda}{2}$ resonator and the parallel RLC circuit, we get the following relations:

$$R = \frac{Z_0}{\alpha\ell} \tag{2.24}$$

$$C = \frac{\pi}{2\omega_0 Z_0} \tag{2.25}$$

$$L = \frac{1}{(n+1)^2 \omega_0^2 C} \tag{2.26}$$

$$Q_n = \omega_n RC = (n+1)\frac{\pi}{2\alpha\ell} \tag{2.27}$$

2.1.4 Coupling to external circuit

Now we look at the effect of coupling a $\frac{\lambda}{2}$ resonator to the outside world with two coupling capacitors. We model our circuit as a parallel RLC circuit, coupled to the outside world (in most cases another transmission line) with impedance Z_0 and with a coupling capacitance C_c. This is shown in fig. 2.5. For its external impedance seen from the resonator we can write:

$$\frac{1}{Z_\mathrm{e}} = \frac{2}{Z_0 + \frac{1}{j\omega C_c}} = 2\left(\frac{\omega^2 C_c^2 Z_0}{1+\omega^2 C_c^2 Z_0^2} + \frac{j\omega C_c}{1+\omega^2 C_c^2 Z_0^2}\right) \tag{2.28}$$

We transform this circuit in another one, shown at the right in fig. 2.5. This circuit has external impedance:

$$\frac{1}{Z_\mathrm{e}} = 2\left(\frac{1}{R^*} + j\omega C^*\right) \tag{2.29}$$

So we can view the coupling to the environment as shunting our circuit twice with a resistance R^* and a capacitance C^* with:

$$R^* = \frac{1+\omega^2 C_c^2 Z_0^2}{\omega^2 C_c^2 Z_0} \approx \frac{1}{\omega^2 C_c^2 Z_0^2} \qquad C^* = \frac{C_c}{1+\omega^2 C_c^2 Z_0^2} \approx C_c \tag{2.30}$$

Where for the approximations we assume small coupling capacitances such that $\omega^2 C_c^2 Z_0^2 \ll 1$.

We can use exact the same equations as in our previous section, but now with an effective capacitance $\tilde{C} = C + 2C_c$ and an effective resistance $\tilde{R} = \frac{RR^*}{2R+R^*}$. From this we already see that our resonance becomes a lower (as expected, because the capacitors increase the electrical length), according to $\omega_0 = \frac{1}{L(C+2C_c)}$. Now for the line width we find:

$$\kappa_\mathrm{tot} = \frac{1}{R^* C^*} \approx \frac{1}{R(C+2C_c)} + \frac{2}{R^*(C+2C_c)} = \kappa_\mathrm{int} + \kappa_\mathrm{ext} \tag{2.31}$$

Here the first term only involves the internal resistance R while the other term only involves the external resistance R^*. So we can interpret these terms as the energy internal dissipated and the energy delivered to the outside world. From this we can define a coupling

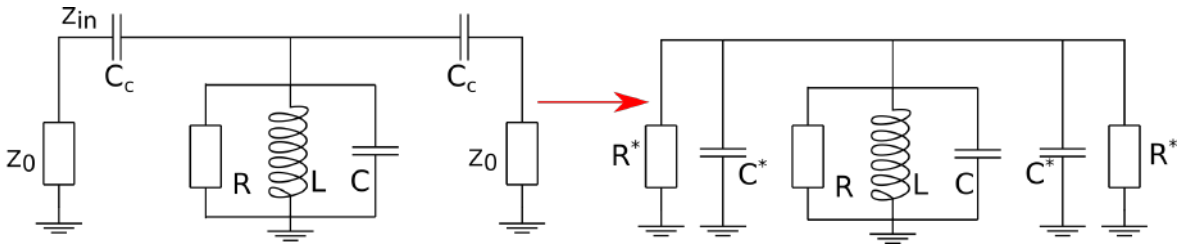

FIGURE 2.5: We couple a $\frac{\lambda}{2}$ transmission line to another impedance Z_0 with coupling capacitance C_c. This is modelled as a parallel RLC circuit coupled to a capacitance C_c and impedance Z_0 in series. To make our calculations easier, we place the impedance Z_0 and coupling capacitance C_c in parallel and introduce an new resistance R^* and capacitance C^*.

factor $g = \frac{\kappa_{\text{ext}}}{\kappa_{\text{int}}} = \frac{Q_{\text{int}}}{Q_{\text{ext}}}$. Expressed as a quality factor:

$$Q_{\text{int}} = \omega_0 R(C + 2C_c) \tag{2.32}$$

$$Q_{\text{ext}} = \frac{C + 2C_c}{2\omega_0 C_c^2 Z_0} \tag{2.33}$$

When we drive the system with $g < 1$ more energy is dissipated internally than is returned to the drive. In this case the drive hardly distorts the system, but we have low signal, which is called undercoupling. In the opposite case, more energy is returned to the drive than is dissipated internally. In this case, called overcoupling, the drive significantly decreases the quality factor the system, but at the same time gets a high signal. When $g = 1$ we are critically coupled.

We calculate the input impedance by viewing the second port as part of the resonator and consider the case $\frac{RR^*}{R+R^*} \to \infty$:

$$Z_{\text{in}} = \left(\frac{1}{j\omega L} + j\omega(C + C_c)\right)^{-1} \tag{2.34}$$

$$= i\frac{\frac{\omega^2}{\omega_0^2} - 1}{\omega C_c\left(1 - \omega^2 L(C + C_c)\right)} \tag{2.35}$$

Next we Taylor expand and introduce loss by replacing $\omega_0 \to \omega_0 + \frac{j(R+R^*)}{C+2C_C}$:

$$Z_{\text{in}} = 2jL\frac{(C + C_c)^2}{C_c^2}\Delta\omega = jL\frac{(C + C_c)^2}{C_c^2}\left(\kappa_{\text{int}} + \frac{\kappa_{\text{ext}}}{2} + 2j\Delta\Omega\right) \tag{2.36}$$

Now we can calculate the reflection parameter, which can be expressed in terms of κ_{int} and κ_{ext}:

$$\Gamma = \frac{Z_{\text{in}} - Z_0}{Z_{\text{in}} + Z_0} \tag{2.37}$$

$$= \frac{\kappa_{\text{int}} + \frac{\kappa_{\text{ext}}}{2} + 2j\Delta\omega - jL\frac{(C+C_c)^2}{C_c^2}}{\kappa_{\text{int}} + \frac{\kappa_{\text{ext}}}{2} + 2j\Delta\omega + jL\frac{(C+C_c)^2}{C_c^2}} \tag{2.38}$$

$$= \frac{\kappa_{\text{int}} + 2i\Delta\omega}{\kappa_{\text{int}} + \kappa_{\text{ext}} + 2i\Delta\omega} \tag{2.39}$$

2.2 Josephson junctions

In section 2.2 a superconductor is shown, interrupted by a barrier, for example an insulator (S-I-S), a normal conductor (S-N-S) or a geometrical constriction (S-s-S). When there is a finite phase difference between the two wave functions, some cooper pairs will tunnel through the barrier giving rise to a current depending on the phase difference $\delta = \phi_l - \phi_r$ [15]:

$$I = I_c \sin(\delta) \tag{2.40}$$

Here I_c is the maximum current that will flow, which depends on the type of barrier, the cross-sectional area and the width of the barrier.

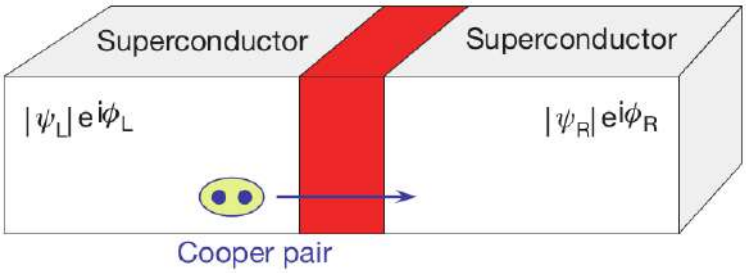

FIGURE 2.6: A Josephson junction consists of a superconductor interrupted by some barrier (red). When there is a finite phase difference between both superconductors, cooper pairs will tunnel through the barrier. Picture adapted from [7]

When the phase difference δ depends on time, there will also be a voltage across the junction:

$$V = \frac{\hbar}{2e}\frac{\partial \delta}{\partial t} \tag{2.41}$$

These equations are known as the Jospehson equations, named after Brian Josephson who discovered them in 1962. If we combine these two equations, we find the following voltage-current relation:

$$V = \frac{\hbar}{2eI_c \cos(\delta)}\frac{\partial I}{\partial t} \tag{2.42}$$

Which has the same form as the voltage-current relation of an inductor $V = L\frac{\partial I}{\partial t}$ with inductance:

$$L = \frac{\hbar}{2eI_c \cos(\delta)} \tag{2.43}$$

Therefore, as the inductance of the Josephson junction depends on the phase difference across it, it can be viewed as a non-linear inductor.

The energy stored in a junction is given by the work needed to bring the phase from 0 to δ:

$$U = \int_0^\delta IV dt = \frac{\hbar}{2e} I_c \int_0^\delta \sin\left(\tilde{\delta}\right) d\tilde{\delta} = \phi_0 I_c \left(1 - \cos(\delta)\right) \tag{2.44}$$

So the typical energy scale for Josephson junctions is given by:

$$E_J = \phi_0 I_c \tag{2.45}$$

With ϕ_0 the reduced flux quantum $\frac{\hbar}{2e}$. By shunting two junctions we create a so-called SQUID (Super Conducting QUantum Interference Device) which behaves as a single junction but with its inductance dependent on the magnetic flux through the loop [16]. When the Josephson energies of the single junctions are different, the Josephson energy of the SQUID becomes [17]:

$$E_j(\phi) = E_{j,0}\sqrt{\alpha^2 + (1-\alpha^2)\cos^2\left(\pi\frac{\phi}{\phi_0}\right)} \tag{2.46}$$

Here, $E_{j,0}$ is the sum of the Josephson energies of the individual junctions $E_{j,1}$ and $E_{j,2}$, and α describes the asymmetry between the junctions:

$$\alpha = \left| \frac{E_{j,1} - E_{j,2}}{E_{j,1} + E_{j2}} \right| \tag{2.47}$$

2.3 Hamiltonian description of electromagnetic circuits

In order to quantize our circuits, we need to find the Hamiltonian of the circuit. For this we will follow the procedure as described by Vool and Devoret [18]. For each node of the circuit a generalized flux is defined according to $\phi(t) = \int_{-\infty}^{t} V(t')dt'$. Like this we can treat the phase difference across a junction and magnetic flux in the same way, since $\delta = \frac{\phi_{j+1} - \phi_j}{\phi_0}$ [18]. Then by Kirchoff's laws, the number of coordinates can be reduced and the degrees of freedom are found. We can find the Lagrangian by defining the kinetic energy as the energy stored in the capacitances and the potential energy as the energy stored in the inductors.

$$E_{\text{kin}} = \frac{C}{2}\left(\dot{\phi}_{j+1} - \dot{\phi}_j\right)^2 \quad E_{\text{pot, lin}} = \frac{1}{2L}\left(\phi_{j+1} - \phi_j\right)^2 \quad E_{\text{pot, jos}} = \frac{\phi_0^2}{L_j}\left(1 - \cos\left(\frac{\phi}{\phi_0}\right)\right) \tag{2.48}$$

Then we write down the Lagrangian $\mathcal{L} = T - V$ and introduce the canonical momenta $\pi_j = \frac{\partial \mathcal{L}}{\partial \dot{\phi}_j}$. Next we apply a Legendre transform to find the Hamiltonian:

$$H = \left(\sum_j \pi_j \dot{\phi}_j\right) - \mathcal{L} \tag{2.49}$$

From this we can postulate commutator relations between π and ϕ, promote them to operators and follow the standard procedure for quantization.

2.4 Oscillators

2.4.1 Harmonic oscillator

A harmonically driven harmonic oscillator has the following equation of motion:

$$m\ddot{x} + c\dot{x} + kx = F_0 \cos(\omega_d t) \tag{2.50}$$

And potential:

$$V = \frac{1}{2} m\omega_0^2 x^2 \tag{2.51}$$

With $\omega_0 = \sqrt{\frac{k}{m}}$. Then, by trying $x = \rho e^{-j\omega t + j\theta}$ we get the following solutions [19]:

$$\rho = F_0 \sqrt{\frac{1}{m^2\left(\omega_d^2 - \omega_0^2\right)^2 + c^2\omega_d^2}} \qquad \tan(\theta) = -\frac{c\omega}{m\left(\omega_0^2 - \omega_d^2\right)} \tag{2.52}$$

This is shown in fig. 2.7.

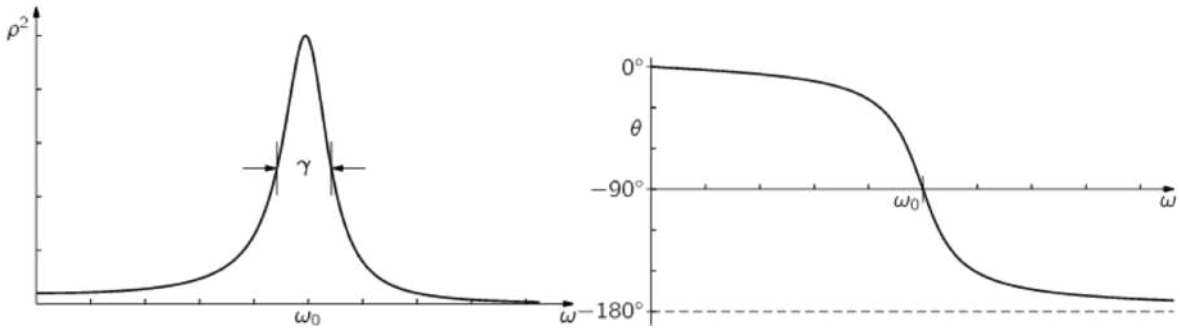

FIGURE 2.7: Response of a harmonically driven harmonic oscillator. The width of the resonance is determined by the damping, here denoted by $\gamma = \frac{c}{m}$. Picture adapted from [19].

2.4.2 Coupled harmonic oscillators

Now consider the linear coupling of two harmonic oscillators. As an example we look at two springs, with spring constant k_A and k_B, coupled by another spring with spring constant κ. This is shown in fig. 2.8

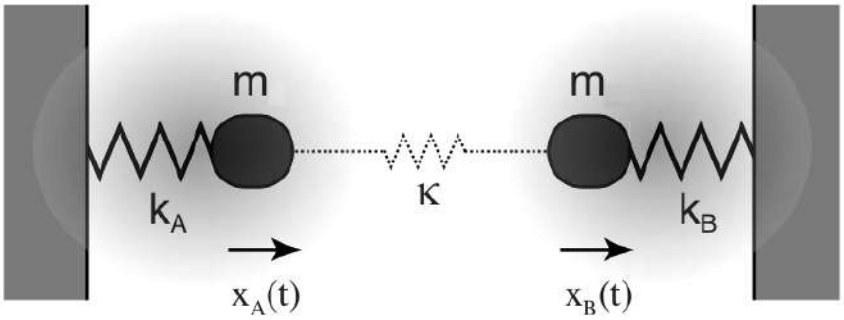

FIGURE 2.8: Two springs coupled by a second spring. This spring leads to frequency splitting. Picture adapted from [20].

This system is described by the following two equations:

$$m\ddot{x}_A + k_A x_A + \kappa\left(x_A - x_B\right) = 0 \tag{2.53}$$
$$m\ddot{x}_B + k_B x_B - \kappa\left(x_A - x_B\right) = 0 \tag{2.54}$$

Again, we substitute $e^{-j\omega t}$ as trial solution, and we get the following eigenfrequencies:

$$\omega_\pm = \frac{1}{2}\left(\omega_A^2 + \omega_B^2 \pm \sqrt{\left(\omega_A^2 - \omega_B^2\right)^2 + 16 g \omega_A \omega_B}\right) \tag{2.55}$$

With $g = \frac{\kappa}{2m\sqrt{\omega_A \omega_B}}$ and $\omega_A = \sqrt{\frac{k_A+\kappa}{m}}$ and $\omega_B = \sqrt{\frac{k_B+\kappa}{m}}$. No we look what happens when we sweep k_A and keep k_B constant. When there is no coupling eq. (2.55) reduces to ω_A and ω_B and we get two straight lines, this is shown in fig. 2.9 to the left.

When we turn on the coupling we see that when the modes are far detuned $(\omega_A^2 - \omega_B^2) \gg \frac{\kappa}{m}$ we have the same as in the uncoupled case. However, in the opposite case, we get a mode with a lower frequency and a mode with higher frequency. The first does not involve the coupling spring and belongs to the symmetric mode, where both masses move in phase. The

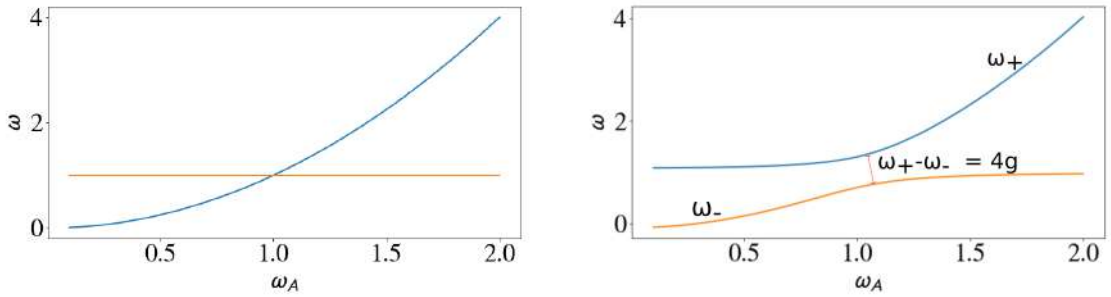

FIGURE 2.9: Spectrum of coupled and uncoupled oscillators. The left picture shows the eigenfrequencies when there is no coupling and the frequencies are brought to resonance by changing ω_A and keeping ω_B constant. When they get close, the frequencies split and a lower and higher mode emerge.

higher mode belongs to the antisymmetric mode where the masses move in anti-phase and does involve the coupling spring. When $\omega_A = \omega_B$ we get:

$$\omega_{\pm}^2 = \omega^2 \left(1 \pm 4g\omega\right) \tag{2.56}$$

And we see that $8g\omega = \omega_+^2 - \omega_-^2$. So the width of the split is given by $\omega_+ - \omega_- \approx 4g$.

Now, we briefly look at a quantum description of the two linear coupled oscillators. We write for the Lagrangian:

$$\begin{aligned}\mathcal{L} = T - V =& \frac{1}{2}m\dot{x}_A^2 + \frac{1}{2}m\dot{x}_B^2 - \frac{1}{2}k_A x_A^2 - \frac{1}{2}k_B x_B^2 - \frac{1}{2}\kappa\left(x_A - x_B\right)^2 && (2.57)\\ =& \frac{1}{2}m\dot{x}_A^2 + \frac{1}{2}m\dot{x}B^2 - \frac{1}{2}(k_A + \kappa)x_A^2 - \frac{1}{2}(k_B + \kappa)x_B^2 - \kappa x_A x_B && (2.58)\end{aligned}$$

Now $p_A = \frac{\partial \mathcal{L}}{\partial \dot{x}_A}$ and $p_B = \frac{\partial \mathcal{L}}{\partial \dot{x}_B}$. Then,

$$\begin{aligned}H =& \left(\sum_{A,B} \dot{x}_i p_i\right) - \mathcal{L} && (2.59)\\ =& \frac{p_A^2}{2m} + \frac{p_B^2}{2m} + \frac{1}{2}\left(k + \kappa\right)x_A^2 + \left(k + \kappa\right)x_B^2 + \kappa x_A x_B && (2.60)\end{aligned}$$

Now we quantize according to $\hat{x}_A = \sqrt{\frac{\hbar}{2m\omega_A}}\left(\hat{a}^+ + \hat{a}\right)$ and $\hat{p}_A = j\sqrt{\frac{\hbar m\omega_A}{2}}\left(\hat{a}^+ - \hat{a}\right)$ and similar for B, with $[\hat{a}, \hat{a}^+] = [\hat{b}, \hat{b}^+] = 1$. We get:

$$\begin{aligned}\hat{H} =& \hbar\omega_A\left(\hat{a}^+\hat{a} + \frac{1}{2}\right) + \hbar\omega_B\left(\hat{b}^+\hat{b} + \frac{1}{2}\right) + \frac{\hbar\kappa}{2m\sqrt{\omega_A\omega_B}}\left(\hat{a}^+ + \hat{a}\right)\left(\hat{b}^+ + \hat{b}\right) && (2.61)\\ =& \hbar\omega_A\left(\hat{a}^+\hat{a} + \frac{1}{2}\right) + \hbar\omega_B\left(\hat{b}^+\hat{b} + \frac{1}{2}\right) + \hbar g\left(\hat{a}^+ + \hat{a}\right)\left(\hat{b}^+ + \hat{b}\right) && (2.62)\end{aligned}$$

And we see that the frequency splitting now appears as four times the rate at which photons are exchanged between the oscillators.

2.4.3 Duffing oscillator

We consider a mass spring system with a linear restoring force $F = kx$ and no dissipation. This system has the well-known equation of motion:

$$m\frac{d^2x}{dt^2} + kx = 0 \tag{2.63}$$

And potential energy:

$$V = m\frac{\omega_0^2}{2}x^2 \tag{2.64}$$

We know that this system has a harmonic solution with $\omega_0 = \sqrt{\frac{k}{m}}$. Now, we make the spring non-linear by adding:

$$F = kx + \beta m x^3 \tag{2.65}$$

We can distinct two cases: $\beta > 0$ and $\beta < 0$. The first is generally called 'spring-hardening' and the second 'spring-softening'. This can be understood by writing:

$$F = kx + m\beta x^3 = (k + m\beta x^2)x \tag{2.66}$$

So the non-linearity can be interpreted as an amplitude dependent spring constant, such that the spring becomes stiffer when $\beta > 0$ and softer when $\beta < 0$. The equation of motion becomes:

$$m\frac{d^2x}{dt^2} + kx + m\beta x^3 = 0 \tag{2.67}$$

And the potential energy:

$$V = m\frac{\omega_0^2}{2}x^2 + m\frac{\beta}{4}x^4 \tag{2.68}$$

When we normalize eq. (2.67) and add a dissipative term $mr\frac{dx}{dt}$ we get the Duffing equation:

$$\frac{d^2x}{dt^2} + r\frac{dx}{dt} + \omega_0^2 x + \beta x^3 = 0 \tag{2.69}$$

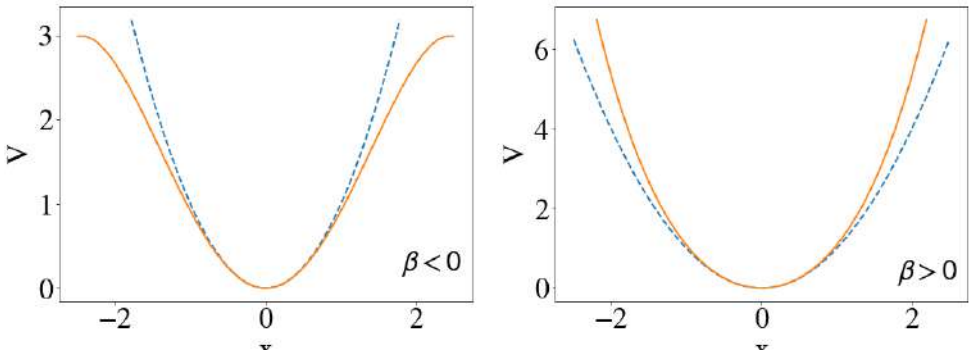

FIGURE 2.10: Anharmonic potentials of mass-spring system with spring-softening non-linearity ($\beta < 0$) and spring-hardening ($\beta > 0$) non-linearity. The blue line shows the unperturbed harmonic potential.

This type of equation differs from the harmonic oscillator in a number of ways: it has no analytic solution anymore, the superposition principle is not valid anymore and new phenomena emerge like the appearance of strange attractors, subharmonics and bifurcation [21][22].

The bifurcation phenomenon will be important later on in this thesis. Here we will focus on a qualitative understanding, in section 5.2.3 we will numerically solve the equation. An example of bifurcation is shown in fig. 2.11. To understand this, we rewrite the potential:

$$V = m(\frac{\omega_0^2}{2} + \frac{\beta}{4}x^2)x^2 \tag{2.70}$$

We see that the non-linearity now appears as an amplitude dependent frequency shift. The potentials for spring-hardening and spring-softening case are plotted in fig. 2.10. When we drive a spring-hardening system above its resonance frequency two states are possible: either the particle takes a low amplitude and behaves the same as a harmonic oscillator driven above its eigenfrequency, or it takes a high amplitude such taht the 'effective' eigenfrequency is shifted up bringing it on resonance with the drive. Increasing the drive frequency, the particle will stay on resonance by increasing its amplitude up to some point where it jumps down to the lower mode. This 'jump-down' frequency depends on the dissipation r, the spring constant k, β and the driving strength F [23]:

$$\omega_+ = \sqrt{\frac{1}{2} + \frac{1}{2}\sqrt{1 + \frac{3\beta F^2}{k^2 r^2}}} \tag{2.71}$$

A important example of a Duffing oscillator in cQED is the transmon qubit, which is basically a Josephson junction shunted with a big capacitor. In the weakly anharmonic limit and with now offset charge, its Hamiltonian reads [24][25]:

$$\hat{H} = 4E_c\hat{n}^2 + E_j\frac{\hat{\delta}^2}{2} - E_j\frac{\hat{\delta}^4}{24} \tag{2.72}$$

Here $\hat{n} = -i\frac{d}{d\delta}$ is the number of electrons passed through the junctions and $\hat{\delta} = \delta$ the phase across the junction. When we compare this with our Duffing Hamiltonian, where we have the operators $\hat{p} = -i\hbar\frac{d}{dx}$ and $\hat{x} = x$:

$$\hat{H} = \frac{\hat{p}^2}{2m} + m\frac{\omega_0^2\hat{x}^2}{2} + m\frac{\beta\hat{x}^4}{4} \tag{2.73}$$

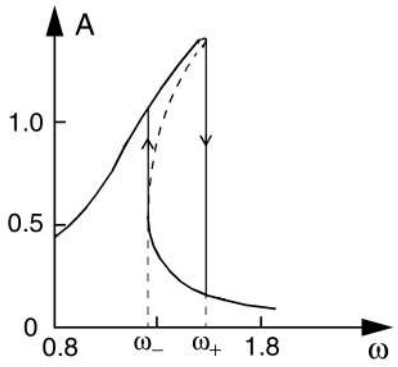

FIGURE 2.11: Bifurcation in a Duffing oscillator with $\beta > 0$. The system has two stable branches for $\omega > \omega_0$. Picture adapted from [21].

We see that $\frac{\hbar^2}{2m} \to 4E_c$ and $m\omega_0^2 \to E_J$. Now, when we quantize this, using the same definitions as with the coupled oscillators $\hat{x} = \sqrt{\frac{\hbar}{2m\omega}}\left(\hat{a}^+ + \hat{a}\right)$ and $\hat{p} = j\sqrt{\frac{\hbar m\omega}{2}}\left(\hat{a}^+ - \hat{a}\right)$, keeping only the lowest order terms, we find:

$$\hat{H} = \hbar\omega\left(\hat{a}^+\hat{a} + \frac{1}{2}\right) + \frac{3m\beta\hbar^2}{8}\left(\hat{a}^+\hat{a}^+\hat{a}\hat{a}\right) \tag{2.74}$$

Chapter 3

Ground state quenching of a CPW

3.1 Quench physics

The adiabatic theorem gives a qualitative prediction of the dynamics of a quantum system prepared in an eigenstate undergoing a transition in its potential landscape over time [26]. According to the theorem we can identify two cases here: adiabatic and diabatic. In the first case, we change the Hamiltonian from H_{initial} to H_{final} slowly compared to some timescale τ. The adiabatic theorem tells us that, when the system was in the n^{th} eigenstate of H_{initial}, it will end up in the n^{th} eigenstate of H_{final}. In the latter case, we change the Hamiltonian faster than τ such that the system is still in the eigenstate of H_{initial}. However, the eigenstates of the system are now those of H_{final} , so the system is now in a superposition. This is schematically illustrated for the case of a particle in a box in fig. 3.1.

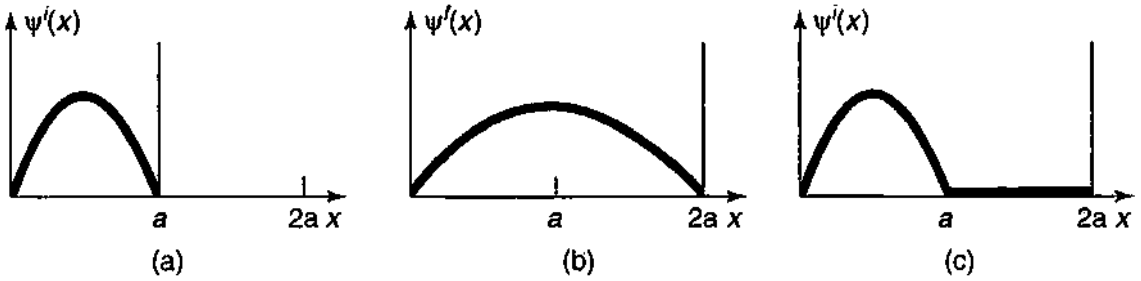

FIGURE 3.1: In (a) the particle is in its ground state. When the potential is slowly varied, the particle ends up in the ground state of the new system, shown in (b). If the potential is changed very fast, the particle still is in the eigenstate of the initial potential and in a superposition of eigenstates of the new potential, shown in (c) [27].

In the diabatic case, it is not evident how the system will evolve and will typically depend on the system in consideration [28]. A number of theoretical studies on cases in the realm of solid state physics has been conducted on for example the XY model [29] and the Ising model [30]. Typical questions concern the mechanisms involved, typical timescales, what happens close to critical points and the kind of correlations expected [31]. Experimental realization with ultracold atoms of the transition from superfluid to a Mott insulating state [32] renewed interest in the topic, as now some questions possibly could be answered experimentally [33] [34]. From then, numerous experiments have been performed involving ultracold atom gasses [35] [14] [36] .

Circuit Quantum Electrodynamics (cQED) has been shown to provide a useful platform for simulating many-body physics [37]. As explainend in section 1.2, quantum circuits are flexible in their design and fabrication of the system parameters, offering the possibility for exploring strong and ultrastrong coupled regimes [38] . By considering the interruption of

the central conductor of a CPW with a tunable coupler we will explore in this chapter a possibility of applying the cQED toolbox to quenching problems. In such an experiment we would have a very simple system. Moreover, in contrast to ultracold atoms, this is an open system which allows for exploring the effect of coupling to an external heat bath [39]. In the following we will first explain how this device can be used for a quenching experiment, and then discuss its experimental feasibility.

3.2 Intersection of CPW with tunable coupler

A schematic of a CPW intersected with a tunable coupler is shown in fig. 3.2.

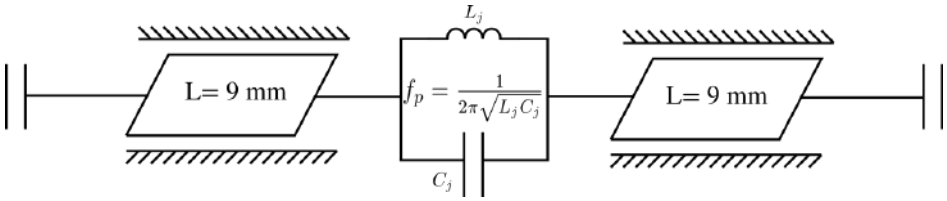

FIGURE 3.2: Schematic of a CPW interrupted by a LC circuit with a tunable inductance. By tuning the inductance we can change the coupling between the two resonators. In this chapter we explore how fast this should be to excite the groundstate.

The coupler is basically a parallel LC circuit with a tunable inductance. Such a tunable inductance can be easily realized by flux biasing a SQUID (see section 2.2). To explain how this device can be used for a ground state quenching experiment we simulated the spectrum of such a system using the circuit simulator `QUCS` [40]. The parameters we used can be found in table 3.1.

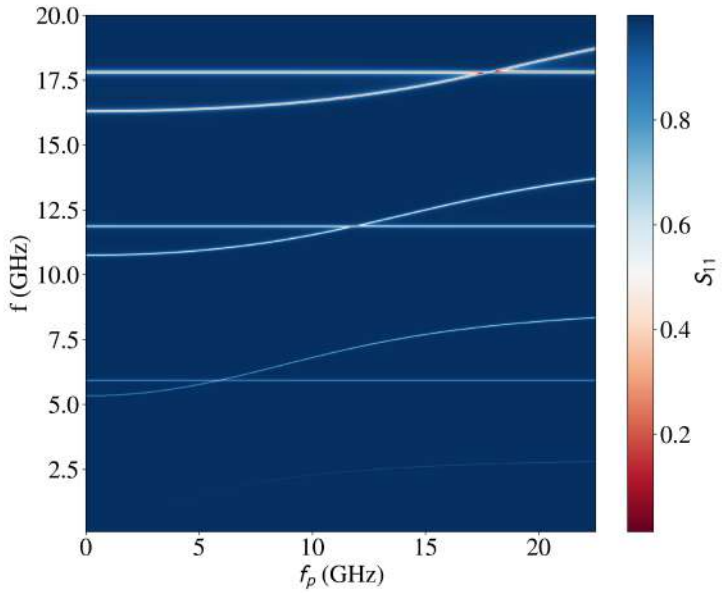

FIGURE 3.3: Reflection coefficients (S_{11}) of a CPW interrupted by a capacitively shunted inductor. Its resonance frequency f_p is changed by varying L_j. The lines independent of f_p are the odd harmonics of the CPW. The lines which do depend on f_p are the mixed modes between the even harmonics of the bare CPW and the inductors. At multiples of $f_p = 6\,\text{GHz}$ they cross each other and become degenerate. This spectrum was obtained with `QUCS` using the parameters of table 3.1

TABLE 3.1: QUCS parameters for simulating spectrum of CPW intersected with tunable LC circuit.

Parameter	Value	Parameter	Value
ℓ(mm)	9	C_c (fF)	25
v ($10^8\,\mathrm{m\,s^{-1}}$)	1.08	Q_{int}	280
f_0 (GHz)	3	Q_{ext}	730
Z_0 (Ω)	50	C_j (fF)	100

In fig. 3.3 the S_{11} reflection coefficients are shown. The junction is modelled as a linear inductor with inductance L_j, varying between ∞ and 1 nH. The inductor together with the capacitance behave like a LC-circuit with plasma frequency $f_p = \frac{1}{\sqrt{L_j C_j}}$.

The straight lines at multiples of $\bar{f} = 6\,\mathrm{GHz}$ are odd harmonics (first, third, sixth etc,) of the bare CPW. These modes have a flux node in the middle at the junction, and therefore a current anti node, as shown in fig. 3.4. Therefore they do not couple to the junction and are independent of f_p. The even harmonics of the CPW do have a finite current at the middle and therefore are modified by the junctions giving them a finite flux drop. They do depend on f_p and cross the straight lines exactly at $\bar{f}_p = 6\,\mathrm{GHz}$.

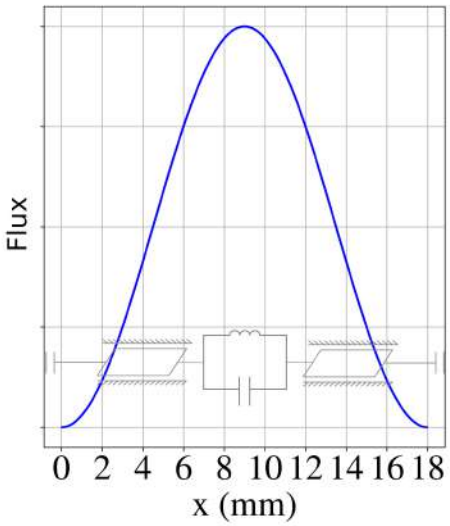

FIGURE 3.4: The first harmonic of the bare CPW has a current node at the capacatively shunted inductor and is therefore decoupled from it.

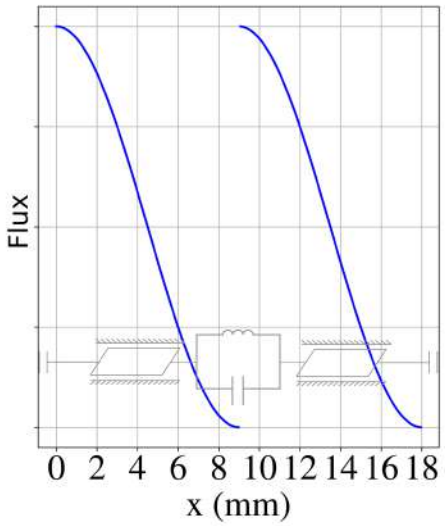

FIGURE 3.5: At $f_p = \bar{f}_p$ the capacatively shunted inductor has an impedance approaching infinity such that the CPW is split into two $\lambda/2$ resonators.

It it is insightful to consider three points, $L_j \to \infty$, $L_j = \frac{1}{C_j \bar{f}^2}$ and $L_j \ll \frac{1}{C\bar{f}^2}$. In the first case the inductor behaves as an open, therefore here the coupling between both resonators is purely capacitive. In the latter case, $Z_L \ll Z_C$ such that the coupling is purely inductive. When $L_j \to 0$ the inductor becomes a short and we are left with the unmodified even harmonics of the bare CPW.

The most interesting point is the crossing point in between where $L_j = \frac{1}{C\bar{f}^2}$. Here the capacitively shunted junction functions as a bandstop filter, having an impedance $Z = R_J$ at frequencies $f = f_p = \bar{f}$, which is virtually infinite. So the frequency where the

impedance becomes infinite matches exactly the eigenfrequency of one piece of CPW with two open ends ($\lambda/2$ resonator). As the coupling capacitances act as mirrors at GHz frequencies ($C_{coupling} \sim$ fF), each half of the CPW behaves as an independent $\lambda/2$ resonator, see fig. 3.5.

A typical quench experiment will start at $f_p = 0$ such that the two resonators are capacitively coupled. Then by suddenly bringing f_p to $\bar{f}$ the two are decoupled. The question we want to answer now is: how fast do we need to quench to excite the ground state?

3.3 Ground state quenching timescales

To determine how fast we should quench our system we write down our Hamiltonian modelling the CPW's as lumped element circuits, quantize and simulate the evolvement of the master equation in `QuTIP`. To this end we follow the approach of Devoret as explained in section 2.4.2 and introduce the generalized fluxes ϕ_a and ϕ_b as our coordinates, as shown in fig. 3.6 [18].

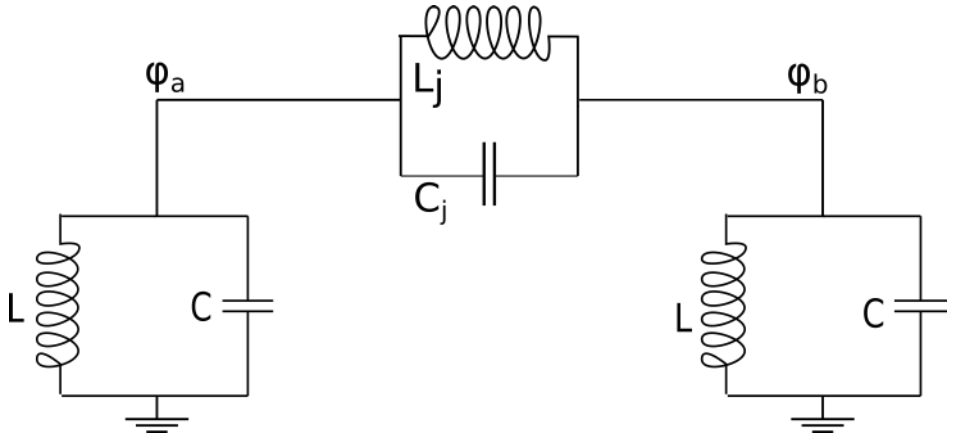

FIGURE 3.6: We model the CPW intersected by a tunable coupler as two LC circuits coupled by another LC circuit with a tunable inductor L_j. We chose ϕ_a and ϕ_b as our coordinates.

Now our Lagrangian becomes:

$$\mathcal{L} = T - V \tag{3.1}$$

$$= \frac{C}{2}\dot{\phi}_a^2 + \frac{C}{2}\dot{\phi}_b^2 + \frac{C_j}{2}\left(\dot{\phi}_a - \dot{\phi}_b\right)^2 - \frac{\phi_a^2}{2L} - \frac{\phi_b^2}{2L} - \frac{1}{2L_j}\left(\phi_a - \phi_b\right)^2 \tag{3.2}$$

We expect a symmetric and an antisymmetric solution, so we transform to $\phi_+ = \frac{\phi_a + \phi_b}{\sqrt{2}}$ and $\phi_- = \frac{\phi_a - \phi_b}{\sqrt{2}}$. Then we get:

$$\mathcal{L} = \frac{C}{2}\dot{\phi}_+^2 + \frac{C}{2}\dot{\phi}_-^2 + C_j\dot{\phi}_-^2 - \frac{\phi_+^2}{2L} - \frac{\phi_-^2}{2L} - \frac{1}{L_j}\phi_-^2 \tag{3.3}$$

$$= \frac{C}{2}\dot{\phi}_+^2 - \frac{\phi_+^2}{2L} + \frac{C + 2C_j}{2}\dot{\phi}_-^2 - \frac{L_j + 2L}{2LL_j}\phi_-^2 \tag{3.4}$$

Now our generalized momenta are $\pi_+ = \frac{\partial \mathcal{L}}{\partial \dot{\phi}_+} = C\dot{\phi}_+$ and $\pi_- = \frac{\partial \mathcal{L}}{\partial \dot{\phi}_-} = (C + 2C_j)\,\dot{\phi}_-$, and we find for our Hamiltonian:

$$H = \left(\sum \dot{\phi}_i \pi_i\right) - \mathcal{L} \tag{3.5}$$

$$= \frac{\pi_+^2}{2C} + \frac{\phi_+^2}{2L} + \frac{\pi_-^2}{2\,(C + 2C_j)} + \frac{L_j + 2L}{2LL_j}\phi_-^2 \tag{3.6}$$

Which is just the sum of two uncoupled harmonic oscillators with $f_+ = \bar{f} = \frac{1}{2\pi\sqrt{LC}}$ and $f_- = \frac{1}{2\pi}\sqrt{\frac{L_j+2L}{(C+2C_j)(LL_j)}}$. We are interested in the mode which involves the coupling, i.e. ϕ_-. To verify if our frequency makes sense we rewrite f_- as a function of f_p.

$$f_-^2 = \frac{\bar{f}^2 C + 2f_p^2 C_j}{C + 2C_j} \tag{3.7}$$

We directly see that at $f_p = \bar{f}$ the antisymmetric mode crosses the symmetric mode, i.e. $f_- = \bar{f}$ as we expect from our `QUCS` simulation. Using eq. (2.25) we plot f_- in our `QUCS` spectrum in fig. 3.7 :

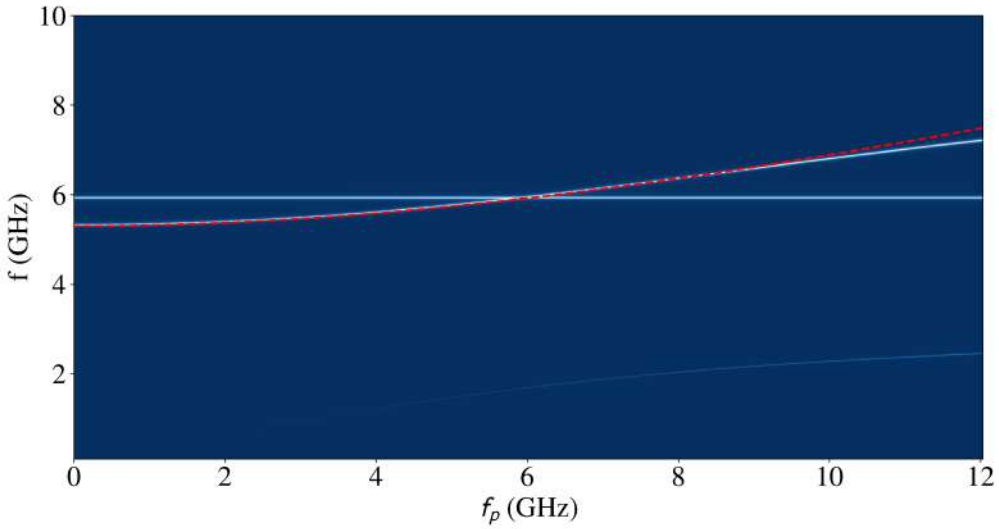

FIGURE 3.7: Plot of the frequency of the antisymmetric mode as obtained from our lumped element model (red dashed line) against our `QUCS` simulation which takes the distributed nature of the CPW into account. As expected it fits very well below $\bar{f}_p$. Above $\bar{f}_p$ it diverges as the lumped element model breaks down.

.

We see that below $\bar{f}$ our resonance frequency matches our `QUCS` spectrum really well. Above it starts to diverge. This is because in the limit $L_J \to 0$ our lumped element model behaves as two strongly coupled oscillators, for which the eigenfrequency scales linear with the coupling. Here the lumped element approximation brakes down, as two strongly coupled CPW's behave as one CPW. So in reality, in the limit $L_J \to 0$ the mode becomes one of the flat harmonics of the CPW (this is better visible in fig. 3.3).

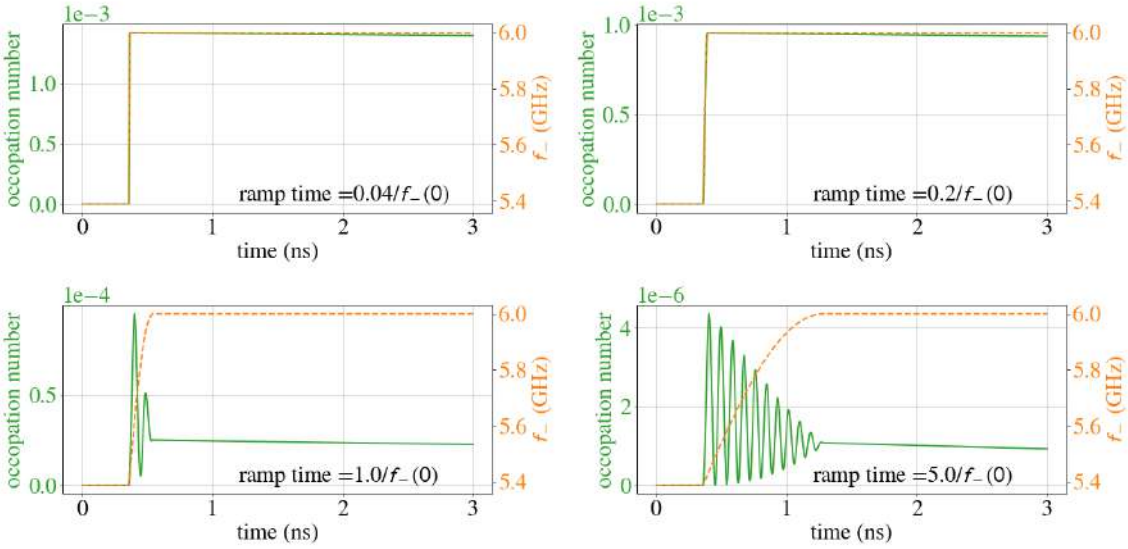

FIGURE 3.8: Occupancy of antisymmetric mode of two coupled harmonic oscillators with $\bar{f} = 6\,\text{GHz}$ prepared in its groundstate. The system is brought from $f_-(0) = 5.4\,\text{GHz}$ to 6 GHz, in four different times. To excite the system it must be quenched faster than $\frac{1}{f_-(0)}$.

Next we quantize the antisymmetric mode, by introducing $\hat{\pi}_- = \sqrt{\frac{hCf_-}{2}}\,(\hat{a}^+ - \hat{a}^-)$ and $\hat{\phi}_- = \sqrt{\frac{\hbar}{4\pi C f_-}}\,(\hat{a}^+ + \hat{a}^-)$, with $[\hat{a}, \hat{a}^+] = 1$:

$$\hat{H} = hf_- \left(\hat{a}^+\hat{a} + \frac{1}{2}\right) \tag{3.8}$$

As $f_- = f_-(f_p)$ and $f_p = f_p(t)$ we have reformulated our problem in quenching an harmonic oscillator. To simulate this in `QuTIP` we need to know the evolvement of the creation and annihilation operators. Following the approach of Ma and Rhodes [41] our time dependent creation and annihilation operator become:

$$\hat{a}^+(t) = \frac{f_-(t) + f_-(0)}{4\pi\sqrt{f_-(t)f_-(0)}}\hat{a}^+(0) + \frac{f_-(t) - f_-(0)}{4\pi\sqrt{f_-(t)f_-(0)}}\hat{a}^+(0) \tag{3.9}$$

Then our time dependent Hamiltonian becomes:

$$\hat{H} = \frac{\pi f_-(0)}{2}\left(\hat{a}^+\hat{a} + \hat{a}\hat{a}^+ - \hat{a}^+\hat{a}^+ - \hat{a}\hat{a}\right) + \frac{\pi f_-(t)^2}{2f_-(0)}\left(\hat{a}^+\hat{a} + \hat{a}\hat{a}^+ + \hat{a}^+\hat{a}^+ + \hat{a}\hat{a}\right) \tag{3.10}$$

Next we use the `QuTIP` function `mesolve` to solve the Schrödinger equation:

$$i\hbar\frac{d}{dt}\left|\Psi\right\rangle = \hat{H}\left|\Psi\right\rangle \tag{3.11}$$

We set $|\Psi\rangle$ at $t = 0$ to the ground state $|0\rangle$ and allow for a maximum number of photons of $N = 20$. We simulate a quenching experiment by preparing our system in its ground state and change f_p from $f_p = 0$ to $f_p = \bar{f} = 6\,\text{GHz}$. We use a capacitance of $C_j = 100\,\text{fF}$ which means that the frequency of the antisymmetric mode changes from $f_-(0) = 5.4\,\text{GHz}$ to $f_- = \bar{f} = 6\,\text{GHz}$. This corresponds to an initial coupling g_0:

$$g_0 \sim \frac{\bar{f}^2 - f_-(0)^2}{4\bar{f}} = \bar{f}\frac{C_j}{2(C+2C_j)} \approx 300\,\mathrm{MHz} \tag{3.12}$$

We plot time traces for four different quenching times shown fig. 3.8. We see that we need to to quench faster than $\frac{1}{f_-(0)}$ to get a significant excitation. Still, we would get an occupation number of only 0.001.

In fig. 3.9 we plot the steady state occupation number as function of g_0 for four different quenching times compared to $f_-(0)$.

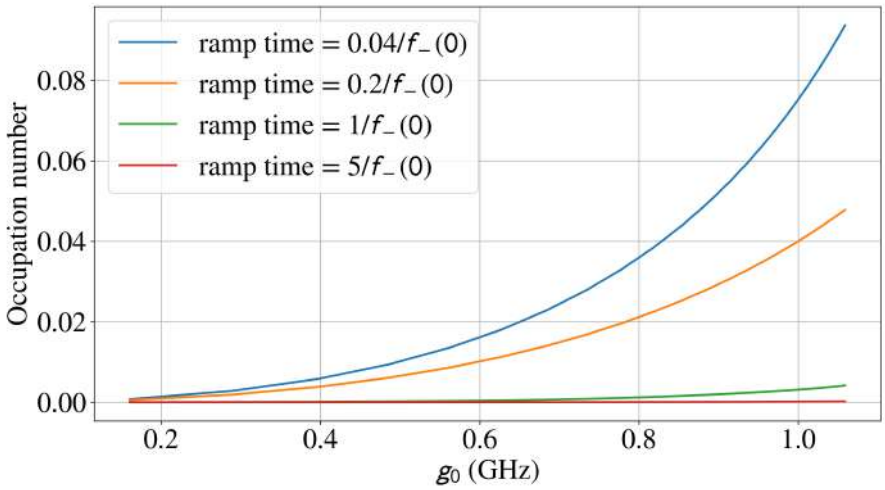

FIGURE 3.9: Steady state occupation number after the quench for different initial couplings g_0, plotted for four different quenching times compared to $f_-(0)$. The higher the coupling, the higher the excitations. At lower couplings quenching has no effect and the occupation number is zero.

As expected, increasing the coupling g_0 will increase the occupation number. Furthermore, we observe that the effect of faster quenching is stronger at higher couplings. The rising time of an Arbitrary Waveform Generator (AWG) depends on its bandwidth, and is typically in the order of nanoseconds. We conclude that a ground state quenching experiment with the proposed device will be experimentally challenging because we find that we need to quench faster than $1/f(0)$ which requires sub-nanosecond timescales. Second, to achieve a high coupling we need capacitors in the order of $\sim$ pF which adds extra complexity to the fabrication process.

Finally, we consider the more general case of quenching two linear coupled harmonic oscillators and simulate again the dynamics using `QuTIP`:

$$\hat{H} = \hbar\omega\left(\hat{a}^+\hat{a} + \frac{1}{2}\right) + \hbar\omega\left(\hat{b}^+\hat{b} + \frac{1}{2}\right) + \hbar g\left(\hat{a}^+ + \hat{a}\right)\left(\hat{b}^+ + \hat{b}\right) \tag{3.13}$$

We again show the time traces with $g_0 = 300\,\mathrm{MHz}$ fig. 3.10. Again the oscillator frequency determines the quenching timescale. For the 'fast' quenching times the excitation number in this model lies in the same order as our previous model, for 'slower' times it predicts a higher value. We also observe that now the fast oscillations at 12 GHz are modulated by a slower oscillation with $f = 4g_0$.

We also calculated the steady-state occupation numbers for different g_0 and different quenching times, plotted in fig. 3.11. The steady state occupation number lies in the same

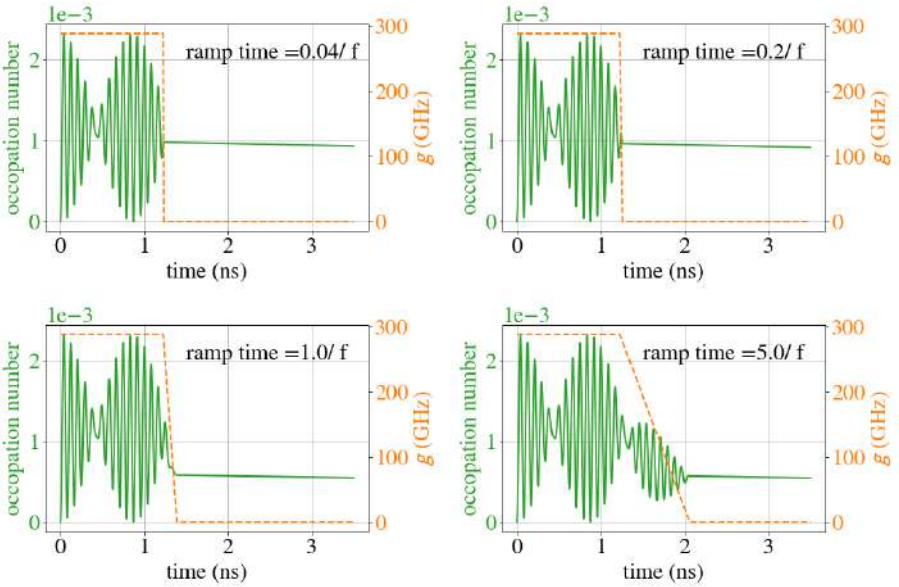

FIGURE 3.10: Decoupling two coupled harmonic oscillators on resonance in the ground state with $f = 6\,\mathrm{GHz}$. The ground state occupancy exhibits fast oscillations at $2f$ modulated by a slower oscillation at $4g_0$. The dashed curve shows the coupling $g(t)$ as a function of time. The quenching must happen much faster than $1/f$ to achieve the highest excitations possible.

order of magnitude as our previous model, but differ in two ways. At low couplings the values for fast quenching times lie much higher, and they show oscillatory behaviour. This can be explained by the fact that the time traces are modulated by g_0 such that the steady state occupation number depends on the moment we quench. As we keep this constant but shift g_0, we get an oscillation. In summary, the experimental challenges we found from our previous model hold in general for ground state quenching linear coupled oscillators.

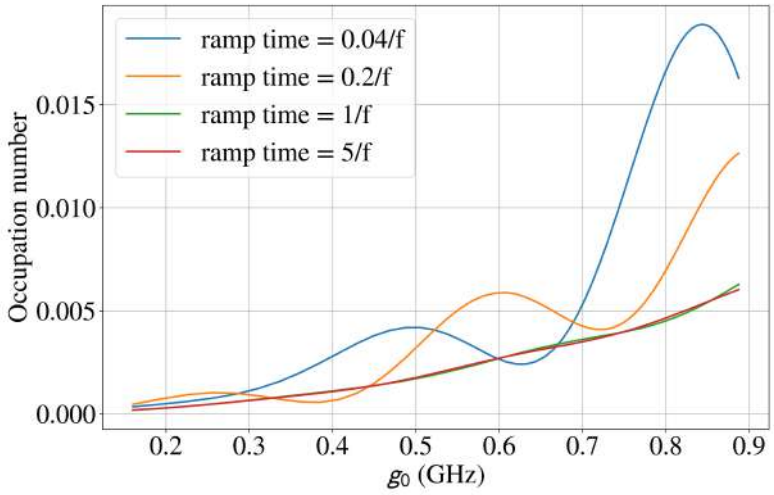

FIGURE 3.11: Steady state occupation number after quenching the coupling of two linear coupled oscillators with frequency $f = 6\,\mathrm{GHz}$ for different initial couplings g_0, plotted for four different quenching times compared to f. The higher the coupling, the higher the excitations.

Chapter 4

Josephson Crystal: Design, fabrication and experimental setup

We designed an experimental realization of a Josephson crystal based on a proposal by Hartmann and Leib [9]. This circuit consists of a coplanar waveguide regularly interrupted by capacitively shunted Josephson junctions at distances comparable to microwave lengths, shown in fig. 4.1. This device exhibits ultra strong coupling between the junctions and the cavity modes, as the junctions are directly placed inside the central conductor.

It is predicted that the band-structure becomes degenerate when the plasma frequency of the Josephson is equal to the frequency of a single CPW. Furthermore, the system makes a sharp transition when it is tuned at the degeneracy point and driven by a red-detuned drive. In that case some modes synchronously switch from low occupancy to a high occupancy, first responding with a π-delay to the drive ending up in phase with the drive.

In this chapter first we review the main theoretical predictions of the work of Leib, then we explain the process of designing, fabricating and measuring an cQED realization of the Josephson crystal.

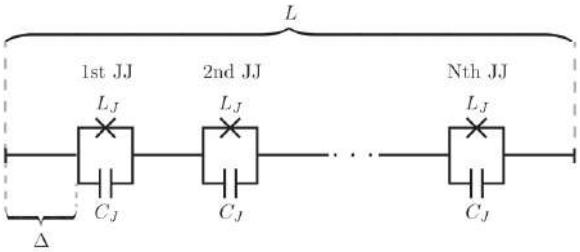

FIGURE 4.1: Central conductor of CPW interrupted by N uniformly distributed Josephson junctions, shunted with a capacitor L_j. Proposal by Leib and Hartmann [9].

4.1 Spectrum and off-resonant driving of the Josephson crystal

In fig. 4.2 the analytical solutions of the spectrum of a CPW intersected with three capacitively shunted junctions at equal spacing are shown [9]. The spectrum for N junctions is is given by:

$$\frac{\cos\left(\frac{\omega}{v}\Delta\right) - \cos\left(n\frac{\pi}{N+1}\right)}{\sin\left(\frac{\omega}{v}\Delta\right)} = \frac{cv\pi}{2C_j}\frac{\omega}{\omega_p^2 - \omega^2} \tag{4.1}$$

Here $\omega_p = 2\pi f_p = \frac{1}{L_j C_j}$ is the plasma frequency of the junctions. As with the CPW interrupted by one junction the odd harmonics of the CPW stay unmodified due to their

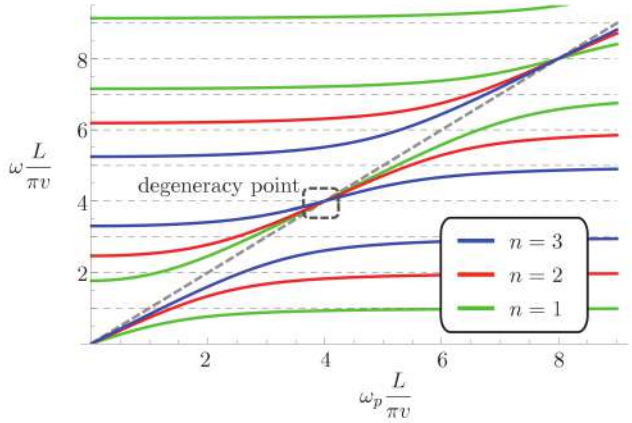

FIGURE 4.2: Classical eigenspectrum of CPW intersected with $N = 3$ equally spaced capacitively shunted Josephson junctions as calculated by Leib et al. [9]. Here $L = 28\,\mathrm{mm}$, $v = 0.98 \times 10^8\,\mathrm{m\,s^{-1}}$, $C_j = 1\,\mathrm{pF}$. The system exhibits a degeneracy point at plasma frequencies $f_p = k\frac{(N+1)\omega L}{\pi v}$.

current nodes at the junctions (see section 3.2). These are left out of the spectrum. Again we can distinguish a capacitive regime at $L_j \to \infty$, an inductive regime ($L_j \ll \frac{1}{C_j \bar{f}^2}$), and degeneracy point $L_j = \frac{1}{C_j \bar{f}^2}$ where the plasma frequency f_p equals the frequency of an odd harmonic $\bar{f} = k\frac{(N+1)\omega L}{\pi v}$. Here the device becomes subdivided into five $\lambda/2$ resonators.

We can gain some more understanding by viewing the Josephson crystal as two sets of harmonic oscillators (the bare CPW modes and N_j LC circuits), coupled to each other with a coupling g. When the two systems would be completely decoupled ($g \to 0$) the spectrum would consist of flat lines at the bare CPW eigenfrequencies ($f_{\mathrm{CPW}} = \frac{nv}{2\Delta}$ with Δ the length of one piece of CPW), and a straight line $f = f_p$ crossing them. By turning on the coupling the modes of the CPW and the junction with frequencies $|f_p - f_{CPW}| \sim g$, the crossings split into a low frequency and high frequency mode. Those branches cross at the degeneracy point, where the plasma frequency match exactly the resonance frequency of a single piece of CPW. Those are plotted in fig. 4.3a.

The quantization of these mixed modes gives a set of harmonic oscillators quantized with the operator $\hat{a}_n$. Then a transformation is applied to a base where the flux drops over the

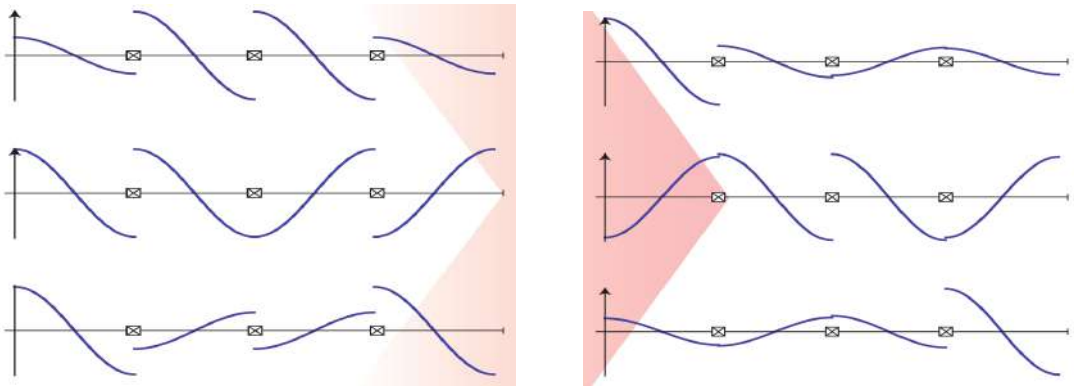

(A) (B)

FIGURE 4.3: **A** Modes at the degeneracy point in arbitrary units for a device with $N_J = 3$ junctions. **B** Transformed modes at the degeneracy point minimizing the flux drop across the junctions. Picture adapted from [9].

junctions is minimized, as shown in fig. 4.3b:

$$\hat{b}_j = \sqrt{2/(N+1)} \sum_{n=1}^{N} \sin(jp_n)\hat{a}_n \tag{4.2}$$

Then non-linearity is added as a perturbation. This gives the following Hamiltonian at the degeneracy point:

$$H = \sum_{j=1}^{N} \left[h\bar{f} b_j^\dagger b_j - \frac{E_c}{2} b_j^\dagger b_j^\dagger b_j b_j \right] - E_c \sum_{j,l}^{N} g_{j,l} \left(\left(b_j^\dagger b_j^\dagger b_j + b_j^\dagger \right) b_l \right) \tag{4.3}$$

With $E_C = \frac{e^2}{2C_j}$, $g_{j,l} = (2/N+1)\sum_{n=1}^{N} \sin(jp_n)\sin(lp_n)\left[\frac{\lambda(f_n)}{\lambda_0} - 1\right]$, $p_j = \frac{\pi j}{N+1}$ and $\lambda_0 = \sqrt{\frac{\hbar}{4\pi C_j f_p}}$ which is the ZPF of a single JJ. The flux fluctuations of each mode are given by:

$$\lambda = \sqrt{\frac{\hbar}{4\pi C_j f_p \left(1 + \frac{\Delta c}{4C_j}\left[1 + \cos\left(n\frac{\pi}{N+1}\right)\right]\right)}} \tag{4.4}$$

The first term in square brackets in eq. (4.3) represents a set of non-linear oscillators with a self-Kerr non-linearity of $\frac{E_c}{2}$. The second term represents the nonlinear inter mode couplings. Now, the following Hamiltonian is added to represent the drive:

$$H_{\text{drive}} = i\hbar \sin(\omega_d t) \sum_j \Omega_j \left(b_j - b_j^\dagger \right) \tag{4.5}$$

Here, Ω_j is an effective driving strength:

$$\Omega_j = \frac{\Phi}{\sqrt{\frac{N+1}{hf_p C_c^2}}} \sum_{n=1}^{N} \sin(np_j)/(\hbar\sqrt{\eta_n}) \tag{4.6}$$

Here Φ is the drive amplitude and η_n the effective mode capacitance [42]:

$$\eta_n = \frac{Lc}{2\sin(p_n)^2 \left(1 + \cos(p_n) + \frac{4C_j(N+1)}{Lc}\left(1 + \cos(p_n)^2\right)\right)} \tag{4.7}$$

Then, the following master equation was solved by a mean field simulation for a red detuned drive with $f_d = \bar{f} - 4E_c/h$:

$$\frac{i}{\hbar}[H, \rho] = \sum_n \frac{\kappa}{2}[2b_n \rho b_n^+ - \rho b_n^+ b_n - b_n^+ b_n \rho] \tag{4.8}$$

The result published by Leib in his paper is shown in fig. 4.4. At a certain power Ω^* most modes become suddenly populated. The explanation given by Leib and Hartmann goes as follows. Without the coupling we would have a set of nonlinear oscillators with a power dependent energy shift (because of the negative Kerr non-linearity). Then we would expect the modes to suddenly become populated at different driving strengths because of the mode dependent driving amplitudes. The effect of the inter mode coupling g is that modes in the same phase amplify each other. Therefore when the first mode tries to switch it is weighted down by the other modes. However, when the majority is switched, they drag the other modes with them.

Our goal is to experimentally observe the synchronization. Therefore we designed and fabricated a Josephson crystal. In the next section we describe our design considerations.

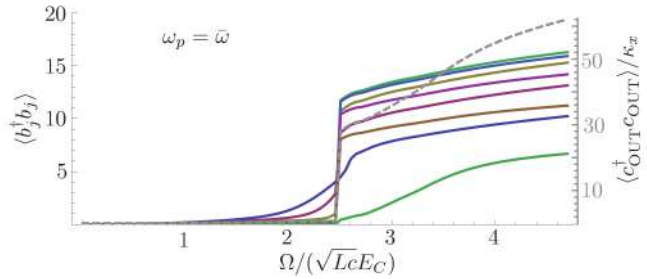

FIGURE 4.4: Modes occupation when driving a Josephson Crystal off-resonant. By increasing the driving strength the modes tuned at the degeneracy point suddenly become populated. Here $N = 8$ junctions are simulated, with $v = 0.98 \times 10^8\,\mathrm{m\,s^{-1}}$, $C_j = 1\,\mathrm{pF}$ and $L = 5.2\,\mathrm{mm}$.

4.2 Designing the Josephson crystal

The final device with five capacitively shunted junctions is shown in fig. 4.5. This section will go through all the design considerations and fabrication techniques of the different parts of the device: the transmission lines, the capacitively shunted junctions together with the flux lines, the coupling capacitors and the ground plane. Before we do this, we first briefly describe the printed circuit board (PCB), functioning as a bridge between the crystal and microwave setup, as its dimensions and placement of the launchers constrain the rest of the design. Finally we describe the microwave setup surrounding the chip which we use for cool down, driving and read-out.

We also made a chip with a crystal interrupted by three junctions and one with only one junction. The design considerations are the same as with the five junction device, see appendix A.

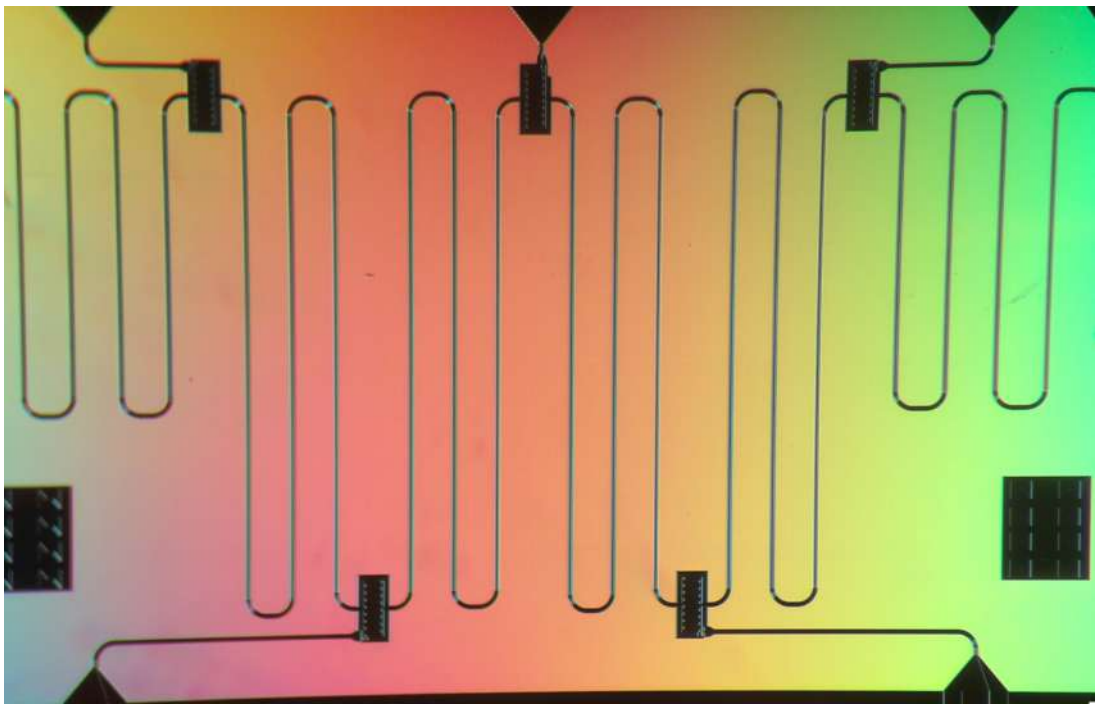

FIGURE 4.5: Design of our Josephson crystal featuring five capacitively shunted junctions (black rectangles) connected by 9 mm CPW's. The triangles are the launchers connecting the chip to the PCB.

4.2.1 PCB

The printed circuit board (PCB) connects the chip with the Josephson crystal to the microwave setup we use to drive and readout our device. The PCB consists of eight lines leading to the pocket in the middle of 4 mm by 7 mm as shown in fig. 4.6 were we place the device. These lines connect the chip via wire bonds to the microwave setup using SMP connectors. One of them will be connected to the drive and one will be used for readout. We use the six lines left to flux bias our junctions, which we shunt with a second junction to make the inductance flux dependent (see section 4.2.3).

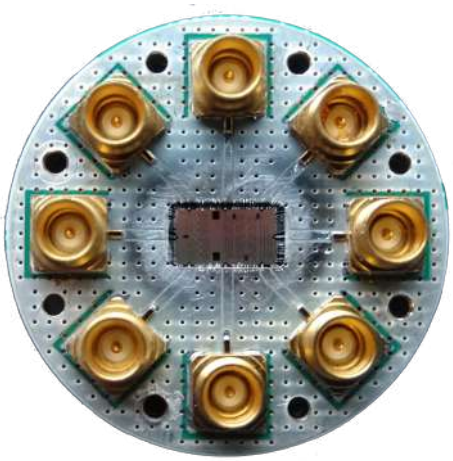

FIGURE 4.6: The chip is placed in the central pocket of the PCB. The eight lines connect the chip via wire bonds to the microwave setup using SMP connectors. Two of these lines are used for driving and read-out, the other six can be used for flux biasing the junctions.

4.2.2 Transmission lines

The shape of the transmission lines is not only constrained by the shape of the PCB but also by the frequency range we can operate in, according to eq. (2.16). The requirement that the modes are not populated by thermal excitations imposes a lower bound of one gigahertz (1 mK $\sim$ 20 MHz). The upper bound comes from the superconducting energy gap, which for aluminum is about fifty gigahertz. In our setup, this range is further reduced by the electronics being optimized to operate between 4 GHz and 8 GHz.

For the central pin and the ground plane we use 0.2 µm thick NbTiN with a critical temperature of $T_c = 14.5\,\mathrm{K}$ and a resistivity $\rho = 1.23 \times 10^{-6}\,\Omega\,\mathrm{m}$, etched on a 500 µm Silicon wafer with $\epsilon_r = 11.45$ at low temperature. To make the CPW have a standard impedance of $50\,\Omega$, we set the width of the central pin to $w = 12\,\mu\mathrm{m}$ and vary the gap until we have the right impedance, according to eq. (2.7) and eq. (2.8). The gap also determines the capacitance per unit length, inductance per unit length and phase velocity, as explained in section 2.1.2. The values we found are shown in table 4.1.

We wrote a python script drawing the CPW's in a GDS file using the `GDSCad` [43] package. Like this, we fully parameterized our design, allowing us to vary positions and dimensions until everything satisfied the constraints. This is further explained in section 4.2.5. We were able to fit five junctions on the chip with the CPW having a length of $L = 9\,\mathrm{mm}$, corresponding to $\bar{f} = 6\,\mathrm{GHz}$.

TABLE 4.1: Parameters of CPW's we use for our experimental realization of the Josephson crystal

Total length L	54 mm
width W	12 µm
gap G	4 µm
capacitance per unit length c	$0.18\,\mathrm{nF\,m^{-1}}$
inductance per unit length l	$0.46\,\mathrm{\mu H\,m^{-1}}$
phase velocity v	$1.08 \times 10^8\,\mathrm{m\,s^{-1}}$
resonance frequency $\bar{f}_p$	6 GHz

4.2.3 Capacitively shunted junctions

Capacitors

The capacitance C_J is chosen to optimize the non-linear inter mode couplings, encoded in the off-diagonal elements of the g-matrix given by eq. (4.3). From fig. 4.7 we see that these have an optimum around $C_j = 200\,\mathrm{fF}$.

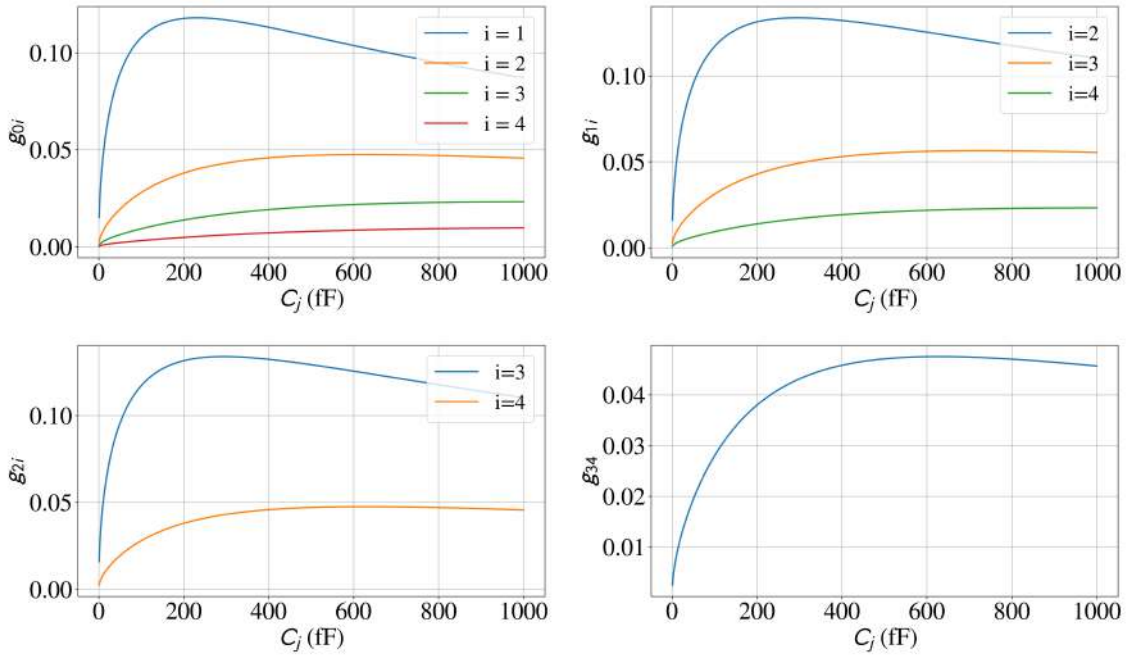

FIGURE 4.7: The non-linear intermode couplings encoded in the off-diagonal elements of g_{ij}, depend on the capacitance C_j and have a maximum around 200 fF. Each graph shows a different row of g_{ij}. A value of 1 means that the non-linear interaction is comparable to the self-Kerr interaction.

To get a capacitor with a capacitance close to this value we design an interdigitated capacitor. The EM analysis tool `Sonnet` [44] is used to parametrize the capacitor by its gap width and finger length, and to measure the reflection coefficient as a function of frequency. From the resonance frequency, we need to separate the capacitance and the parasitic inductance. To this end we add an extra inductor between the top fingers and measure the resonance for two different inductances, leaving us with two equations and two unknowns.

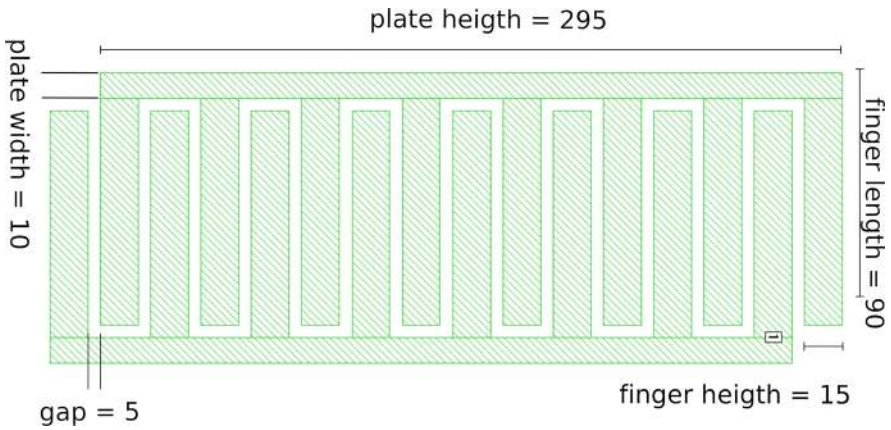

FIGURE 4.8: Design of capacitor shunted with the Josephson junctions. The measurements are in µm

From this, we find a capacitance of 135 pF and a self inductance of 0.29 nH for the parameters shown in fig. 4.8. This yields a self resonance at 25 GHz, far away from the 4 GHz to 8 GHz range we are looking at.

Next, the zero point flux fluctuations of the junctions should be lower than the flux quantum $\phi_0 = \frac{\hbar}{2e}$ in order to reduce charge noise [42]. The fluctuations around the first degeneracy point are given by eq. (4.4). We find that in our case the fluctuations are 5.5 times smaller than a quantum of flux.

Junctions

The fabrication process inevitably introduces variation in E_j and E_c between different capacitively shunted junctions. To correct for this and to probe the spectrum around the degeneracy point $\bar{f} = 6$ GHz, we make the Josephson energy E_j tunable by adding an extra junction in parallel, according to eq. (2.46).

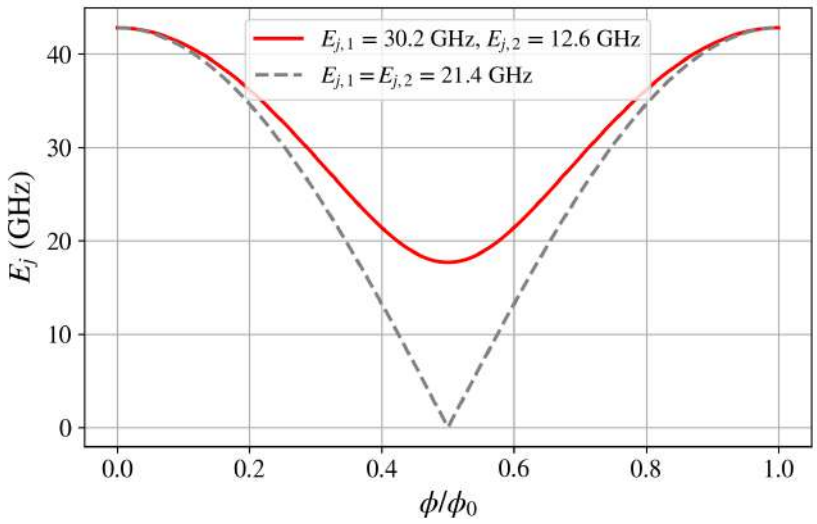

FIGURE 4.9: By shunting our junctions with a second junction we make the total E_j tunable as a function of the magnetic flux ϕ. To set a lower bound, we chose to use two junctions with different E_j,shown in red. In grey the curve corresponding to the symmetric case is drawn.

When two identical junctions are used (α =0), E_j modulates between $E_{j,1} + E_{j,2}$ and 0. By making them asymmetric we can set a lower bound $E_{j,1} - E_{j,2}$, shown in fig. 4.9.

This makes them less susceptible to flux noise, and allow for more precise tuning. Approximating the capacitively shunted junction by a linear LC circuit with frequency $f = \frac{1}{2\pi\sqrt{LC}}$ and using that $E_j = \left(\frac{\phi_0}{2\pi}\right)^2 / L_j$ we can translate these extrema into a frequency range around the degeneracy point. We find that for the junctions to be tunable between 4.5 GHz and 7 GHz we need $E_1 = 12\,\text{GHz}$ and $E_2 = 30\,\text{GHz}$.

In fig. 4.10 we show an optical image of the SQUID shunted with the capacitor. On the left there is a fluxline delivering a constant DC current parallel to the loop. Like this, a constant magnetic flux threads the loop, allowing for tuning the resonance frequency of the coupler during the experiment.

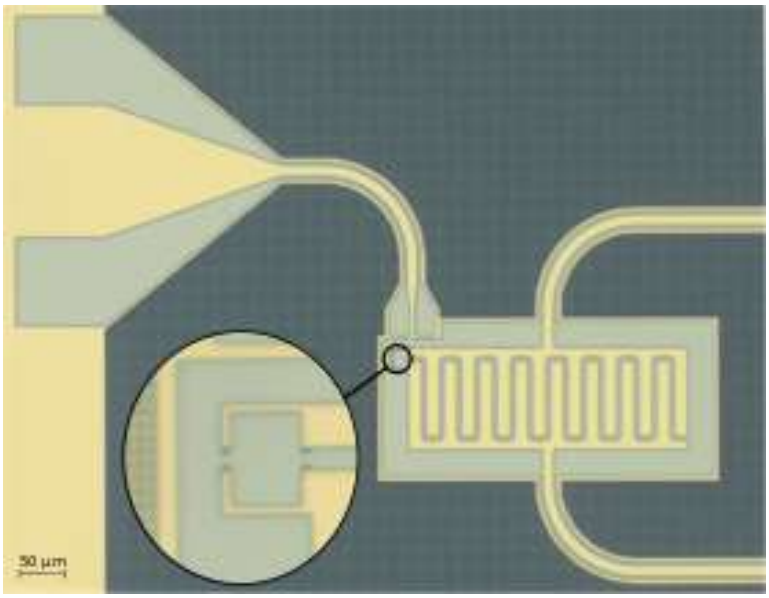

FIGURE 4.10: SQUID loop (shown in the zoom) shunted with a capacitor. On the left side a fluxline is shown which delivers a DC current parallel to the loop. This creates a constant magnetic flux through the loop, allowing us to tune the resonance frequency of the coupler in situ.

4.2.4 Coupling capacitors

Our device is coupled to the outside world by two coupling capacitors with capacitance C_c. These capacitors enable us to drive and measure the system, but introduce extra loss to the outside world, quantified by Q_{ext} (see also section 2.1.4). We want our device to be to critical coupled to have both a high SNR and high coherence, so we require $Q_{\text{ext}} = Q_{int}$. To be on the safe side, we approach from below ($Q_{\text{ext}} \leq Q_{int}$) ensuring us to be at least undercoupled. Based on measurements with reference resonators we estimate Q_{int} to be around $Q_{\text{ext}} = 10^5$.

To estimate Q_{ext} as a function of C_c, we made a linear model of our device in the circuit simulator `QUCS` [40]. In this model losses in the CPW are modelled by an attenuation constant, as explained in section 2.1.1. Losses in the couplers can be modelled by shunting them with a resistance. Then we do a frequency sweep for different capacitances C_c. By fitting eq. (2.39) we derived the external quality factor shown in fig. 4.11a.

We make our capacitances by simply leaving a gap in the centre conductor. To translate this gap to the capacitance we need, we again use `sonnet` with a similar trick. The result is shown in fig. 4.11b. We find we need a gap of 12 µm to be critically coupled.

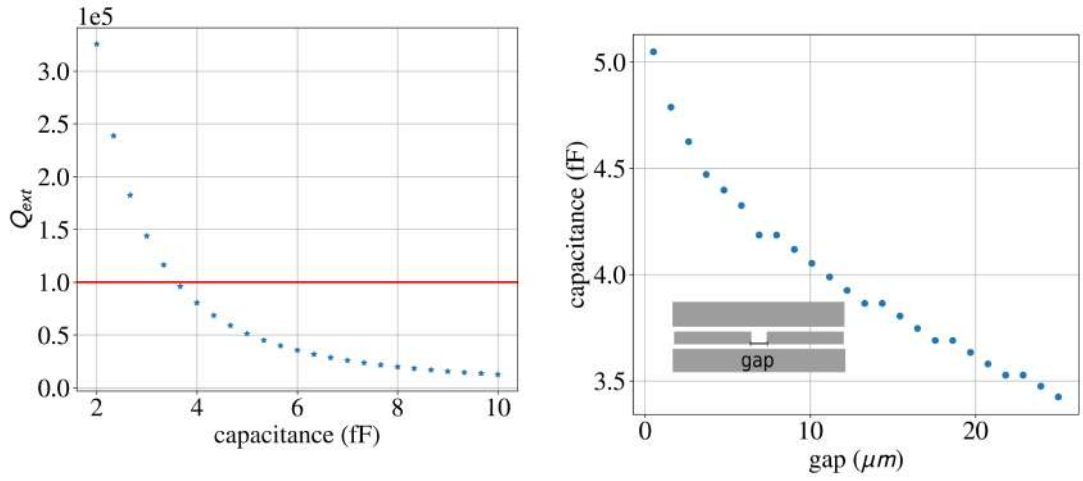

(A) (B)

FIGURE 4.11: **A** The external quality factor Q_{ext} scales inversely with the coupling capacitance C_c. The red line shows our estimation of the internal quality factor. The crossing marks the condition for critical coupling. **B** The capacitance of a CPW with the central conductor interrupted by a gap as a function of the gap size. We find we need a gap of 12 µm to be critically coupled.

4.2.5 Designing circuits in `Python`

We designed our circuit fully in `Python` using the `gdsCAD` package [43]. With `gdsCAD` one can view and create GDSII layout files, the standard file format for integrated circuit masks. Its building blocks are Cells containing one or more objects. Objects be grouped as an element, which allows for transforming them all at once, like translation or rotation. The Cells are added to a so-called Layout which then can be saved as a GDSII file. The package contains a number of predefined basic geometries like rectangles, polygons and circles. In addition to `gdsCAD` we used the `stcad` package [45], a collection of `Python` scripts with more sophisticated structures like coplanar waveguides build from `gdsCAD` objects.

As an illustration we show a minimal working example drawing an L-shaped block:

```
import gdsCAD as cad
from stcad.source_dev.chip import Base_Chip
from stcad.source_dev import objects

## system parameters
path = '/example/minimal_working'
chipsize_x = 2e3
chipsize_y = 2e3

chip = Base_Chip(name, chipsize_x, chipsize_y)

block = cad.core.Boundary( [(-500, -500), (-500,500), (200,500), \
(200, 200), (500, 200), (500, -500)], layer=1)
cell = cad.core.Cell('Example')
cell.add(block)
chip.add(cell, origin=(0,0))
chip.save_to_gds( save=True,loc=path)
```

First a chip is created using Base_Chip, defined in `stcad` as follows:

```
class Base_Chip(cad.core.Cell):
    def __init__(self, name, xdim=1000, ydim=1000):

        super(Base_Chip, self).__init__(name)
        self.name = name
        self.xdim = xdim
        self.ydim = ydim
        self.boxwidth = 100

        self.make_layout()

    def make_layout(self):
        """
        Generate chip with dimensions xdim,ydim
        """
        box=cad.shapes.Box((-self.xdim/2, -self.ydim/2), (self.xdim/2, self.ydim/2),
                           width=self.boxwidth, layer =self.layer_box)
        date = time.strftime("%d/%m/%Y")
        self.add(box)

    def save_to_gds(self, loc = 'examples/', save = True, show = False):
        """
        Save and show gds file
        """
        layout = cad.core.Layout('MAIN_CHIP')
        layout.add(self)
        if save:
            layout.save(loc + self.name + '.gds')
```

Base_Chip inherits the Cell class and thus is a Cell itself. To define the boundaries of the chip a box is drawn. After the chip is instantiated we draw a L-shaped block using the `gdsCAD` boundary object. This object is added to a Cell, which in turn is added to the chip. Then, so save to GDSII a Layout is created, the chip is added and saved as GDSII. The result is shown in fig. 4.12.

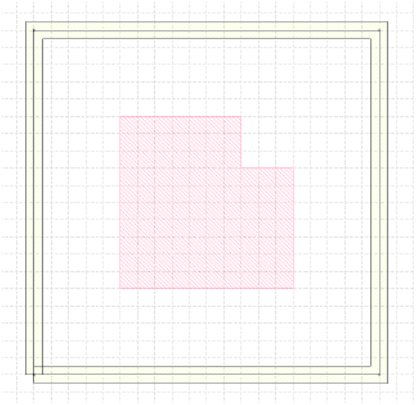

FIGURE 4.12: Example of drawing objects in `gdsCAD`. The yellow border marks the edge of the chip.

During the project, we added an interdigitated capacitor object with the option to include a SQUID to `stcad`. New functions for the CPW object (called 'methods' in object oriented programming) were written too, to add airbridges and to add a boundary between the CPW and the ground plane, called 'skirts'. These can be found in appendix B.

To draw the transmission lines we use the CPW object from `stcad`, which draws a transmission line using the `gdsCAD` boundary object. For this it needs the coordinates of beginning point, end point and bends. Because each CPW must have the same length in our case, we wrote a function called 'CPWcoor' which takes as input the coordinates of the beginning and the end, the total length, number of bends and starting length. Furthermore the initial direction can be given as 'north' (n), 'south' (s), together with the direction of the end, which can be 'horizontal' (h) and 'vertical' (v). It returns the coordinates passed to the CPW object such that we can quickly generate different types of CPW's with the same length. This is illustrated in fig. 4.13.

The file which finally generates the chip can be found in appendix B. It is structured as follows. First a list with the coordinates of the launchers is created. Then we make a second list were we parameterize the coordinates of the capacitively shunted junctions, defined by the points where the CPW meets the capacitor. From those two list, the beginning en ending points of the CPW are determined and saved in a third list. The CPW's are then instantiated using our CPWcoor function and the CPW object. Now we can easily shift a capacitor, add an extra bend or adjust the length of the CPW because our design is parameterized such that everything stays connected to each other. Finally, because we designed the airbridge method of the CPW object such that the airbridges are specified by a density, we can easily add or remove airbridges and add skirts.

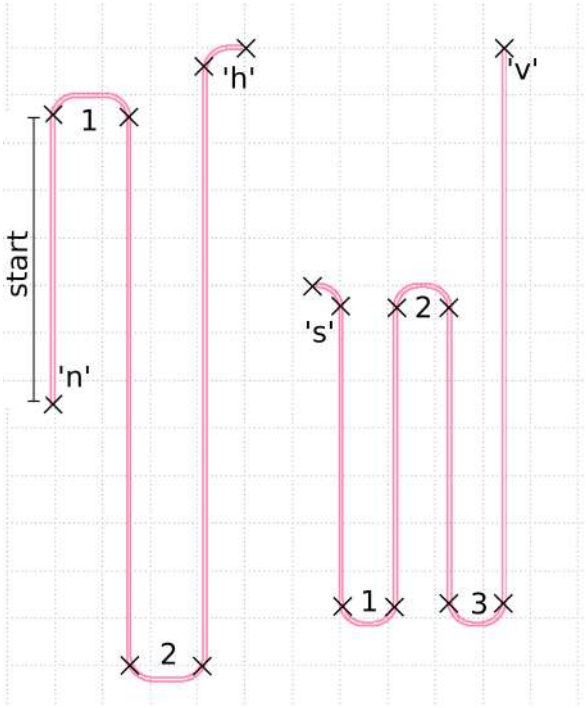

FIGURE 4.13: Two CPW's with coordinates generated with the python function 'CPWcoor', indicated with a cross. As input it takes the total length, the starting length, the begin and end coordinates, the number of bends and the direction of the first and last segment. Like this we can create very fast different types of CPW's with the same length.

4.3 Fabrication

The fabrication happens in two stages. In the first stage the metallic structures (transmission lines, capacitors and squid arms) are made by e-beam lithography and reactive ion-etching on a 500 µm Silicon wafer with 0.2 µm NbTiN on top. In this step also a grid of holes is made in the ground plane to trap unwanted magnetic vortices.

Then in the second stage, the junctions are made from Al/AlOx/Al by the Dolan bridge method [46]. To make junctions with the energies we calculated in section 4.2.3 , we fabricated an array of junctions with a width ranging from 10 µm to 500 µm. Then we measured its normal state resistance R_n which scales inverse with E_j according to the Ambegaokar-Baratoff

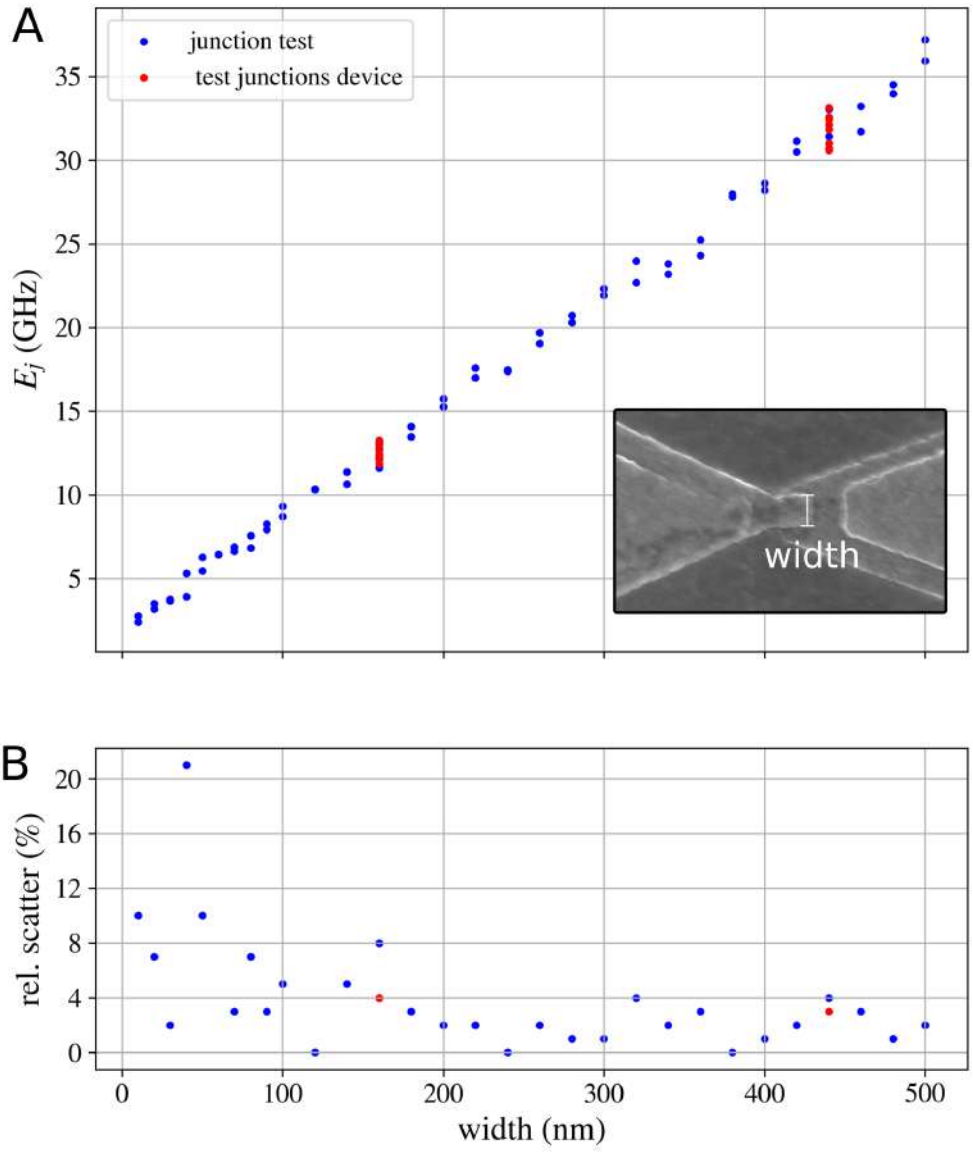

FIGURE 4.14: **A** E_j as function of junction width for a gap of 120 nm. The red dots show extra measurements done with the width we use for our device (160 nm and 440 nm). **B** Relative scatter in E_j for different width is around 3%. At small width the energies show a wider spread.

formula [47] $E_j = \frac{h\Delta_{\mathrm{al}}}{8e^2 R_n} = 140\,\mathrm{GHz}\,\Omega/R_n$, with Δ_{al} superconducting energy gap of Aluminium. The results are shown in fig. 4.14 together with the relative scatter which for our parameters amounts to 4%. From this we estimate our lower frequency to $f_l = (4.8 \pm 0.2)\,\mathrm{GHz}$ and our upper frequency $f_u = (7.1 \pm 0.1)\,\mathrm{GHz}$.

4.4 Experimental setup

In a first round of experiments we cooled down the device with the three junction crystal and one junction crystal in a BlueFors LD dilution refrigerator. The refrigerator consists of different stages place above each other. The lowest stage has a temperature of $T < 10\,\mathrm{mK}$. This, together with the wiring diagram is shown in fig. 4.15.

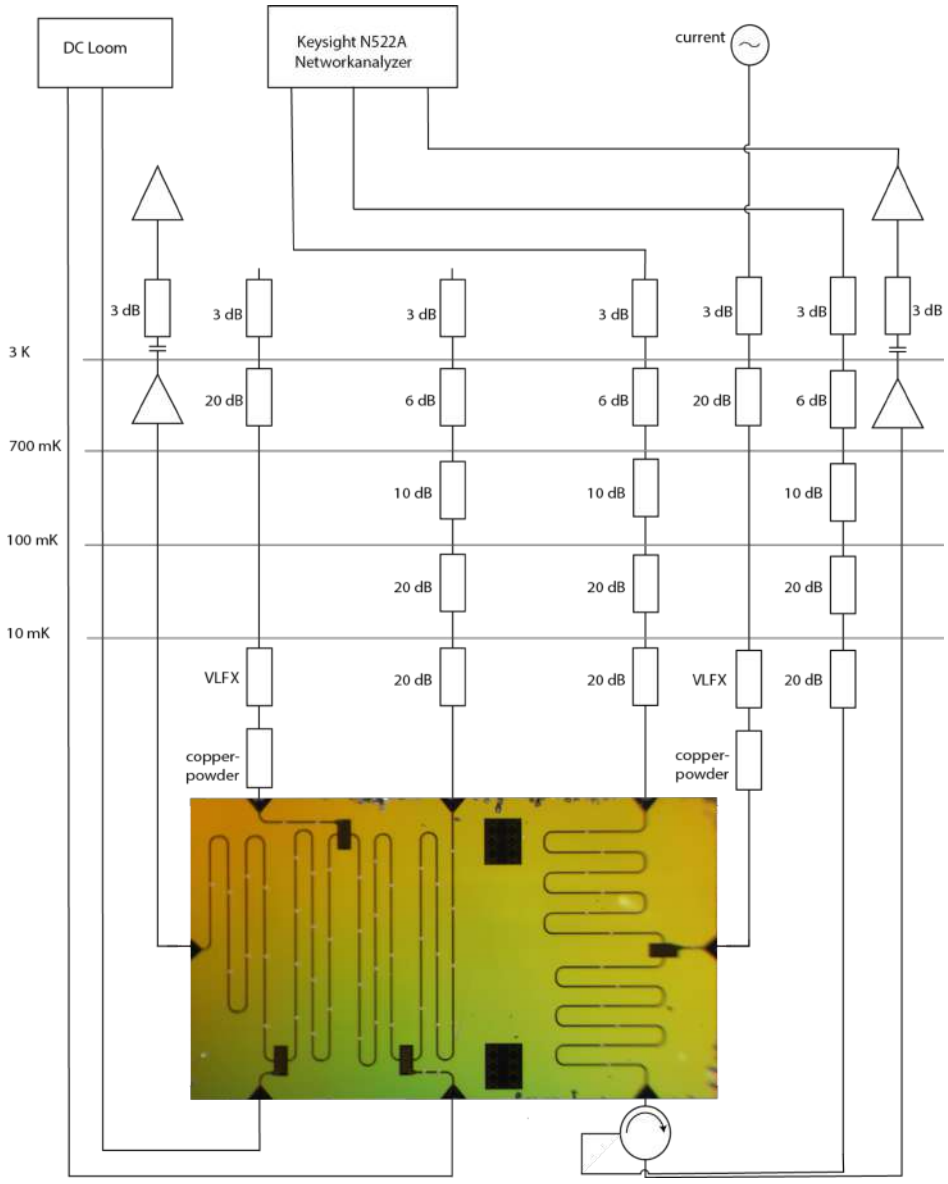

FIGURE 4.15: Wiring diagram of our setup. The input lines have $\sim 60\,\mathrm{dBm}$ attenuation. The output signal is amplified by cryogenic (HEMT) amplifiers and room temperature amplifiers. Our flux lines have VLFX and copper powder low pass filters.

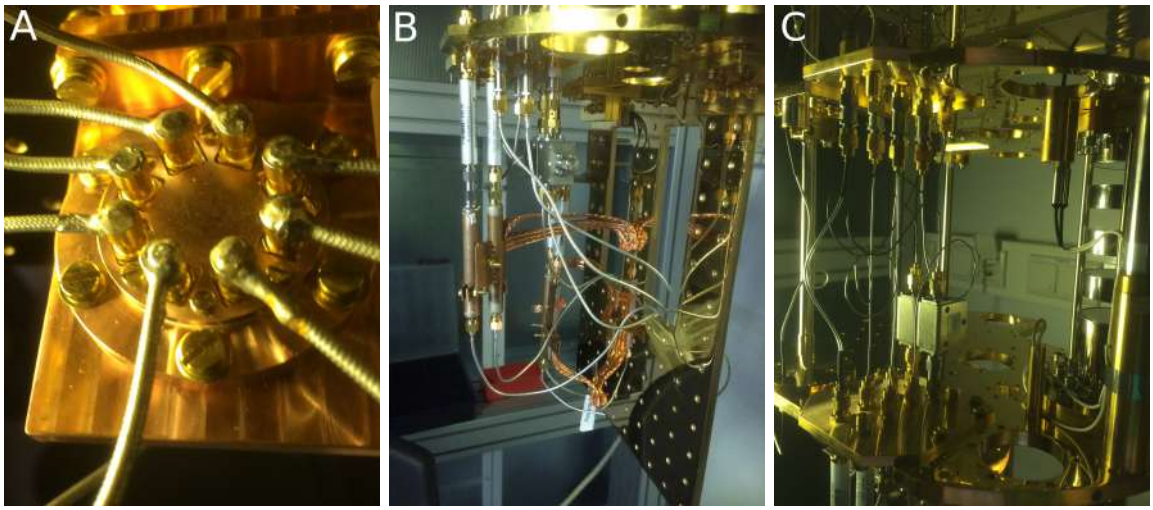

FIGURE 4.16: **A** The PCB (fig. 4.6 with the chip, mounted to the backside of the mixing chamber plate. **B** The wiring coming from the 10 mK stage going to the backside of mixing chamber plate. The grey tubes are the VLFX filters with the copper powder filters. **C** 3K stage with the cryogenic amplifiers.

The device is mounted to the backside of the mixing chamber plate, shown in fig. 4.16a and fig. 4.16b. Via the input lines the Vector Network Analyzer (VNA) sends signals to the device. These lines all have a total of ~ 60 dBm attenuation. The output goes through a circulator, which allows for measuring both in reflection and transmission, and then goes through a cryogenic amplifier (HEMT), shown in fig. 4.16c, and room temperature amplifier back to the VNA. For the flux lines we use a current source and the DC loom normally used for biasing magnets. The lines have a total attenuation of ~ 23 dBm and use VLFX and copper-powder filters as low-pass filters. The network analyzer and current sources are controlled by a computer using python wrapper scripts. With this we can set the input power, the current bias and the IF bandwidth.

Chapter 5

Josephson crystal: Experimental results and analysis

We started our experiments first measuring the most simple case of a Josephson crystal, a CPW interrupted with one coupler, as a benchmark for experiments with more junctions. However, it turned out that even the most simple case behaved differently from what we expected. In this chapter we first show in what sense the results diverged from our expectations. Then we compare the results with our linear circuit model in `QUCS` and a numerical integration of the equations of motion which takes into account the non-linearity up to the first order.

5.1 Experimental results

5.1.1 Full spectra at low powers

As a first experiment we measure the transmission coefficients for three different powers, shown in fig. 5.1.

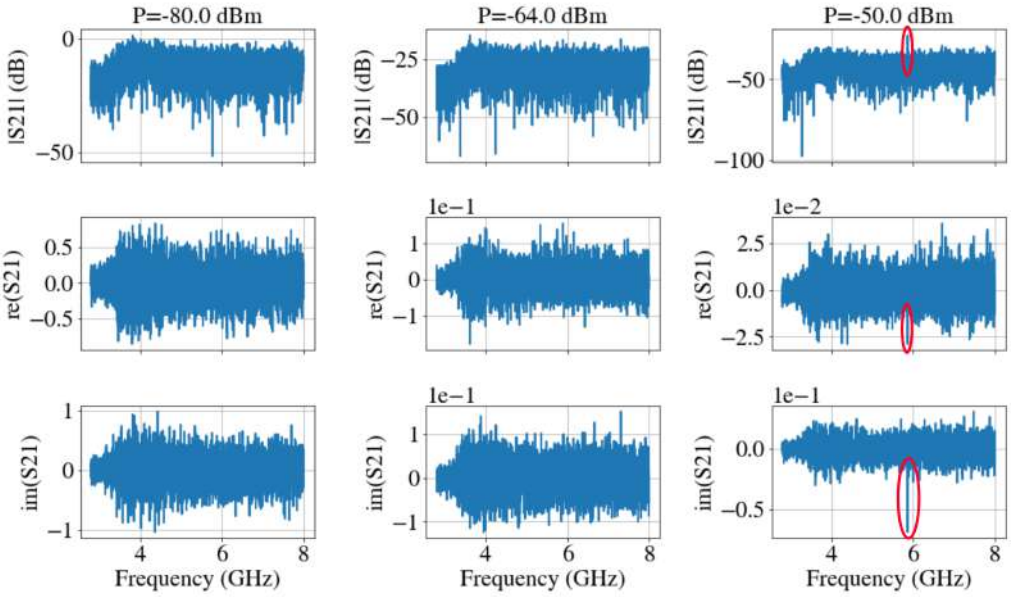

FIGURE 5.1: Full spectrum scan of the transmission coefficients of the 1 junction device for different input powers. In the upper row the absolute value is shown, in the rows below we plot the real and imaginary part separately. At $P = -50\,\mathrm{dBm}$ we see a peak appearing at $f = 5.8\,\mathrm{GHz}$, marked with red circles.

We are looking for the two normal modes, one which is dark and the other which is bright to the junction. The dark mode is independent of the flux through the junctions and should have a frequency around $f = 6\,\mathrm{GHz}$. The other mode instead does depend on the amount of flux through the junction and is expected to lie between $f = 5\,\mathrm{GHz}$ and $7\,\mathrm{GHz}$. We see only one peak appearing from $P = -50\,\mathrm{dBm}$ at $f = 5.8\,\mathrm{GHz}$, most clearly in the imaginary part. In section 5.1.2 we take a closer look at this peak.

Next, we examine the reflection coefficients for the same powers. They are shown in fig. 5.2. Here we see a dip at $f = 6.3\,\mathrm{GHz}$ at all powers. We will discuss this peak further in section 5.1.3. The peak we saw in the S_{12} parameters is not directly visible here. However, as we will see in the next section where we zoom in on a smaller frequency range, it is still present there.

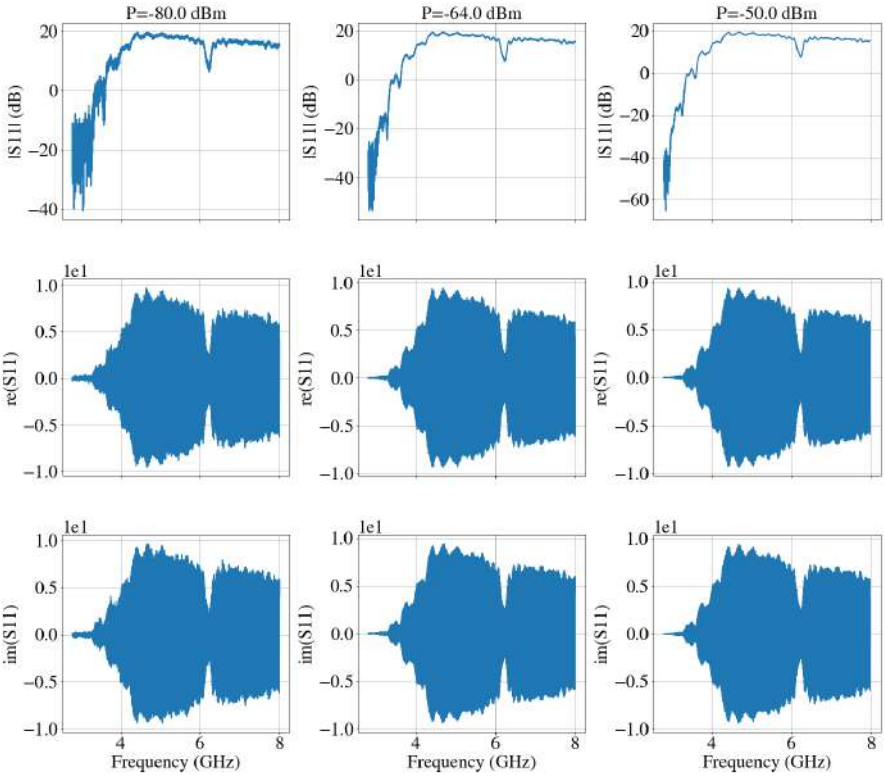

FIGURE 5.2: Full spectrum scan of the reflection coefficients of the 1 junction device for different input powers. Again, in the upper row the absolute value is shown, in the rows below we plot the real and imaginary part. Now a broad dip emerges around $f = 6.2\,\mathrm{GHz}$.

5.1.2 Bare resonator mode

In fig. 5.3 we zoom in on the reflection parameters of the peak at $f = 5.865\,\mathrm{GHz}$. At powers above $P = -15\,\mathrm{dBm}$ the peak at $f = 5.865\,\mathrm{GHz}$ vanishes and new peaks arise at $f = 5.866\,\mathrm{GHz}$ and the background moves upward. At the right a zoom is shown of the peaks below $P = -15\,\mathrm{dBm}$. The peak becomes narrower and deeper with decreasing power.

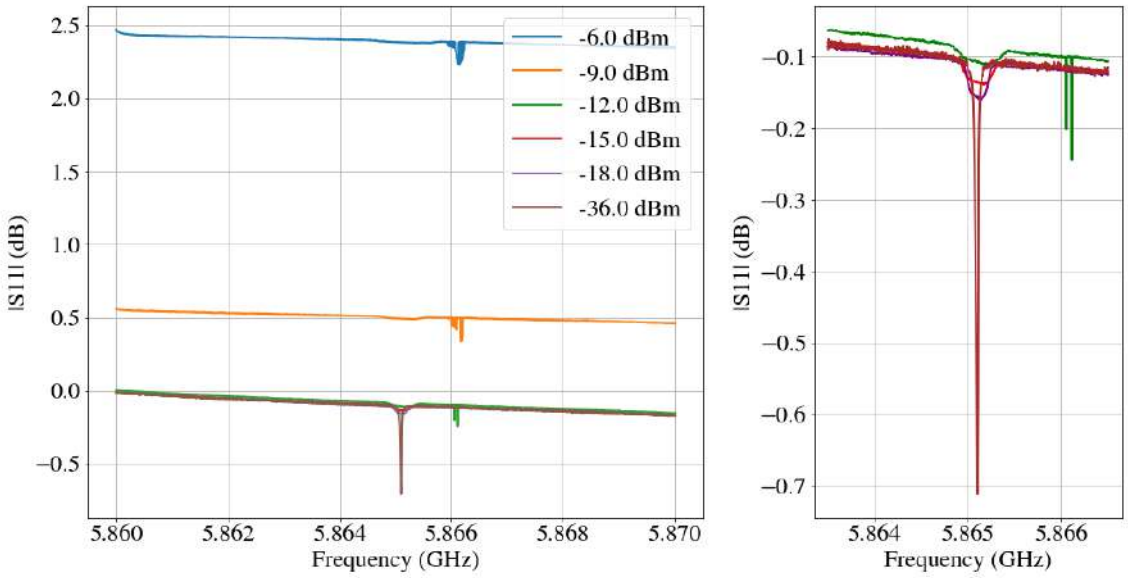

FIGURE 5.3: Reflection coefficients at $f = 5.865\,\text{GHz}$ for different input powers. We see a transition around $P = -15\,\text{dBm}$. Above this power the peak vanishes, and new peak arise at $f = 5.866\,\text{GHz}$.

We analyze this peak further at $P = -40\,\text{dBm}$. The behaviour as a function of the current bias is shown in fig. 5.4. The amplitude and phase do not move with current, which suggests it is the bare resonator mode with a current node at the junction. A slice of the peak is shown in fig. 5.5.

We fit eq. (2.39) and find an internal quality factor $Q_{\text{int}} = 2.7 \times 10^5$ and an external quality factor $Q_{\text{e}} = 3.1 \times 10^6$. Our external coupling differs a factor 10 from what we designed for, making our system undercoupled by a factor 10, while we designed for critical coupling.

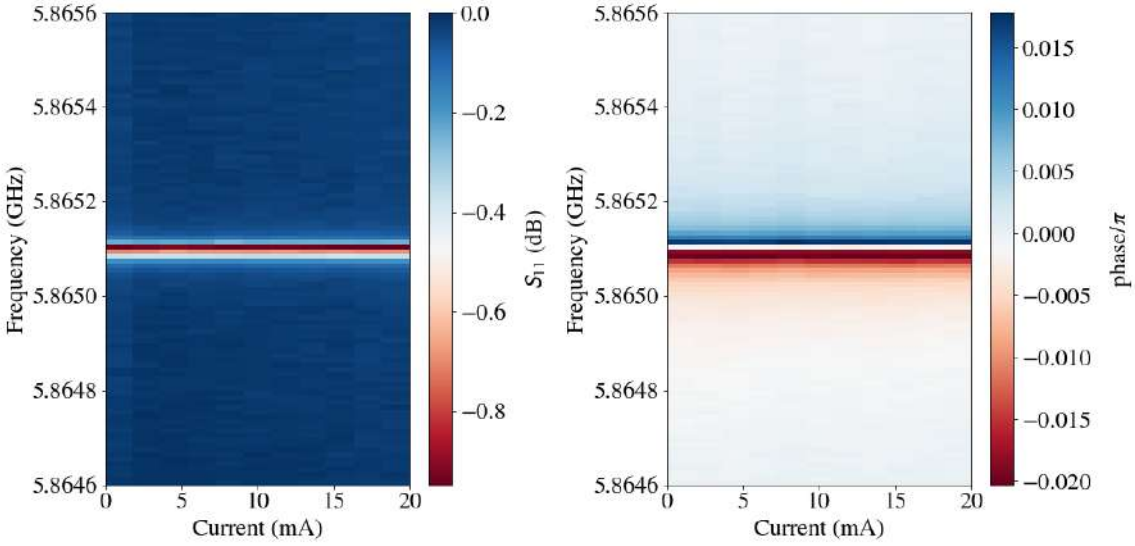

FIGURE 5.4: A current sweep at input power $P = -40\,\text{dBm}$ shows a peak at $f = 5.8651\,\text{GHz}$ independent of current. This suggests this is the bare CPW resonance which does not couple to the junctions.

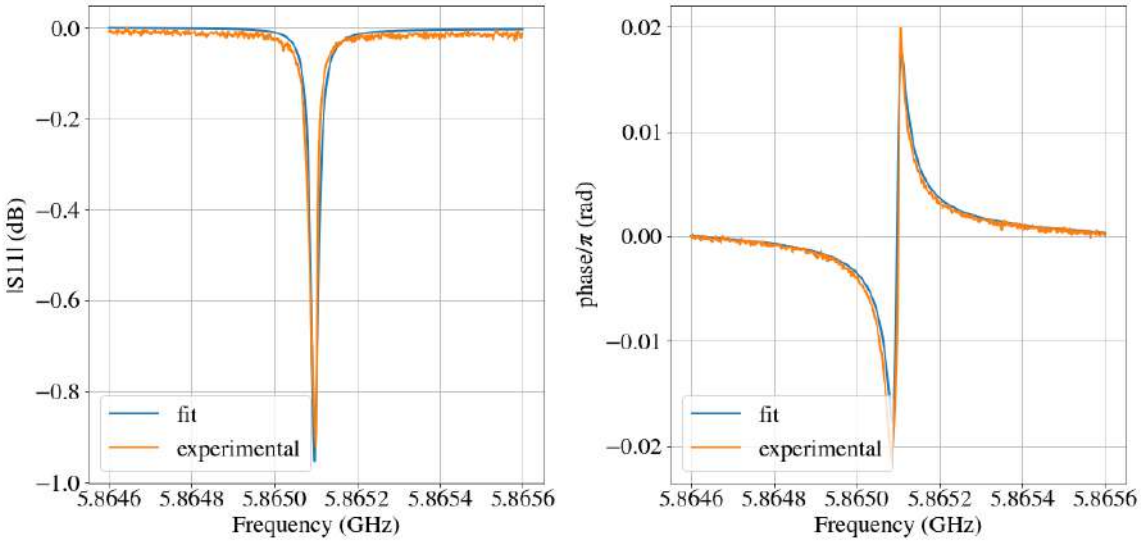

FIGURE 5.5: Linecut of the bare resonance at $P = -40\,\mathrm{dBm}$ including a lorentzian fit. The phase of the peak only changes a little, indicating that we are fairly undercoupled.

The cause can be either a mistake in our mapping $Q_{\mathrm{ext}} \to C_{\mathrm{c}}$ or $C_{\mathrm{c}} \to$ gap, or both (see fig. 4.11a and fig. 4.11b). We investigate them separately.

For the mapping $Q_{\mathrm{ext}} \to C_{\mathrm{c}}$ we used a `qucs` model and used the same relation for both the five junction device as the one junction device. We plot them in fig. 5.6, now calculating the relationship for the one junction device separately.

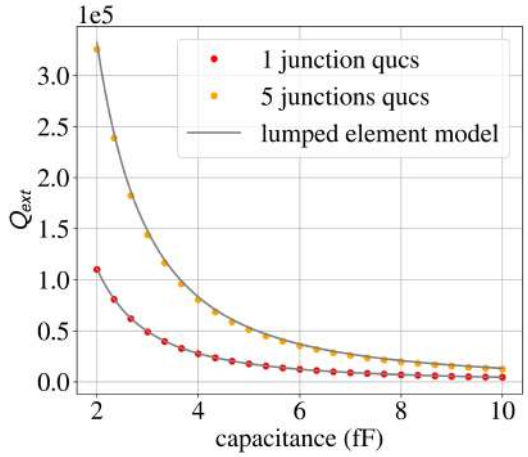

FIGURE 5.6: We calculate the relation between Q_{ext} and the coupling capacitance C_{c} for the one junction device, and compare it with the curve we actually used, assuming five junctions (see fig. 4.11a). Since this predicts a lower Q_{ext} than we assumed it cannot explain why our experiments yields a higher Q_{ext}. We also have plotted the analytical expression from a lumped element approximation, which confirms our methods are correct.

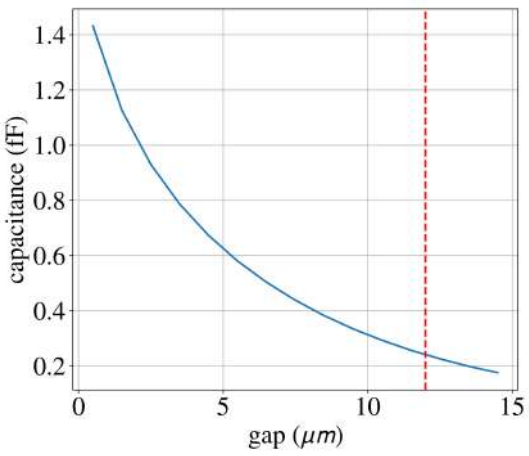

FIGURE 5.7: Relation between coupling capacitance and gap in the inner conductor of our CPW, now obtained with `sonnet` build-in equations, instead of using ideal components. The red line denotes the gap used in our devices. Now we get a capacitance 10 times lower than the 4 fF we found with fig. 4.11b.

To check we did not make a mistake in our `qucs` model we also plot the relation from our lumped element model section 2.1.3. First of all, we see that our `qucs` model and our lumped element model agree really well, confirming our method itself is correct. Second, we observe that the one junction device has *lower* external coupling than our five junction device. From this, we conclude that our under coupling cannot be explained by a mistake in the mapping $Q_{\text{ext}} \rightarrow C_{\text{c}}$, and that we must have much lower capacitances than needed. From eq. (2.33) we derive:

$$C_c = \frac{1}{2Q_e\omega_0 Z_0}\left(1 + \sqrt{2Q_e\omega_0 Z_0 C + 1}\right) = 0.4\,\text{fF} \tag{5.1}$$

So indeed, our capacitances are much smaller than we thought.

The next question we want to answer is why our capacitances are so much smaller. Possibly our `sonnet` simulation where we added an ideal inductor in series with our capacitance to create and LC circuit, allowing us to find the capacitance from the resonance frequency, is wrong. We compare this with a different approach, where we do not make use of extra ideal components, but derive the capacitance from the Y parameters using the build-in equations of `sonnet`. Here, our system is modelled as shown in fig. 5.8.

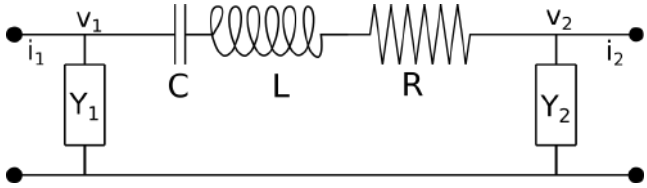

FIGURE 5.8: PI-model of a CPW interrupted with a gap. The inductor represents the parasitic inductance. Using the Y-parameters from the `sonnet` simulation we can find the capacitances and parasitic inductance of the capacitor.

The current voltage relations can be written in a matrix form $I = YV$:

$$\begin{bmatrix} i_1 \\ i_2 \end{bmatrix} = \begin{bmatrix} Y_1 + Y_{RLC} & -Y_{RLC} \\ Y_{RLC} & -Y_2 - Y_{RLC} \end{bmatrix} \begin{bmatrix} v_1 \\ v_2 \end{bmatrix} \tag{5.2}$$

Here $Y_{\text{RLC}} = \frac{j\omega C}{1-\omega^2 LC + j\omega RC}$. Now it follows that:

$$\frac{1}{\omega\,\text{Im}(1/Y_{12})} = \frac{C}{1-\omega^2 LC} \tag{5.3}$$

So by plotting $\frac{1}{\omega\,\text{Im}(1/Y_{12})}$ as a function of ω we find the capacitance from the crossing with the y-axis and the parasitic inductance from the resonance. In fig. 5.7 we show the new C_c- gap relation. Indeed, now we find that a gap of 12 µm yields a capacitance of 0.25 fF which is much more closer to the real value than the 4 fF we found before.

Next, now we have derived some useful information from the internal and external couplings, we focus on the resonance frequency $f = 5.8651\,\text{GHz}$ which is 135 MHz lower than the $f = 6.02\,\text{GHz}$ we designed for. This is mostly due to the kinetic inductance its sensibility to the film thickness, and to a lesser extent due to the coupling capacitances. We already have our coupling capacitances and the capacitance per unit length of the resonator is completely determined by the geometry and therefore not expected to change much. Using $f_0 = \sqrt{\frac{1}{L(C+2C_c)}}$ we can calculate the inductance per unit length l and the impedance Z_0. The final fit parameters are summarized in table 5.1.

TABLE 5.1: Comparison of CPW parameters between the values we designed for and the values of our actual realization.

Parameter	Realized	Designed
f (GHz)	5.865	6.022
l ($\mu\mathrm{H\,m^{-1}}$)	0.485	0.461
c ($\mathrm{nF\,m^{-1}}$)	0.184	0.184
v ($10^8\,\mathrm{m\,s^{-1}}$)	1.06	1.08
Z_0 (Ω)	51	50
C_c (fF)	0.42	4.0
α (dB)	0.0052	0.015
Q_{int}	3×10^6	1×10^5
Q_{ext}	3×10^5	2×10^5

We use these fit parameters for our `QUCS` model and plot the result together with our measurements in fig. 5.9. We see that our agrees really well with our experimental data confirming this is indeed the bare resonator mode and that the fit parameters we found are correct.

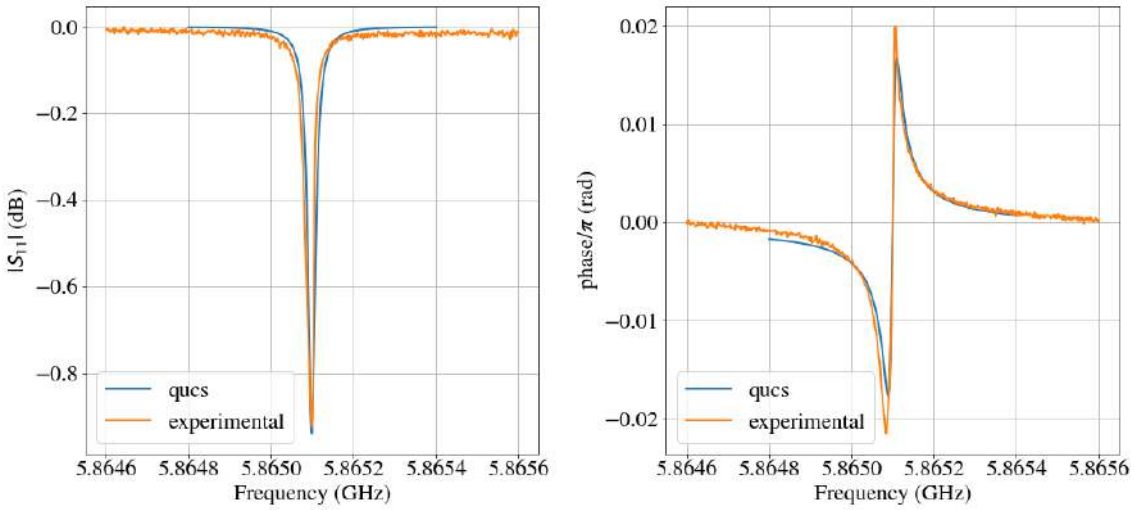

FIGURE 5.9: Resonance peak with at $f = 5.8651\,\mathrm{GHz}$ and $P_{\mathrm{input}} = -40\,\mathrm{dBm}$ together with a fit of our `QUCS` confirming that our fit parameters describe our system very well.

5.1.3 Broad peak

In fig. 5.10 we show three different power scans for the broad peak we observed in the reflection parameters around 6.2 GHz, for both low and high powers.

We see that the peak exists from very low powers up to powers of $P = 10\,\mathrm{dBm}$, from then it vanishes. Around $P = -15\,\mathrm{dBm}$ it gets deeper and narrower, and shifts to the right. At $P = 0\,\mathrm{dBm}$ it jumps back to the left.

In fig. 5.11 we show the current dependence of this peak for low power ($P = -40\,\mathrm{dBm}$) and high power ($P = 8\,\mathrm{dBm}$). At low power the peak does not move with current and is thus independent of the flux through the junctions. At high power it moves slightly with current, which is easiest to notice between 0 mA and −20 mA.

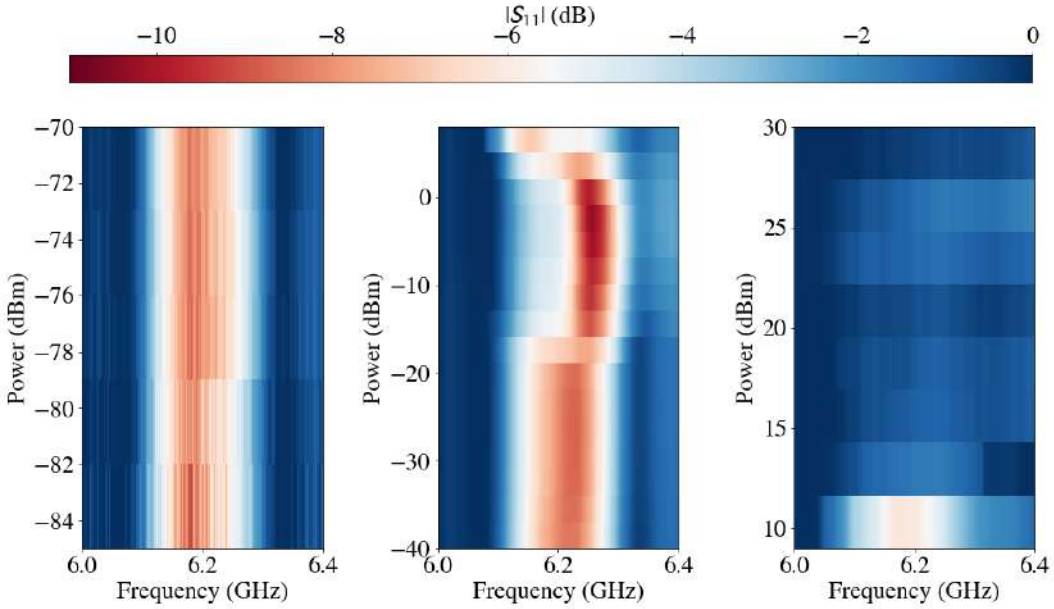

FIGURE 5.10: Around $f = 6.2\,\text{GHz}$ a broad assymetric peak is observed. The peak gets deformed from $P_{input} = -15\,\text{dBm}$ and higher.

We do not believe this 'mode' is the junction for several reasons. First of all the peak has a width of $\sim 200\,\text{MHz}$ which we cannot reproduce in our `QUCS` simulation for any gap resistance R_j, see also section 5.2.1. Second, the peak hardly moves with current. We expect the peak to move between 5 GHz and 7 GHz within $0.5\phi_0$. From other experiments with approximately the same size SQUID, we know that $0.5\phi_0 \sim 3\,\text{mA}$. Therefore we would expect the peak to move much more over 40 mA.

One explanation could be that this mode is a parasitic slotline mode caused by the ground plane being split. These modes are known to exhibit resonance effects and signal loss and also can explain why we see it only in the reflection parameters [48] [49].

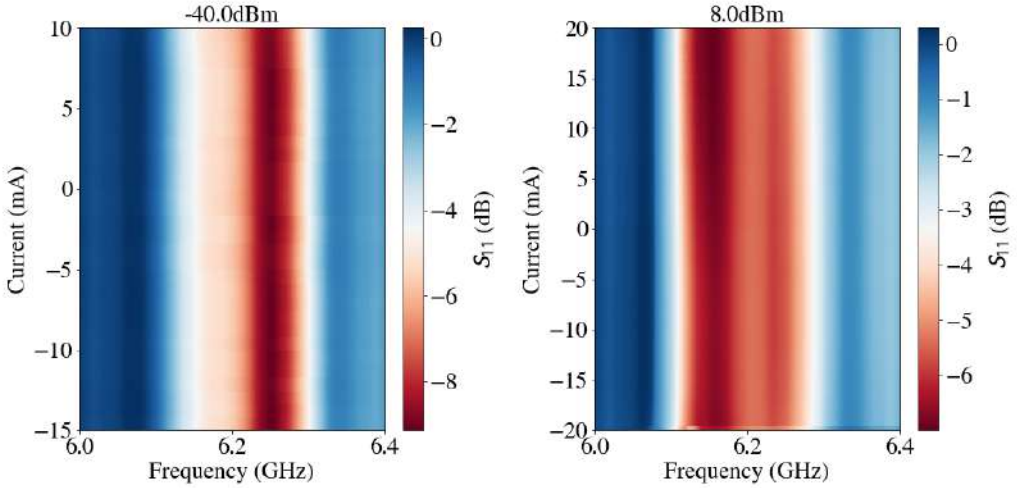

FIGURE 5.11: Broad peak around $f = 6.2\,\text{GHz}$ at $P_{input} = 8\,\text{dBm}$. Here the peak sligthly changes with current

5.2 Why do we see no tuning?

In this section we explore different explanations why we did not see the moving peak. As a first explanation we test the effect of sub-gap resistance of the junctions on the peak visibility. Next we explore the effect of flux dephasing. Finally we make a classical model of our device, taking the non-linearity of the junctions into account and look how this influences the moving peak.

5.2.1 Josephson sub-gap resistance

Using the values we found from the bare peak, we use our `QUCS` model to look what happens to the moving peak. We find that the visibility of the moving peak depends on the Josephson sub-gap resistance as shown in fig. 5.12.

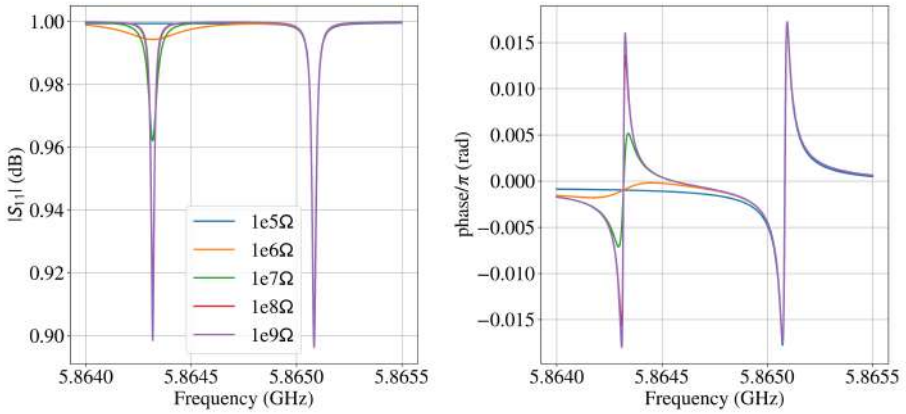

FIGURE 5.12: `QUCS` simulation of the magnitude and phase of the two resonances for different Josephson gap resistances using the fit parameters derived in the previous section. The left peak is the peak moving with flux, the right is the bare peak dark to the junctions. The depth and therefore the visibility of the left peak depends on the josephson gap resistance.

In fig. 5.13 we show the dependence of the peak depth and maximum phase shift as a function of the sub-gap resistance, together with our noise floor $N \sim 0.01\,\mathrm{dB}$.

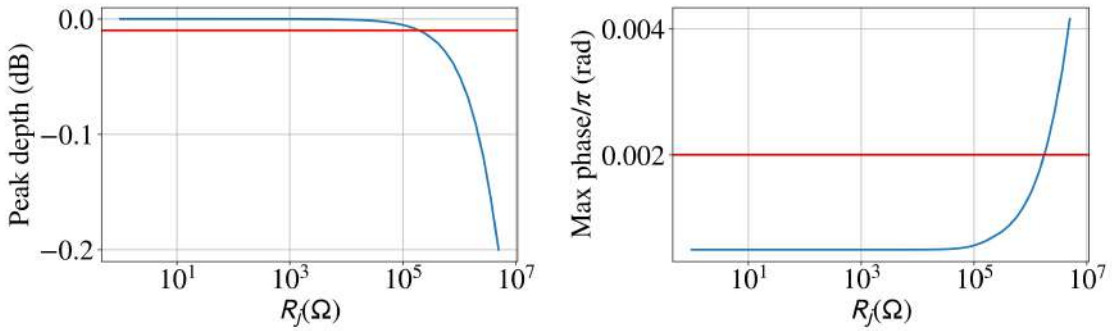

FIGURE 5.13: Here we plot the depth of the moving peak and the maximum phase for different Josephson gap resistances R_j. The red line denotes the noise in our measurments. We see that at resistances below $R_j = 1 \times 10^5\,\Omega$ the peak becomes invisible, both in phase and magnitude.

From this we derive that the sub-gap resistance must lie below $R_{\mathrm{j,max}} \approx 0.2\,\mathrm{M\Omega}$ for the peak to become invisible. The sub-gap resistance generally depends on the density of quasi particles generated either by thermal excitation or finite voltage bias [50] and is expected to be much smaller than the normal state resistance [51]. Using t_1 from experiments done with the same type of junctions but in a fridge shielded against infra-red radiation, we find a minimal sub-gap resistance of [52]:

$$R_j = \frac{Q}{2\pi f_0 C} = \frac{t_1}{2C} = 90\,\mathrm{M\Omega} \tag{5.4}$$

This is in the same order of magnitude as other experiments with Al/AlO junctions [53]. Measurements with phase qubits have shown a reduction in t_1 from 450 ns to 120 ns by removing infra-red shielding [54] while a sub-gap resistance of $R_j = 0.2\,\mathrm{M\Omega}$ implies a t_1 around 20 ns. Therefore it is unlikely that the sub-gap resistance of the junction is below $0.2\,\mathrm{M\Omega}$, even when the infrared radiation is taken into account.

5.2.2 Flux noise

A second cause of the peak to disappear could be dephasing due to flux noise. The flux noise in the fridge will change the plasma frequency f_p by an amount $\Delta f_p = \frac{df_p}{d\phi}\Delta\Phi$, with $\Delta\Phi$ a stochastic variable characterizing the flux noise. This is shown in fig. 5.14.

Now by eq. (4.1) the peak itself will shift by $\Delta f = \frac{df}{df_p}\Delta f_p$. When the integration time of the VNA is much longer than the time over which the noise varies, the resulting signal is an average of all quadratures shifted by Δf, decreasing the depth of the peak. Mathematically:

$$Q_{avg} = \int_{-\infty}^{\infty} Q(f - f_0)P(f)df \tag{5.5}$$

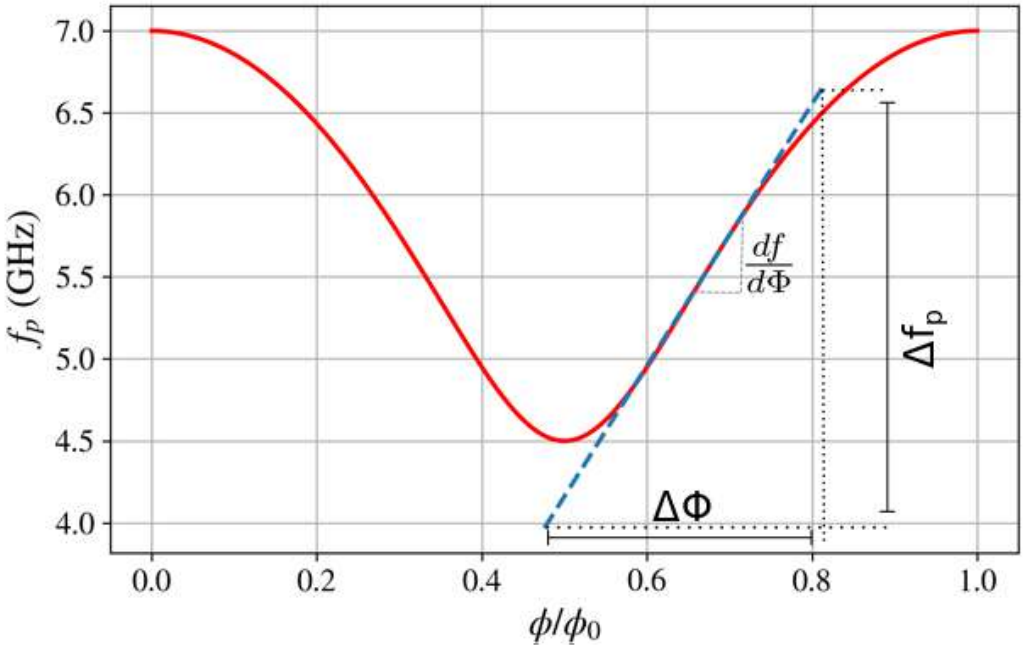

FIGURE 5.14: The flux noise picked up in the SQUID causes the plasma frequency f_p to fluctuate depending on the slope of f-ϕ relation at that point.

Here Q is either the real or imaginary part of our signal, and P a Gaussian distribution characterizing resonance frequency distribution centered around a chosen resonance frequency with $\sigma_{\Delta f} = \frac{df}{df_p}\frac{df_p}{d\phi}\sigma_{\Delta\Phi}$. To test whether flux noise indeed can explain the disappearance of our peak, we need to know the minimal $\sigma_{\Delta\Phi}$ which will bring our peak below the noise floor. To this end, we first generate an unshifted signal with our `QUCS` model at $f = 5.74\,\text{GHz}$ using the fit parameters derived above. We chose this frequency because $\frac{df}{d\phi} = 8\,\text{GHz}/\phi_0$ is maximum here, such that we will arrive at a lower limit. We use a gap resistance of $R_j = 1 \times 10^8\,\Omega$ to make sure the disappearance is only due to dephasing. Next, we numerically evaluate eq. (5.5) for different $\sigma_{\Delta f}$ and look for what value our peak becomes below our noise of $N \sim 0.01\,\text{dB}$. Now, as we can derive $\frac{df}{df_p}$ from eq. (4.1) we will have an estimation of the minimal $\sigma_{\Delta\Phi}$ needed to let our peak disappear, and thus an under limit of the flux noise.

In fig. 5.15 we plot the numerical evaluation of eq. (5.5) for different $\sigma_{\Delta f}$.

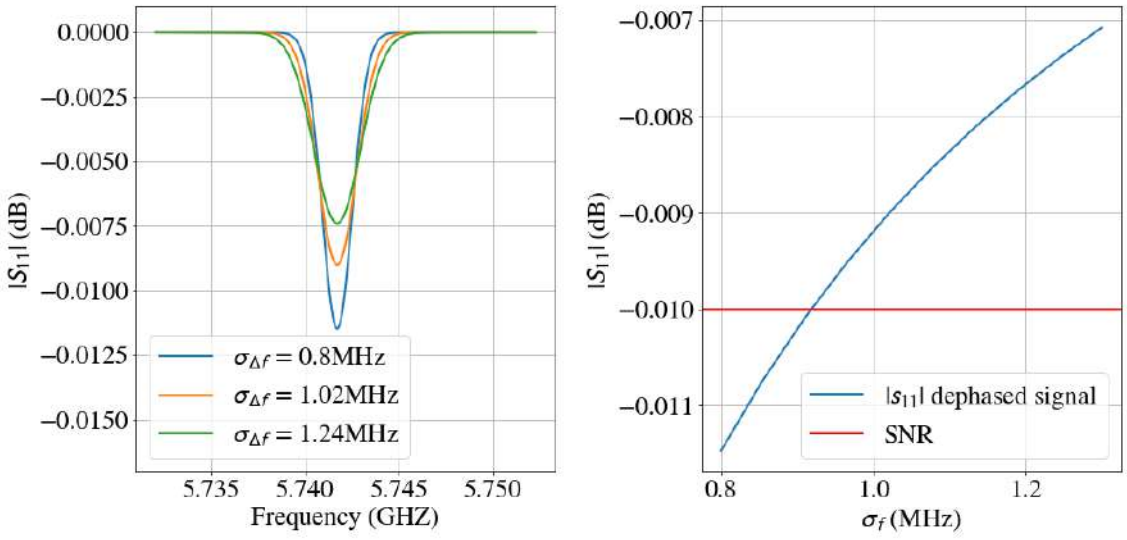

FIGURE 5.15: Convolution of tunable peak at $f = 5.810\,\text{GHz}$ made in `QUCS` with a gaussian distribution, modelling the effect of flux noise for different $\sigma_{\Delta f}$. In the right plot the depth versus the spread is plotted together with our signal to noise ratio. Above $\sigma_{\Delta f} = 0.9\,\text{MHz}$ the peak becomes invisible

We find that above $\sigma_{\Delta f} = 0.9\,\text{MHz}$ and the peak becomes below our signal to noise ratio. Now we need to know $\frac{df}{df_p}$ at $f = 5.74\,\text{GHz}$. As this is close to $\bar{f}$ we can find an analytical expression by expanding eq. (4.1) at $\bar{f}$:

$$f^2\left(\frac{cv}{2C_j}\frac{\Delta}{v} + 1\right) = f_p^2 + \frac{cv}{8\pi C_j} \tag{5.6}$$

By implicit differentiation we arrive at:

$$\left.\frac{df}{df_p}\right|_{\bar{f}} = \frac{2C_j}{2C_j + c\Delta} = 0.13 \tag{5.7}$$

So, we find that for our under limit:

$$\sigma_{\Delta\Phi} = \frac{0.9 * 10^{-3}}{0.13 * 8} = 10^{-3}\phi_0 \tag{5.8}$$

From other experiments done with qubits in the same fridge we can estimate the magnetic field strength. We plot the frequency-flux scan in fig. 5.16 and fit the theoretical relation eq. (2.46) with $\alpha = 0$.

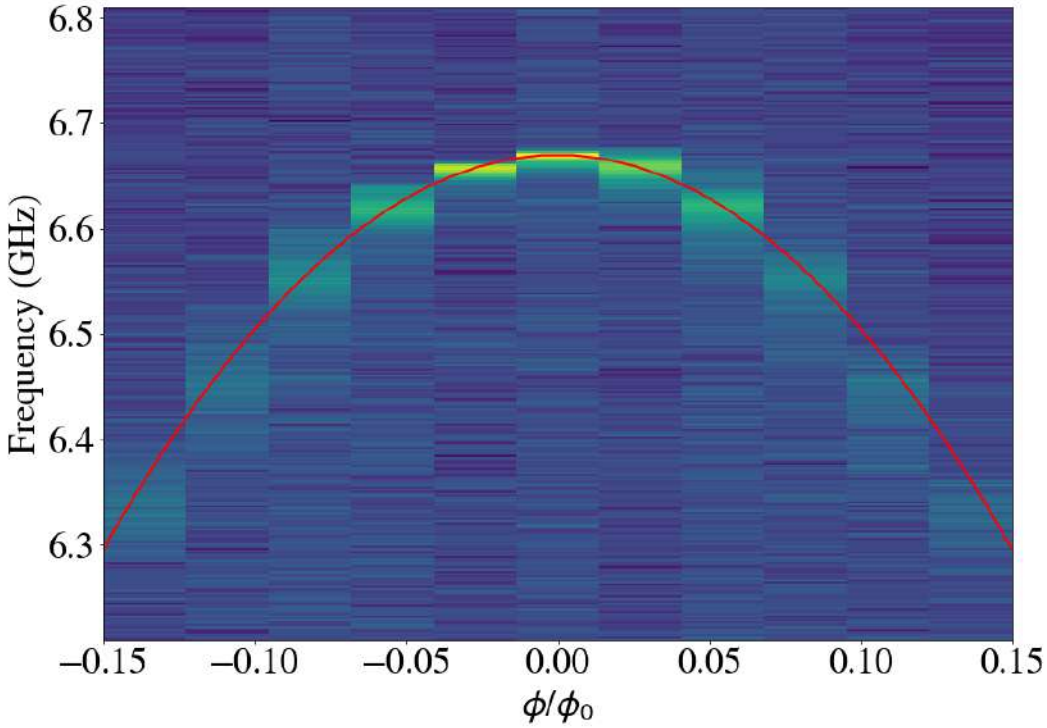

FIGURE 5.16: Frequency versus flux dependence of a qubit measured in the same fridge as our device. The red line shows a fit of the theoretical frequency versus flux curve. We see a maximum flux noise $\sim 50\,\mathrm{MHz}$.

In the experiment the frequency was measured as a function of current. We translated this to flux by comparison with an earlier experiment where the frequency of the same qubit was measured against flux [52]. At $\phi/\phi_0 = -0.07$ we have $\Delta f \sim 50\,\mathrm{MHz}$ which translates to $\Delta\phi \approx 0.03\phi_0$. As our SQUID has nearly the same area as in the qubit experiment, we will have the same flux noise in our experiment. Since it is ~ 30 higher than the under limit we conclude that it will indeed make our peak invisible.

To verify if our calculations make sense we calculate the magnetic field strength from the area of the SQUID and get $B \approx 30\,\mathrm{nT}$. B-field measurements in the room report a maximum field strength of $117\,\mathrm{nT}$ [55], which supports our estimation given that we have no magnetic shielding inside the fridge.

5.2.3 Non-linearity

Finally we develop a non-linear model to explore the effect of the non-linearity on the visibility of the peak. We approximate the transmission lines again by a lumped element circuit and write down the equations of motion at the degeneracy point $\bar{f}$. In fig. 5.17 the equivalent circuit together with the fluxes is shown.

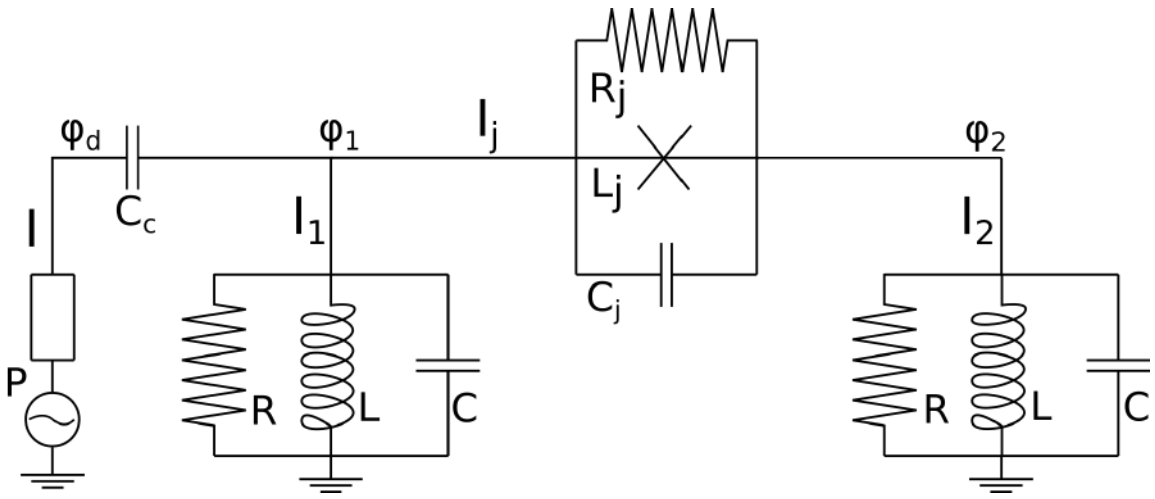

FIGURE 5.17: Lumped element model of the 1 junction device. The system is described by two fluxes, ϕ_1 and ϕ_2. By modelling the junction as a nonlinear inductor we can explore the effect of the nonlinearity on our results.

From Kirchhoff's laws we have $I_j = I_2$ and $I = I_1 + I_j = I_1 + I_2$. This gives us two equations of motion:

$$C(\ddot{\phi}_1 + \ddot{\phi}_2) + \frac{1}{R}(\dot{\phi}_1 + \dot{\phi}_2) + \frac{1}{L}(\phi_1 + \phi_2) = C_c(\ddot{\phi}_d - \ddot{\phi}_1) \tag{5.9}$$

$$C_j(\ddot{\phi}_1 - \ddot{\phi}_2) + \frac{1}{R_j}(\dot{\phi}_1 - \dot{\phi}_2) + I_0 \sin((\phi_1 - \phi_2)/\phi_0) = C\ddot{\phi}_2 + \frac{1}{R}\dot{\phi}_2 + \frac{1}{L}\phi_2 \tag{5.10}$$

Now we introduce $\phi_+ = \phi_1 + \phi_2$ and $\phi_- = \phi_1 - \phi_2$. Using $C_c << C$ we get two uncoupled equations:

$$C\ddot{\phi}_+ + \frac{1}{R}\dot{\phi}_+ \frac{1}{L}\phi_+ = C_c\ddot{\phi}_d \tag{5.11}$$

$$(2C_j + C)\ddot{\phi}_- + (\frac{2}{R_j} + \frac{1}{R})\dot{\phi}_- + \frac{1}{L}\phi_- + 2I_0 \sin(\phi_-/\phi_0) = C_c\ddot{\phi}_d \tag{5.12}$$

The first equation does not involve the junction and corresponds to the dark mode. We now focus on the other mode. We expand the sine up to third order and use that we are tuned at the degeneracy point, such that $\frac{1}{LC} = \frac{I_0}{\phi_0 L_j} = \omega^2$:

$$(2C_j + C)\ddot{\phi}_- + (\frac{2}{R_j} + \frac{1}{R})\dot{\phi}_- + \frac{1}{L}\phi_- + 2I_0\left(\phi_-/\phi_0 - \frac{1}{6}(\phi_-/\phi_0)^3\right) = C_c\ddot{\phi}_d \tag{5.13}$$

$$(2C_j + C)\ddot{\phi}_- + (\frac{2}{R_j} + \frac{1}{R})\dot{\phi}_- + C\omega^2\phi_- + 2C_j\omega^2\phi_- - \frac{1}{3}C_j\omega^2\left(\frac{\phi_-}{\phi_0)}\right)^2\phi_- = C_c\ddot{\phi}_d \tag{5.14}$$

We introduce $\tilde{C} = 2C_j + C$,$\frac{1}{\tilde{R}} = \frac{2}{R_j} + \frac{1}{R}$, $\tilde{Q} = \tilde{R}\tilde{C}\omega_0$ and assume a drive $\phi_d = \Phi\cos(\omega_d t)$ which gives our Duffing equation:

$$\ddot{\phi}_- + \frac{1}{\tilde{R}\tilde{C}}\dot{\phi}_- + \omega^2\phi_- - \frac{1}{3}\frac{C_j\omega^2}{\tilde{C}}\left(\frac{\phi_-}{\phi_0}\right)^2\phi_- = -\frac{C_c}{\tilde{C}}\omega_d^2\Phi\cos(\omega_d t) \tag{5.15}$$

We want to solve this system by numerical integration, and then look at the steady-state solutions. However, for high Q, the time it takes to arrive at equilibrium is $t_{\text{eq}} = \frac{2}{\kappa} = \frac{Q}{\pi f_0}$ which is a few microseconds while the oscillations themselves are at $\frac{1}{f_0}$ which is below a nanosecond. To reduce the number of time steps needed to arrive at equilibrium, we average these out using the Krylov–Bogoliubov method [56] [57]. This works as follows. We first assume a solution in the form of $\phi_- = x(\tau)e^{i\omega_d t} + x(\tau)^* e^{-i\omega_d t}$ which is basically a truncated Fourier expansion with $x(\tau)$ a slow moving variable with $\tau = |\omega - \omega_d|t = \delta t$. Then, when taking derivatives, we drop the term with the highest order in δ:

$$\dot{\phi}_- = i\omega_d[xe^{i\omega_d t} - x^* e^{-i\omega_d t}] + [\frac{dx}{d\tau}e^{i\omega_d t} + \frac{dx^*}{d\tau}e^{-i\omega_d t}]\delta \approx i\omega_d[xe^{i\omega_d t} - x^* e^{-i\omega_d t}] \tag{5.16}$$

$$\ddot{\phi}_- = -\omega_d^2[xe^{i\omega_d t} + x^* e^{-i\omega_d t}] + i\omega_d[\frac{dx}{d\tau}e^{i\omega_d t} - \frac{dx^*}{d\tau}e^{-i\omega_d t}]\delta \tag{5.17}$$

$$+ i\omega_d[\frac{dx}{d\tau}e^{i\omega_d t} - \frac{dx^*}{d\tau}e^{-i\omega_d t}]\delta + [\frac{d^2x}{d\tau^2}e^{i\omega_d t} + \frac{d^2x^*}{d\tau^2}e^{-i\omega_d t}]\delta^2 \approx \tag{5.18}$$

$$- \omega_d^2[xe^{i\omega_d t} + x^* e^{-i\omega_d t}] + 2i\omega_d[\frac{dx}{d\tau}e^{i\omega_d t} - \frac{dx^*}{d\tau}e^{-i\omega_d t}]\delta \tag{5.19}$$

We fill this in into our equation and drop the fast moving terms (i.e. the terms with $e^{i2\omega_d t}$ or higher). We fill this in into our equation and rescale x and get the following normalized equation for the slow moving variable $v = x\sqrt{\frac{C_j\omega^2}{2\tilde{C}\omega_d\delta\phi_0^2}}$:

$$\frac{dv}{d\tau} = -\frac{v}{\Omega} - iv\left(|v|^2 - sgn(\omega - \omega_d)\right) + i\sqrt{\beta} \tag{5.20}$$

With the following definitions:

Table 5.2: Parameter definitions of the normalized Duffing equation

Parameter	Definition
$\tilde{C}$	$2C_j + C$
$\frac{1}{\tilde{R}}$	$\frac{2}{R_j} + \frac{1}{R}$
$\tilde{Q}$	$\tilde{R}\tilde{C}\omega_0$
v	$x\sqrt{\frac{C_j\omega^2}{2\tilde{C}\omega_d\delta\phi_0^2}}$
β	$\frac{C_jC_c^2}{\tilde{C}^3}\frac{\Phi^2}{\phi_0^2}\frac{\omega^2\omega_d}{32\delta^3}$
Ω	$2\tilde{R}\tilde{C}\delta$

In fig. 5.18 we plot the steady state results of our model for different powers, obtained by Runge-Kutta integration of eq. (5.20) using the system parameters from table 5.1 and $R_j = 1 \times 10^7\,\Omega$. We intergrated over a total time $\tau_{total} = 4t_{\text{eq}}\delta = \frac{8}{\kappa}\delta = \frac{4Q}{\pi f_0}\delta$ with steps $h = 0.2$.

We change the driving frequency up and down (denoted by the arrows) and observe two branches as expected (see section 2.4.3). When we go up in frequency we see behaviour similar to a normal harmonic oscillator, which we call the lower branch. Sweeping the other

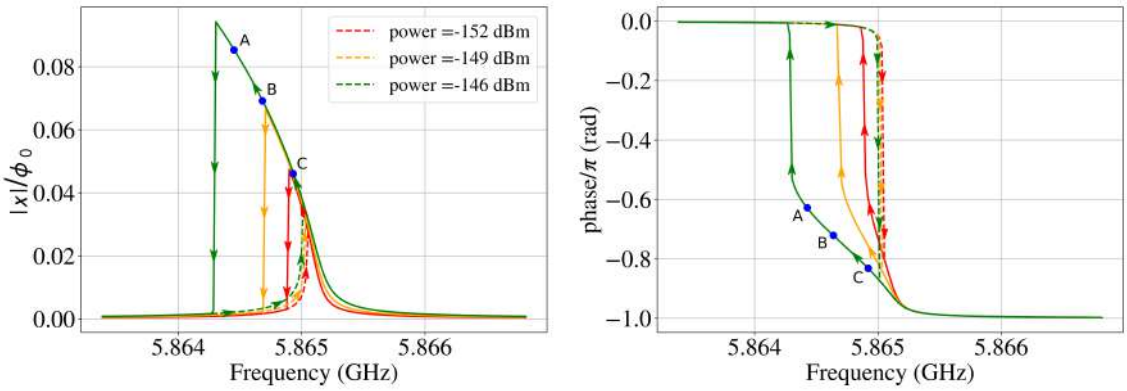

FIGURE 5.18: Steady-state flux across the junctions as a function of the driving frequency for different powers. For each power there are two branches. When the frequency is swept up, the branch with the lower amplitude is chosen (dashed), while when the frequency is swept down, the higher branch is chosen (solid). Time traces in the phase plane of the points A, B, and C are plotted in the next figure. We used $R_j = 2 \times 10^7\,\Omega$, such that $\tilde{Q} = 2 \times 10^5$.

way round, starting at high frequency an slowly lowering the frequency, the amplitude keeps being high after having passed the resonance frequency $\bar{f}$, up to a certain point where it drops back to the same value as the lower branch. The phase chooses another branch too. Far above the resonance it is in anti-phase with the drive (π delay), but when we cross the resonance frequency it slowly increase it phase, and then jumps to zero and becomes back in phase with the drive. We call this branch the upper branch, and the frequency where it switches back to the lower state the jump-down freqeuncy. Sometimes a peak appeared in the phase close to this frequency. This is because the model takes a long time to converge at this point and does not reach steady-state. We removed these points for plotting purposes, as explained in appendix C.

We plot time traces in the phase plane for the points marked by A, B and C in fig. 5.19.

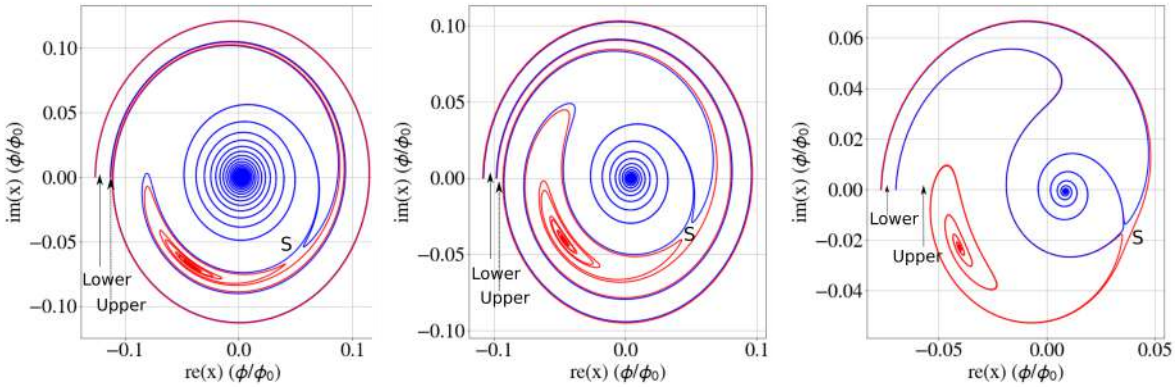

(A) (B) (C)

FIGURE 5.19: Time traces for four different initial conditions plotted in the phase plane, for the same parameters as in fig. 5.18, at $P = -146\,\text{dBm}$. The three subplots (A), (B) and (C) correspond to the points denoted in fig. 5.18. There are two steady-state solutions, corresponding to the upper and lower branch. There is also a unstable saddle point, denoted by S.

The blue spiral is the steady state solution for the lower branch, the red line the steady-state solution of the upper branch. The initial conditions leading to either of these two are marked with an arrow. We see that at small detuning (fig. 5.19a) most points lead to the upper branch. This is in agreement with the observation that decreasing the frequency will lead to the upper branch. The other way round, at higher detuning, there are very few points leading to the upper branch, and nearly all initial conditions will stabilize in the lower branch. We also have an unstable saddle point, denoted by S.

To explore the different regimes of the system we plot the difference between the steady-state amplitudes of the two branches for different driving frequencies and powers, which we use as a measure for the amount of bifurcation. This is plotted in fig. 5.20.

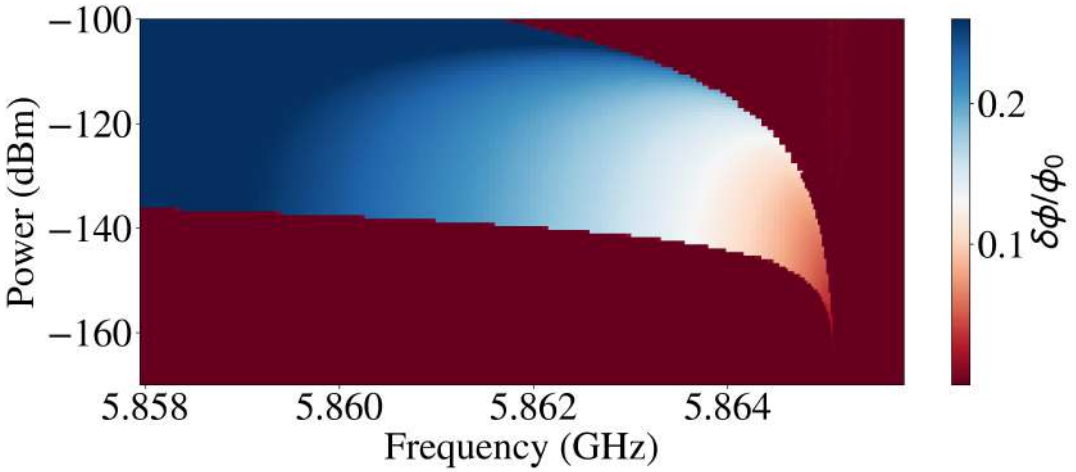

FIGURE 5.20: Phase diagram of the one junction device with $R_j = 2 \times 10^7\,\Omega$ and $\tilde{Q} = 2 \times 10^5$. The color denotes the difference in amplitude between the two branches which is a measure for the amount of bifurcation. The system start to bifurcate at $P = -161\,\text{dBm}$.

We see that the bifurcation point lies at $P_b = -161\,\text{dBm}$. Above this power, close to the resonance frequency two branches emerge between a small frequency range which becomes increasingly broader with increasing power.

Taking into account the attenuation in our setup of around $\sim 60\,\text{dBm}$, this means that all our measurements would be above the bifurcation point. Here we assumed an Josephson gap resistance of $Rj = 2 \times 10^7\,\Omega$. To draw conclusions, we first have to know how the bifurcation power depends on R_j. To this end we derive an analytical expression for the coordinates of the bifurcation point. When we multiply eq. (5.20) in steady-state with its conjugate, we get:

$$\beta = |v|^2 \left(\frac{1}{\Omega^2} + \left(|v|^2 - \text{sgn}(\omega - \omega_d) \right)^2 \right) \tag{5.21}$$

When we write $\rho = |v|^2$ we get the following third order polynomial:

$$\rho^3 - 2sgn(\omega - \omega_d)\rho^2 + \left(1 + \frac{1}{\Omega^2}\right)\rho = \beta \tag{5.22}$$

We get bifurcation when this equation has three solutions for a certain β, which means that the derivative must have two zeros. We find that:

$$\left(\rho - \frac{2}{3} sgn(\omega - \omega_d)\right)^2 = \frac{1}{9} - \frac{1}{3\Omega^2} \tag{5.23}$$

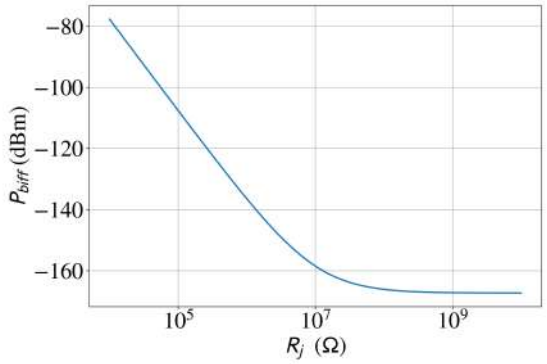

FIGURE 5.21: Bifurcation power as a function of the sub-gap resistance R_j with $C_j = 135\,\text{fF}$. A lower resistance will increase the bifurcation point.

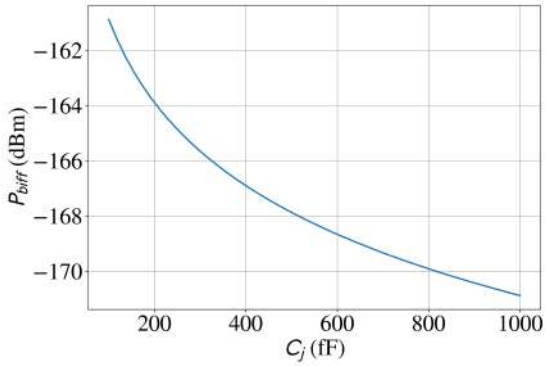

FIGURE 5.22: Bifurcation power as a function of the capacitance shunted with the junction C_j at $R_j = 2 \times 10^7\,\Omega$. Increasing it decreases the bifurcation point.

So the bifurcation starts at $\Omega = 2\tilde{R}\tilde{C}\delta > \sqrt{3}$ and $\beta = \frac{16}{27}$. Using the relations from table 5.2 we can translate this to the detuning δ_b and driving amplitude Φ_b:

$$(\delta_b, \Phi_b) = \left(\frac{\sqrt{3}}{2\tilde{R}\tilde{C}}, \frac{12\sqrt{3}}{\tilde{R}^3 C_j C_c^2 \omega^2(\omega_d)} \right) \tag{5.24}$$

Using $P = \frac{V^2}{2*50}$ we find $P_b = -162\,\text{dBm}$ in agreement with our simulations.

Now we can plot the power coordinate of the bifurcation point as a function of R_j, shown in fig. 5.21. As we expected, the bifurcation power decreases with R_j as it is shunted with the inductor and the capacitor. The higher its resistance, the more current will flow through the inductor and its non-linearity becomes more important. At resistances $R_j > 8 \times 10^7\,\Omega$ the bifurcation power remains constant at $P = -167\,\text{dBm}$. Assuming a resistance of $2 \times 10^7\,\Omega$ all our measurements would be above the bifurcation point. If we assume a lower resistance this would still be the case for most of our measurements as the lowest power we measured was $-145\,\text{dBm}$ (including internal attenuation).

Before we look at the effect of being above the bifurcation point on the S_{11} parameters, we first shortly discuss the role of C_j. In fig. 5.22 we show P_{biff} versus C_j. Again, the bifurcation point decreases with C_j. This can be understood from a similar argument as with R_j, as for a capacitor $Z = \frac{1}{j\omega C}$. Increasing the capacitance will decrease the impedance of the circuit bringing it closer to $Z_0 = 50\,\Omega$ from the input lines and thus requiring less power for the same current.

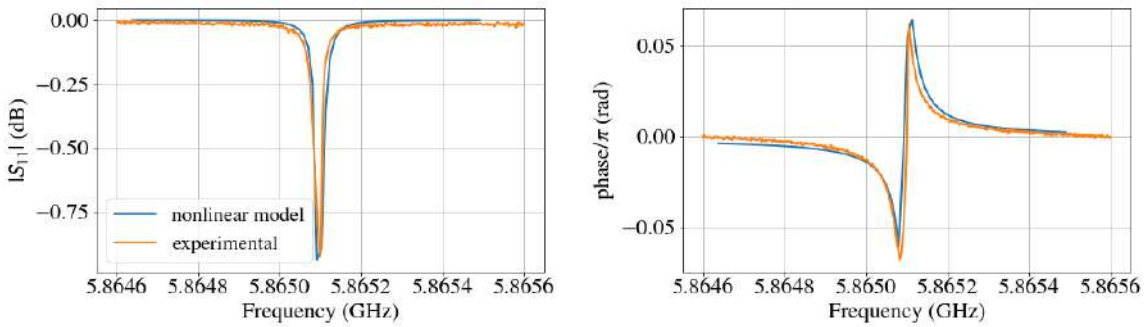

FIGURE 5.23: S_{11} parameters below the bifurcation point at $P = -170\,\text{dBm}$ and $R_j = 1 \times 10^9\,\Omega$. We also plotted the bare resonance which should match the moving peak in the linear regime. We see this is indeed the case.

Finally to see what effect the bifurcation has on the reflection parameters, we plot them both below and above the bifurcation point. To this end we first calculate the impedance:

$$Z = \frac{V}{I} = \frac{\dot{\phi}_d}{I} = \frac{i\omega_d \Phi}{C_c\left(\ddot{\phi}_d - \ddot{\phi}_1\right)} = \frac{i\Phi}{C_c\omega_d\left(\frac{1}{2}(\phi_+ + \phi_-) - \Phi\right)} \tag{5.25}$$

Here $\ddot{\phi}_1 = \frac{1}{2}\left(\ddot{\phi}_+ + \ddot{\phi}_-\right)$. Dropping all terms containing derivatives of $x(\tau)$ as we are in steady state $\ddot{\phi}_- = -2\omega_d^2 x(\tau)e^{i\omega_d t}$, and we $\ddot{\phi}_2 = -\omega_d^2\phi_2$, where we find ϕ_2 from eq. (2.52). Then we can use eq. (2.6) to calculate S_{11}.

As a benchmark, we plot the S_{11} parameters at $P = -170\,\mathrm{dBm}$ and $R_j = 1 \times 10^9\,\Omega$ together with the bare resonance peak in fig. 5.23. From section 5.2.1 we know they should be the same in the linear regime when $R_j > 1 \times 10^9\,\Omega$. We see that this is indeed the case.

Above the bifurcation point at $P = -149\,\mathrm{dBm}$, plotted in fig. 5.24, we see the two branches again. If we scan up in frequency we get similar shape as below the bifurcation point, if we scan the other way round, we obtain a much broader peak. The same holds for the phase: scanning up we have similar behaviour as below P_{biff}, scanning down we get a semicircle. Therefore, even if most of our measurements are above the bifurcation point, we still should see clear signatures of our peak in the reflection parameters. So we conclude that the non-linearity cannot explain the disappearance of our peak.

We also observe a small second peak arising close to the resonance frequency, which we do not expect. We trace back its origin in appendix D.

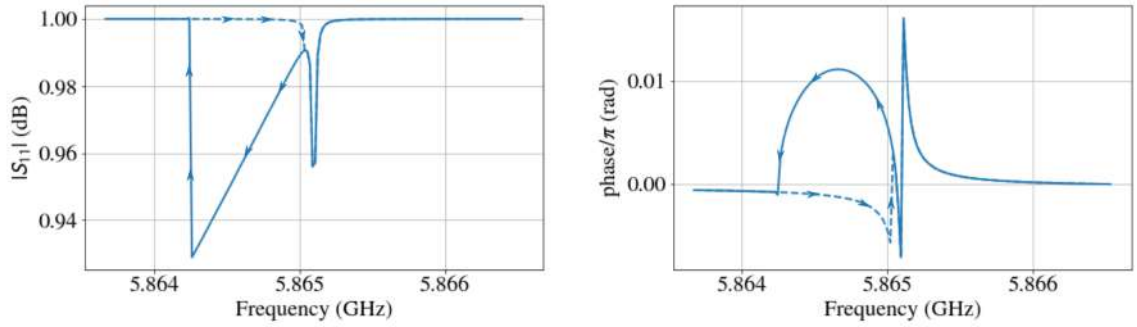

FIGURE 5.24: Amplitude and phase of peak above the bifurcation point at $P = -149\,\mathrm{dBm}$. We get two branches, both should be visible above the bifurcation point.

Chapter 6

Mean field simulations of a Josephson crystal

Because we did not see the moving peak in the one junction device, we never cooled down the five junction device. Still, we can learn more about this device by simulations. In this chapter we use the mean-field code developed by Martin Leib [9] [42] to simulate the synchronization effect for a Josephson crystal consisting of five junctions and explore different regimes.

6.1 Mean field simulations

Here we present the solutions of the master equation eq. (4.8) obtained by a mean field approach, using the code developed by Leib. In fig. 6.1 we show the mode occupancy $\left\langle \hat{b}^{+}\hat{b} \right\rangle$ as a function of the driving strength with the design parameters of our device, but varying C_j. We see that at $C_j = 100\,\mathrm{fF}$, there is no synchronization, but all modes become occupied at a different driving strength. When the capacitance is increased, the transitions become sharper, but the simulations more unstable too.

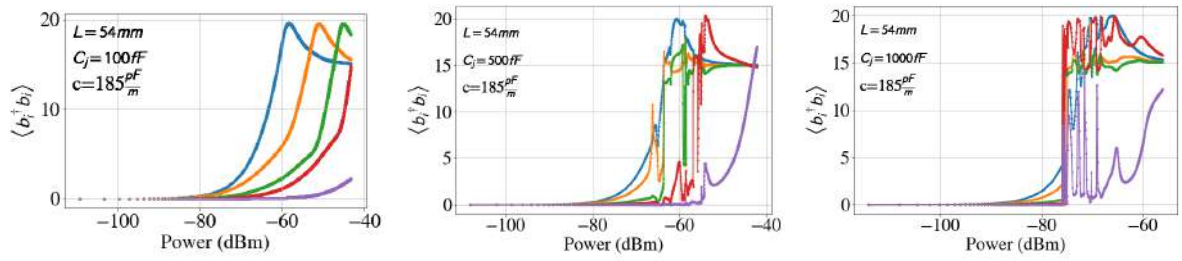

FIGURE 6.1: Mode occupancy as a function of driving strength, driving the crystal with $N_j = 5$ off-resonant at $f - \bar{f} = -4\frac{E_c}{h}$ detuning. With increasing capacitance the transitions become sharper, but no synchronization is observed. The following parameters were used: $L = 54\,\mathrm{mm}$, $l = 460\,\mathrm{nH\,m^{-1}}$, $c = 185\,\mathrm{pF\,m^{-1}}$, $\Omega = 50\,\Omega$ and $C_c = 4\,\mathrm{fF}$.

In fig. 6.2 we plot again the mode occupancy, but now varying the length, keeping the capacitance at $C_j = 1\,\mathrm{pF}$. Only at small lengths of 10 mm the modes become all suddenly occupied at one power. This is in contrary with the suggestion in the paper of Leib that the synchronization can observed experimentally [9], as such a small length requires a frequency of 30 GHz.

We also observed that lowering the length L by a certain factor or the capacitance per unit length c, has the same effect as doubling the Josephson capacitance C_j by that factor. This

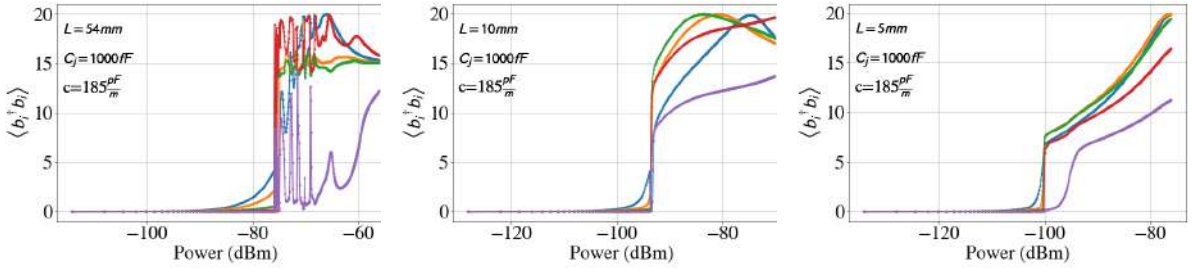

FIGURE 6.2: Mode occupancy at different driving strengths for driving the crystal with $N_j = 5$ off-resonant at $f - \bar{f} = -4\frac{E_c}{h}$ detuning. Now we decrease the length of the device. Only at lengths $\sim$ mm we observe the synchronization effect. The following parameters were used: $L = 54\,\mathrm{mm}$, $l = 460\,\mathrm{nH\,m^{-1}}$, $c = 185\,\mathrm{pF\,m^{-1}}$, $\Omega = 50\,\Omega$ and $C_c = 4\,\mathrm{fF}$.

is illustrated in fig. 6.3. In other words, there seems to be a parameter $\frac{L*c}{C_j}$, the ratio between the resonator capacitance and the Josephson capacitance, which marks different regimes.

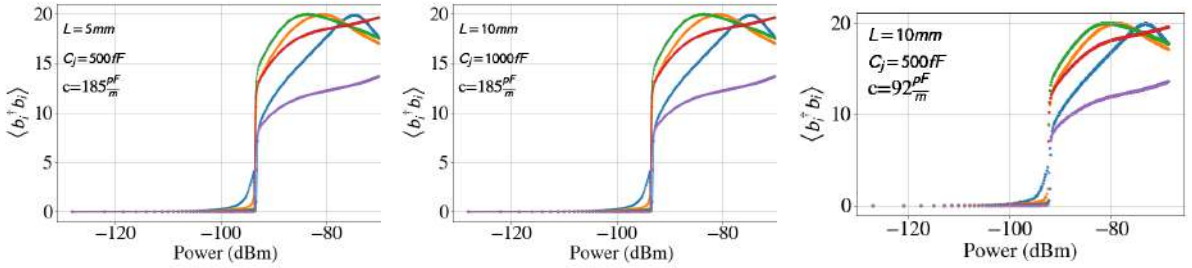

FIGURE 6.3: Mode occupancy as a function of driving strength, driving the crystal with $Nj = 5$ off-resonant at $-4E_c$ detuning. We change the length, Josephson capacitance and capacitance per unit length, but keep the ratio $\frac{Lc}{C_j}$ constant. Apparently, the shape of the graph is determined by this ratio.

Calculating $\frac{L*c}{C_j}$ for fig. 6.1 and fig. 6.2 we can distinguish two regimes:

$$\left\{ \begin{array}{ll} \text{synchronization,} & \text{for } \frac{Lc}{C_j} < 1 \\ \text{no synchronization,} & \text{for } \frac{Lc}{C_j} > 10 \end{array} \right\}$$

6.2 Analytical expressions for flux fluctuations

To gain more understanding what is going on, in fig. 6.4a and fig. 6.4b we plot the analytical expressions of the flux fluctuations λ eq. (4.4) with respect to the reduced magnetic flux quantum $\frac{\phi_0}{2\pi}$ and to the zero point flux fluctuations of a single junction, respectively.

To be in the phase regime it is required that $\lambda/\phi_0 < 1$. We see that for all modes this ratio in the upper left, which is the regime where we observe synchronization, is the lowest. Moving to the lower right by increasing the length and decreasing the capacitance the ratio increases. Still, the requirement $\lambda/\phi_0 < 1$ is met everywhere.

From eq. (4.3), it follows that for the inter mode coupling g to be pertubative $\frac{\lambda}{\lambda_0} \sim 1$. The same trend can be observed as with the previous plot, that moving from the regime where we observe synchronization to the regime where we do not, means we move away from this

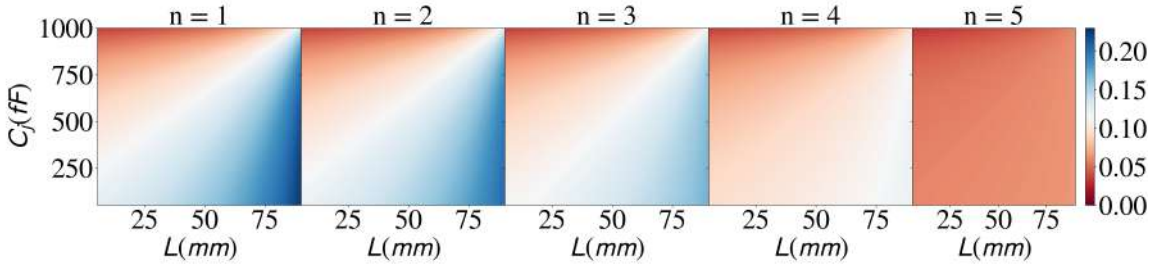

(A) λ/ϕ_0

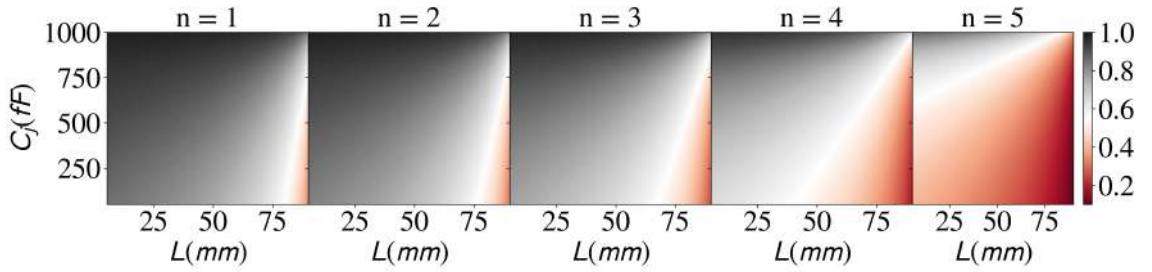

(B) λ/λ_0

FIGURE 6.4: Flux fluctuations as a function of the total length L and the capacitance C_j compared to the reduced magnetic flux quantum $\frac{\phi_0}{2\pi}$ and the flux fluctuation of a single junction λ_0. To be in the phase regime, $\lambda/\phi_0 \ll 1$. For the coupling g to be pertubative, $\lambda/\lambda_0 \sim 1$.

condition. Here the effect is stronger and in the lower right corner the condition is not met anymore. Looking again at the expression of g:

$$g_{j,l} = (2/N+1)\sum_{n=1}^{N} \sin(jp_n)\sin(lp_n)\left[\frac{\lambda}{\lambda_0} - 1\right] \tag{6.1}$$

With:

$$\frac{\lambda}{\lambda_0} = \sqrt{\frac{1}{1 + \frac{Lc}{4C_j(N_j+1)}\left[1 + \cos\left(n\frac{\pi}{N+1}\right)\right]}} \tag{6.2}$$

We see that it indeed depends on the parameter $\frac{Lc}{C_j}$.

Chapter 7

Classical model for the Josephson crystal: simulations of two degenerate Duffing oscillators with a purely nonlinear coupling

To get a better understanding of the synchronization effect, we simplify our problem by considering a Josephson crystal of only two junctions. We take a classical approach in a similar fashion as with the one junction device (see section 5.2.3). First we derive the equations of motion for the lumped-element equivalent of a Josephson crystal with two junctions, shown in fig. 7.1. Then we Taylor expand these equations taking into account the non-linearity of the junctions up to the first order. Like this get two non-linearly coupled Duffing oscillators. Then, we parameterize the coupling between the two circuits such that we can turn it off and on. This is described in section 7.1. Next, as with the one-junction device, we apply the Krylov–Bogoliubov method to filter out the fast oscillations, such that we can numerically integrate using bigger time steps. This is explained in section 7.2. In section 7.3 we discuss the results.

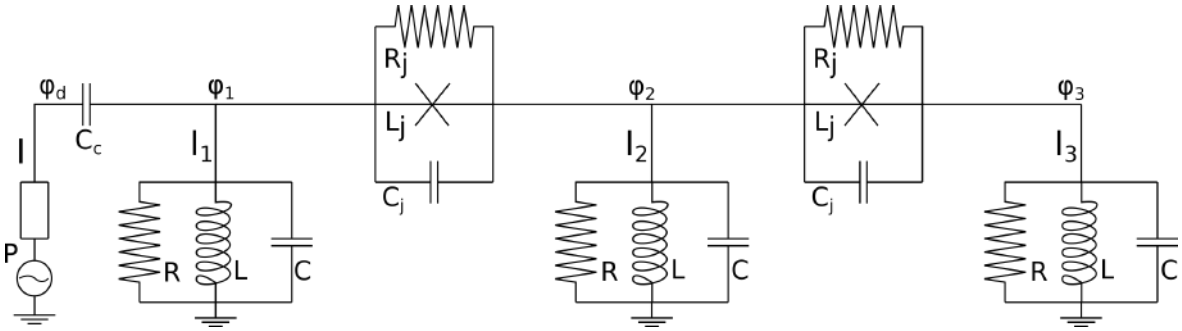

FIGURE 7.1: Lumped element model of two coupled non-linear oscillators. The system is described by three generalized node fluxes, ϕ_1, ϕ_2 and ϕ_3.

7.1 Equations of motion

We start the classical description of the circuit shown in fig. 7.1 by introducing the generalized node fluxes ϕ_1, ϕ_2 and ϕ_3 as explained in section 2.3. From Kirchhoff's laws we get the following equations for the RLC circuits:

$$C\ddot{\phi}_n + \frac{1}{R}\dot{\phi}_+ \frac{1}{L}\phi_n = I_n \tag{7.1}$$

With $n \in \{1, 2, 3\}$. Then we write $\phi_{12} = \phi_1 - \phi_2$ and $\phi_{23} = \phi_2 - \phi_3$ and arrive at a second set of equations for the capacitively shunted junctions:

$$C_j \ddot{\phi}_{12} + \frac{1}{R_j}\dot{\phi}_{12} + I_0 \sin\frac{\phi_{12}}{\phi_0} = I_2 + I_3 \tag{7.2}$$

$$C_j \ddot{\phi}_{23} + \frac{1}{R_j}\dot{\phi}_{23} + I_0 \sin\frac{\phi_{23}}{\phi_0} = I_3 \tag{7.3}$$

Now we move to a new basis with:

$$\phi_k = \phi_1 + \phi_2 + \phi_3 \tag{7.4}$$

$$\phi_l = \frac{\phi_{12} + \phi_{23}}{2} = \frac{\phi_1 - \phi_3}{2} \tag{7.5}$$

$$\phi_m = \frac{\phi_{12} - \phi_{23}}{2} = \frac{\phi_1 - 2\phi_2 + \phi_3}{2} \tag{7.6}$$

Here, ϕ_k is the mode where ϕ_1, ϕ_2 and ϕ_3 move in phase, and therefore does not involve the junction. ϕ_l is the mode where ϕ_1 and ϕ_3 move in anti-phase and $\phi_2 = 0$. Finally, ϕ_m is associated with ϕ_1 and ϕ_3 moving in phase and ϕ_2 moving in anti-phase with them. This is shown in fig. 7.2:

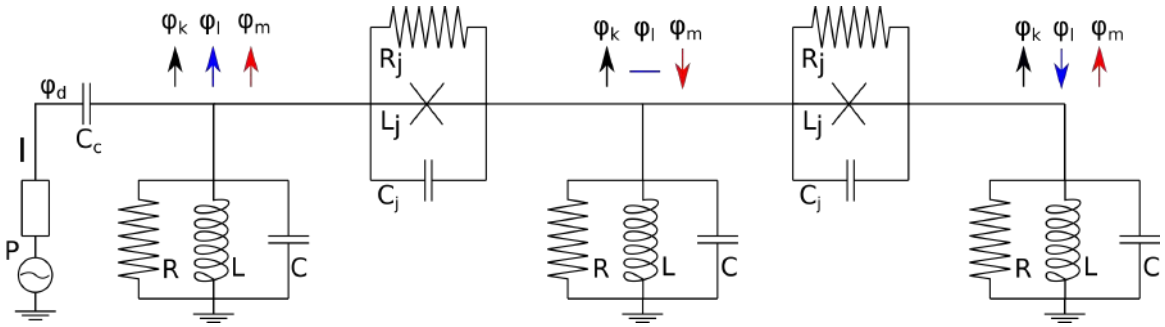

FIGURE 7.2: Lumped element model of two coupled non-linear oscillators. We moved to a new basis with generalized node fluxes, ϕ_k (black), ϕ_l (blue) and ϕ_m (red). ϕ_l is zero in the middle.

Using that $I \approx C_c \ddot{\phi}_d$ we get:

$$C\ddot{\phi}_k + \frac{1}{R}\dot{\phi}_k + \frac{1}{L}\phi_k = C_c \ddot{\phi}_d \tag{7.7}$$

So as expected we have one uncoupled harmonic equation, not involving the junction, with resonance frequency $f = \bar{f} = \frac{1}{2\pi\sqrt{LC}}$. By adding and subtracting eq. (7.2) and eq. (7.3) we get our other two equations:

$$(C_j + C)\ddot{\phi}_l + (\frac{1}{R_j} + \frac{1}{R})\dot{\phi}_l + C\frac{1}{LC}\phi_l + C_j\frac{I_0}{C_j}\cos\frac{\phi_m}{\phi_0}\sin\frac{\phi_l}{\phi_0} = C_c\frac{\ddot{\phi}_d}{2} \tag{7.8}$$

$$(C_j + \frac{1}{3}C)\ddot{\phi}_m + (\frac{1}{R_j} + \frac{1}{3R})\dot{\phi}_m + \frac{C}{3}\frac{1}{LC}\phi_m + C_j\frac{I_0}{C_j}\cos\frac{\phi_l}{\phi_0}\sin\frac{\phi_m}{\phi_0} = \frac{1}{6}C_c\ddot{\phi}_d \tag{7.9}$$

Here we used $\sin(\phi_{12}) \pm \sin(\phi_{23}) = 2\sin\left(\frac{\phi_{12}\pm\phi_{23}}{2}\right)\cos\left(\frac{\phi_{12}\mp\phi_{23}}{2}\right)$. In case eq. (7.2) and eq. (7.3) were linear, we would have two uncoupled harmonic equations, again with resonance frequency $f = \bar{f} = \frac{1}{2\pi\sqrt{LC}}$. So by diagonalizing the set of node fluxes ϕ_1, ϕ_2 and ϕ_3 we arrived at the peculiar situation of three normal modes all having the same frequency $f = \bar{f}$. There is no linear coupling, only a non-linear coupling between ϕ_l and ϕ_m.

Now we focus on eq. (7.8) and approximate the sine and cosine by a Taylor expansion, keeping only terms up to third order:

$$\frac{I_0}{C_j}\cos\frac{\phi_m}{\phi_0}\sin\frac{\phi_l}{\phi_0} \approx \frac{I_0}{C_j}(1-\frac{1}{2}(\frac{\phi_m}{\phi_0})^2)(\frac{\phi_l}{\phi_0}-\frac{1}{6}(\frac{\phi_l}{\phi_0})^3) \approx \frac{I_0}{C_j}(\frac{\phi_l}{\phi_0}-\frac{1}{2}(\frac{\phi_m}{\phi_0})^2\frac{\phi_l}{\phi_0}-\frac{1}{6}(\frac{\phi_l}{\phi_0})^3) \quad (7.10)$$

Now we replace the factor $\frac{1}{2}$ with $\frac{J}{2}$ to parametrize the coupling between the modes. We do the same for eq. (7.9). This finally gives the equations we want to solve for:

$$\ddot{\phi}_k + \frac{1}{RC}\dot{\phi}_k + \omega^2\phi_k = \frac{C_c}{C}\ddot{\phi}_d \quad (7.11)$$

$$\ddot{\phi}_l + \frac{1}{C_j+C}\left(\frac{1}{R_j}+\frac{1}{R}\right)\dot{\phi}_l + \omega^2\phi_l - \frac{\omega^2 C_j}{2\phi_0^2(C_j+C)}\left(J\phi_m^2\phi_l + \frac{1}{3}\phi_l^3\right) = \frac{C_c}{C_j+C}\frac{\ddot{\phi}_d}{2} \quad (7.12)$$

$$\ddot{\phi}_m + \frac{1}{C_j+\frac{1}{3}C}\left(\frac{1}{R_j}+\frac{1}{3R}\right)\dot{\phi}_m + \omega^2\phi_m - \frac{\omega^2 C_j}{2\phi_0^2(C_j+\frac{1}{3}C)}\left(J\phi_l^2\phi_m + \frac{1}{3}\phi_m^3\right) = \frac{C_c}{C_j+\frac{1}{3}C}\frac{\ddot{\phi}_d}{6} \quad (7.13)$$

According to eq. (2.33), all three modes have a different coupling to the drive:

$$Q_{\text{ext},k} = \frac{C+C_c}{4\pi^2\bar{f}C_c^2 Z_0} \qquad Q_{\text{ext},l} = \frac{4(C+C_j)}{C}Q_{\text{ext},k} \qquad Q_{\text{ext},m} = \frac{12(C+3C_j)}{C}Q_{\text{ext},k} \quad (7.14)$$

In fig. 7.3 we summarize the situation. We have three degenerate normal modes ϕ_k, ϕ_l and ϕ_m, capacitively coupled to a drive. ϕ_k does not involve the junction and is therefore linear and not coupled to the other modes. ϕ_l and ϕ_m are non-linear themselves (self-Kerr), have a lower coupling to the drive, and are non-linearly coupled to each other (cross-Kerr), parameterized by J.

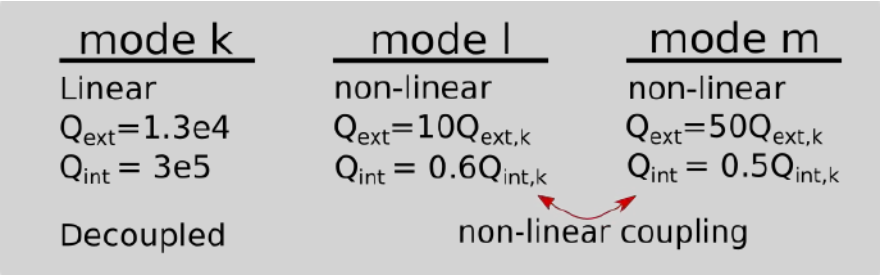

FIGURE 7.3: We have three degenerate normal modes labeled 'k', 'l' and 'm' capacitively coupled to a drive. Mode k is linear and not coupled to the other modes. Mode l and m are non-linear (self Kerr), have a lower coupling to the drive, and are non-linearly coupled to each other (cross Kerr), parameterized by J. Here the parameters of table 7.2 are used.

7.2 Krylov-Bogoliubov method

We apply a harmonic drive $\phi_d = \Phi\cos(\omega_d t)$. We are only interested in the envelope function and therefore filter out the fast oscillations at the drive frequency $f_d = 2\pi\omega_d$, using again the Krylov–Bogoliubov method (section 5.2.3). We write:

$$\phi_l = [x(\tau)e^{i\omega_d t} + x(\tau)^* e^{-i\omega_d t}] \tag{7.15}$$

$$\dot{\phi}_l \approx i\omega_d[xe^{i\omega_d t} - x^* e^{-i\omega_d t}] \tag{7.16}$$

$$\ddot{\phi}_l \approx -\omega_d^2[xe^{i\omega_d t} + x^* e^{-i\omega_d t}] + 2i\omega_d[\frac{dx}{d\tau}e^{i\omega_d t} - \frac{dx^*}{d\tau}e^{-i\omega_d t}]\delta \tag{7.17}$$

Where we introduced the slow moving variable $\tau = |\omega - \omega_d|t = \delta t$. We get the same for ϕ_m but then $x \to y$. Moving to a rotating frame by multiplying both sides of eq. (7.12) with $e^{-i\omega_d t}$, dropping the fast moving terms and writing $C_c\ddot{\phi}_d e^{-i\omega_d t} \approx -\frac{C_c\omega_d^2\Phi}{2}$ gives us:

$$(i\omega_d x + 2i\omega_d\frac{dx}{d\tau}\delta) + \frac{1}{\tilde{R}_l\tilde{C}_l}i\omega_d x + \omega_0^2 x(\tau) - \frac{C_j\omega^2}{2\phi_0^2\tilde{C}_l}\left(J\phi_m^2\phi_l + \frac{1}{3}\phi_c^3\right) = -\frac{C_c\omega_d^2\Phi}{4\tilde{C}_l} \tag{7.18}$$

Here we introduced $\tilde{C}_l = C_j + C$ and $\frac{1}{\tilde{R}_l} = \frac{1}{R_j} + \frac{1}{R}$. Now we use that

$$\phi_l^3 e^{-i\omega_d t} \approx 3|x|^2 x \tag{7.19}$$

$$\phi_m^2\phi_l e^{-i\omega_d t} \approx 2|y|^2 x + x^* y^2 \tag{7.20}$$

This gives after rescaling $x = \frac{v}{\sqrt{\frac{C_j\omega_0^2}{4\tilde{C}_l\omega_d\delta\phi_0^2}}}$, $y = \frac{w}{\sqrt{\frac{C_j\omega_0^2}{4\tilde{C}_m\omega_d\delta\phi_0^2}}}$ the following two equations:

$$\begin{aligned}
\frac{dv}{d\tau} &= -\frac{v}{\Omega_b} - i\left(v|v|^2 - vsgn(\omega-\omega_d) + 2J\frac{\tilde{C}_m}{\tilde{C}_l}v|w|^2 + J\frac{\tilde{C}_m}{\tilde{C}_l}v^* w^2\right) + i\sqrt{\beta_l} \\
\frac{dw}{d\tau} &= -\frac{w}{\Omega_c} - i\left(w|w|^2 - wsgn(\omega-\omega_d) + 2J\frac{\tilde{C}_l}{\tilde{C}_m}w|v|^2 + J\frac{\tilde{C}_l}{\tilde{C}_m}w^* v^2\right) + i\sqrt{\beta_m}
\end{aligned} \tag{7.21}$$

With the definitions summarized in table 7.1.

Table 7.1: Normalized parameter definitions of two coupled Duffing oscillators labeled by 'l' and 'm'.

Parameter	Definition	Parameter	Definition
$\tilde{C}_l$	$C_j + C$	$\tilde{C}_m$	$C_j + \frac{1}{3}C$
$\frac{1}{\tilde{R}_l}$	$\frac{1}{R_j} + \frac{1}{R}$	$\frac{1}{\tilde{R}_m}$	$\frac{1}{R_j} + \frac{1}{3R}$
Ω_l	$2\tilde{R}_l\tilde{C}_l\delta$	Ω_m	$2\tilde{R}_m\tilde{C}_m\delta$
β_l	$\frac{C_c^2 C_j}{256\tilde{C}_l{}^3}\frac{\omega_d\omega_0^2}{\delta^3}\frac{\Phi^2}{\phi_0^2}$	β_m	$\frac{1}{9}\left(\frac{\tilde{C}_l}{\tilde{C}_m}\right)^3\beta_l$
v	$x\sqrt{\frac{C_j\omega^2}{4\tilde{C}\omega_d\delta\phi_0^2}}$	w	$y\sqrt{\frac{C_j\omega_0^2}{4\tilde{C}_m\omega_d\delta\phi_0^2}}$

7.3 Results

We solve eq. (7.21) by Runge-Kutta integration using the system parameters from table 7.2. The typical time to reach equilibrium is given by $t_{\text{eq}} = \frac{2}{\kappa}$. To be sure we arrive at equilibrium we let the system evolve over a time $4t_{\text{eq}}$. Because we transformed to the slowly moving variable τ this translates into $\tau_{total} = 4t_{\text{eq}}\delta = \frac{4Q}{\pi f_0}\delta$. We use time steps $h = 0.06$. Note that we need a three times smaller time step than with the single Duffing oscillator (see section 5.2.3).

TABLE 7.2: System parameters of non-linearly coupled Duffing oscillators

Parameter	Value
C_j	1 pF
C	0.8 pF
C_c	4 fF
R_j	1 MΩ
$Q_{\text{int,k}}$	3×10^5
$Q_{\text{ext,k}}$	1.3×10^4
$\bar{f}$	6 GHz

In fig. 7.4 we plot ϕ_l and ϕ_m as a function of frequency, for low power $P = -200\,\text{dBm}$, such that the modes are linear. We turn off the inter-mode coupling too by setting $J = 0$. As expected, we get two harmonic peaks, both at $f = \bar{f}$. They have a different height as they have a different coupling to the drive due to their different effective capacitances, as we know from eq. (7.14). In fig. 7.5 we compare them with the height of the bare peak.

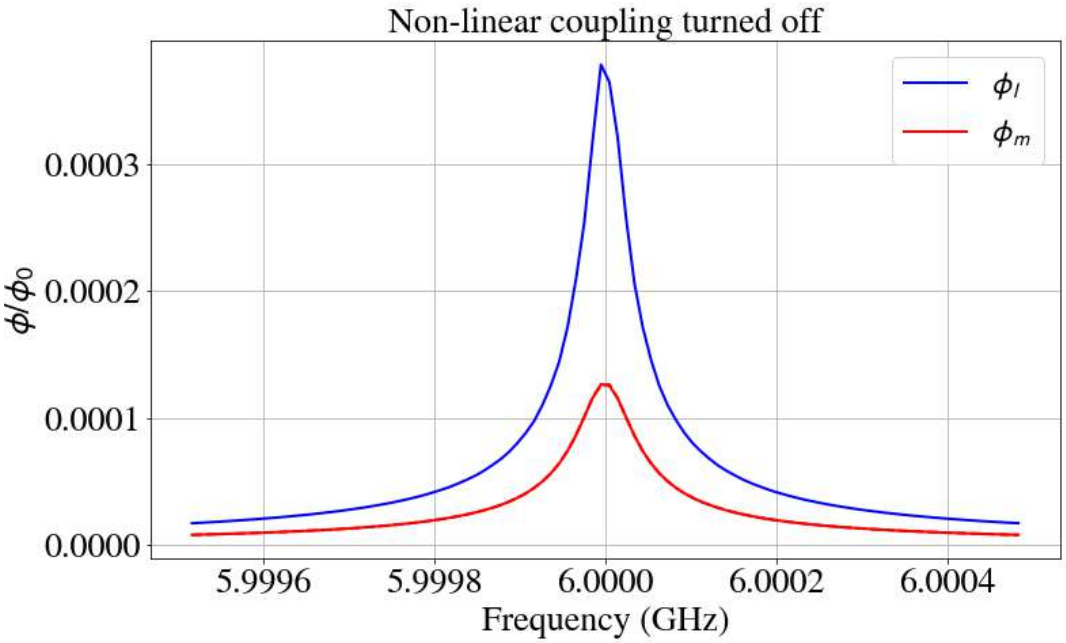

FIGURE 7.4: Generalized fluxes ϕ_l and ϕ_m for $P = -200\,\text{dBm}$. Because we are at low power, the modes are linear. We set $J = 0$ such that the non-linear inter mode coupling is switched off too. We see that in this case we get two harmonic peaks both at the same frequency $f = \bar{f}$.

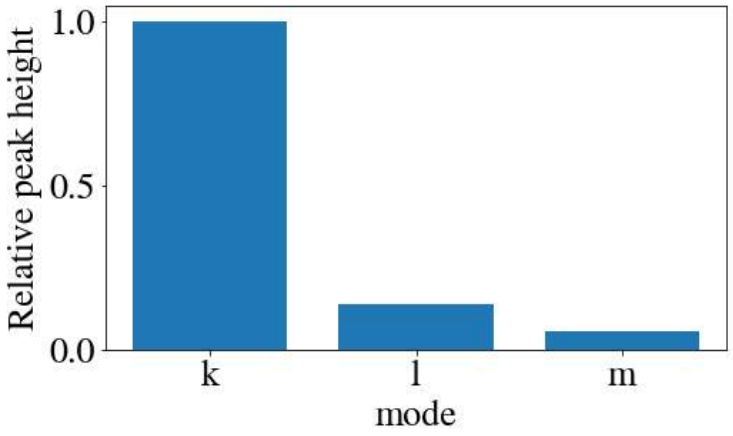

FIGURE 7.5: Relative driven amplitude for same input driving for the modes 'k', 'l' and 'm'. All modes are coupled different to the drive due to their different effective capacitances.

Next we plot ϕ_l and ϕ_m above the bifurcation point of ϕ_l for two different powers, $P = -165\,\text{dBm}$ and $P = -159\,\text{dBm}$, in fig. 7.6. The inter-mode coupling is still turned off. Here we clearly see that these modes are non-linear. At $P = -165\,\text{dBm}$ ϕ_l bifurcates and ϕ_m gets distorted (its peak is shifted to the left). At $P = -159\,\text{dBm}$ they both bifurcate.

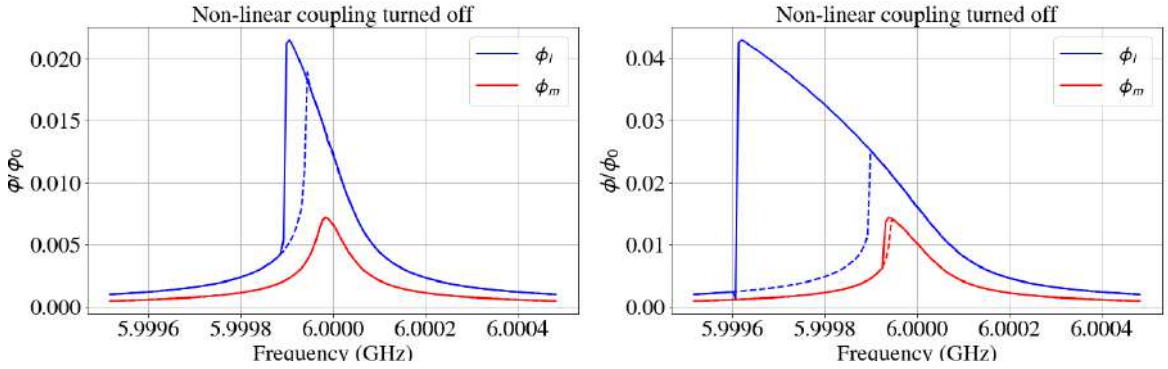

(A) P = −165 dBm (B) P = −159 dBm

FIGURE 7.6: Generalized fluxes ϕ_l and ϕ_m for $P = -165\,\text{dBm}$ and $P = -159\,\text{dBm}$. We set $J = 0$ such that the non-linear inter mode coupling is switched off. The dashed line denotes the lower branch (scanning up in frequency), the solid line the upper branch (scanning down). At $P = -165\,\text{dBm}$ we are above the bifurcation point of ϕ_l and below the bifurcation point of ϕ_m. At $P = -159\,\text{dBm}$ they both bifurcate.

Now we look what happens when we turn on the non-linear coupling by setting $J = 1$ in fig. 7.7. At $P = -165\,\text{dBm}$ ϕ_m now bifurcates too. This suggests that the bifurcation point of ϕ_m is lowered by ϕ_l. Furthermore, now, at both powers, the two degenerate non-linear oscillators synchronize their jump-down frequencies. This is an important result, as it shows that in a fully classical treatment of two non-linearly coupled Duffing oscillators, there is a similar effect as the synchronization effect in a Josephson crystal predicted from a quantum mechanical analysis.

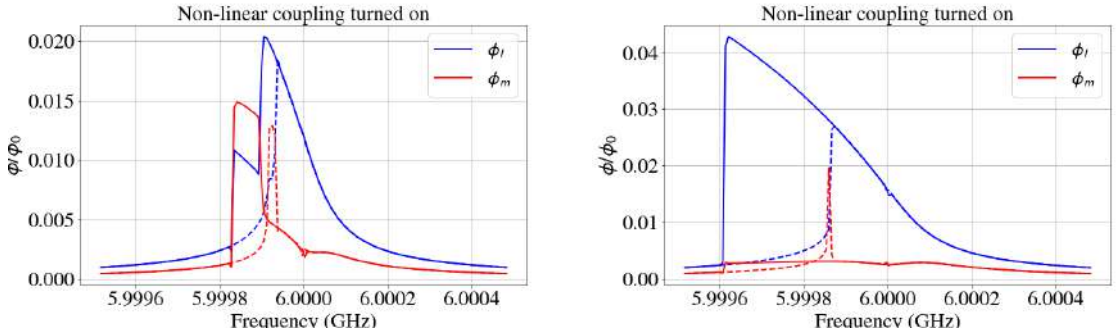

(A) P = −165 dBm (B) P = −159 dBm

FIGURE 7.7: Generalized fluxes ϕ_l and ϕ_m for $P = -165\,\text{dBm}$ and $P = -159\,\text{dBm}$. Now we turn on the non-linear coupling by setting $J = 1$. The dashed line indicates the lower branch (scanning up in frequency), the solid line the upper branch (scanning down). Surprisingly, the jump-down frequencies of the two modes are synchronized. Note that now at $P = -165\,\text{dBm}$ both modes are bifurcated, in contrast to the case $J = 0$.

In fig. 7.8 we plot the upper branches of ϕ_l and ϕ_m for different powers. The shape and power dependence of ϕ_l is similar to the upper branch of a Duffing oscillator. The jump-down frequency of ϕ_m keeps being synchronized with ϕ_l. Its shape becomes lower and flatter with increasing power..

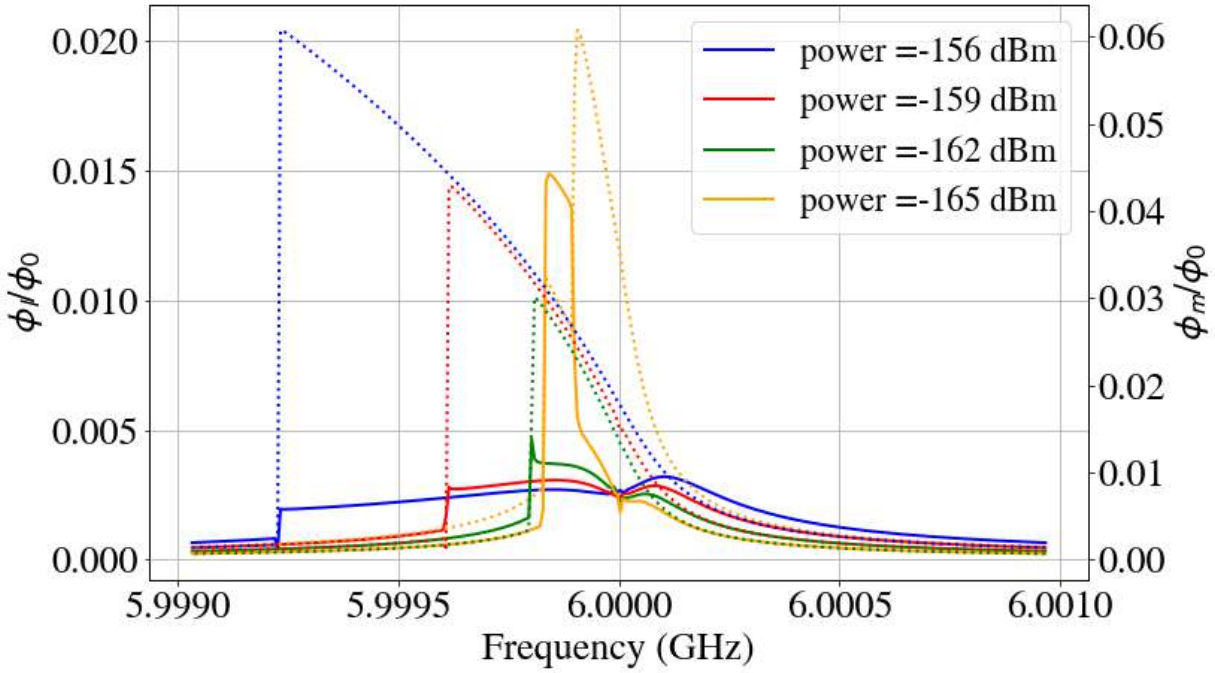

FIGURE 7.8: Generalized fluxes ϕ_l and ϕ_m for different powers scanning down in frequency (upper branch). For all powers the jump down frequencies of ϕ_l (dotted) and ϕ_m (solid) synchronize. For higher powers ϕ_m becomes lower. Note that we used different scales for ϕ_l and ϕ_m because ϕ_m is much lower than ϕ_l.

The mechanism behind the synchronization is not exactly clear, and is an open question for further research. A hint in the right direction could be in the phase. We observed that

above $\bar{f}$, before the modes bifurcate, they tend to increase the mutual phase difference, shown in fig. 7.9. Close to the jump-down frequency they synchronize their phases again.

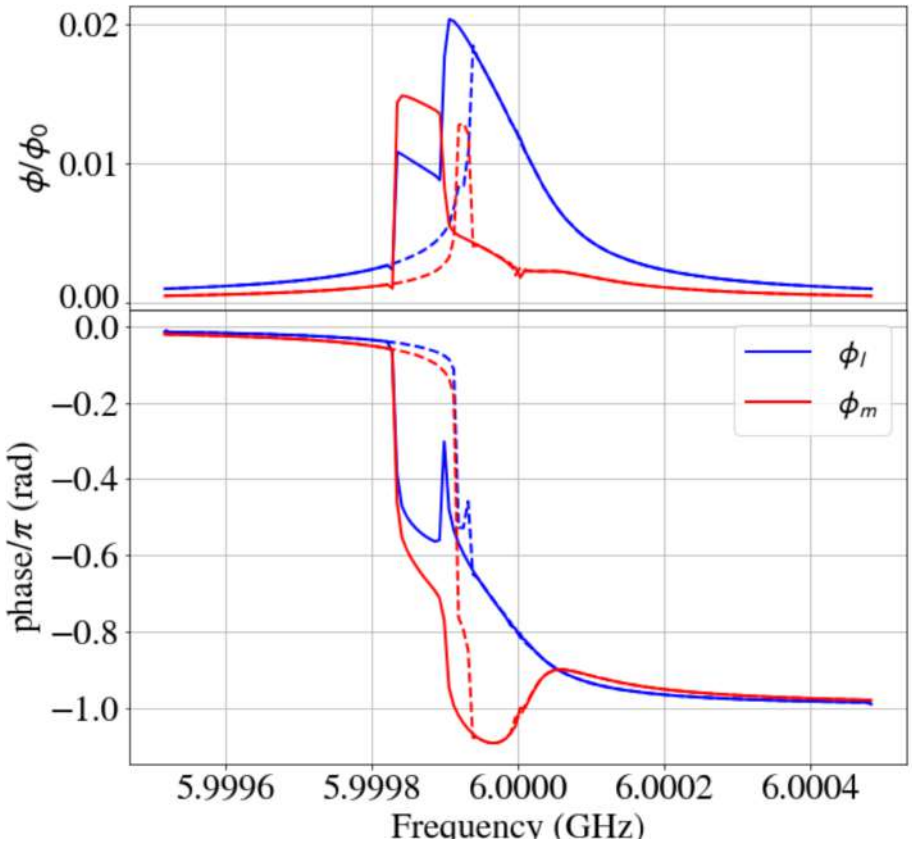

FIGURE 7.9: Phases of ϕ_l and ϕ_m at $P = -165$ dBm, with the non-linear coupling turned on. The solid line is again the upper branch, and the dashed line the lower branch. Before they bifurcate, above $\bar{f}$ the tend to increase the mutual phase difference. This could be a hint for understanding the mechanism behind the synchronization.

Chapter 8

Conclusions and outlook

Concerning the ground state quenching of a CPW we found that the coupling must be tuned faster than 1/f. Second we found that a higher initial coupling results in a higher excitation number. Tuning the coupling from 1 GHz to 0 faster than 10 ps results in an photon number of 0.1. This is experimentally unfeasible with current state of the art electronics. Second, the high coupling demands capacitors at the order of picofarads, which makes the fabrication challenging too.

During the cool-down of the one junction device we only observed the bare resonance not involving the junctions which we found was due to the combination of the high flux noise in the fridge ($\Delta\phi \approx 0.03\phi_0$) and our device being undercoupled ($g \approx 0.1$). From our linear model made in `QUCS` we excluded the possibility that a low Josephson sub-gap caused the disappearance. Based on our non-linear Duffing model of this device we also found that nearly all our measurements were done above the bifurcation point, but this has no effect on the visibility of the moving peak.

Contrary to what was claimed in the theoretical proposal, the synchronization effect cannot be observed for the parameters common in cQED. We found that the occurrence of the synchronization effect depends on the ratio of the total capacitance of the CPW and the capacitance shunted with a single junction $\frac{L*c}{C_j}$ being as low as possible. Achieving this is challenging with conventional cQED. One way would be to push the limits of the capacitances to several picofarads.

Finally, we observed a synchronization effect in our simulation of two degenerate non-linearly coupled Duffing oscillators. This is a first step in understanding the synchronization effect in a Josephson crystal in a fully classical way. As a next step towards a full understanding of this effect, it would be very interesting to explore different parameter regimes, consider the phases of both oscillators and look at the time dynamics.

Appendix A

Three plus one junction device

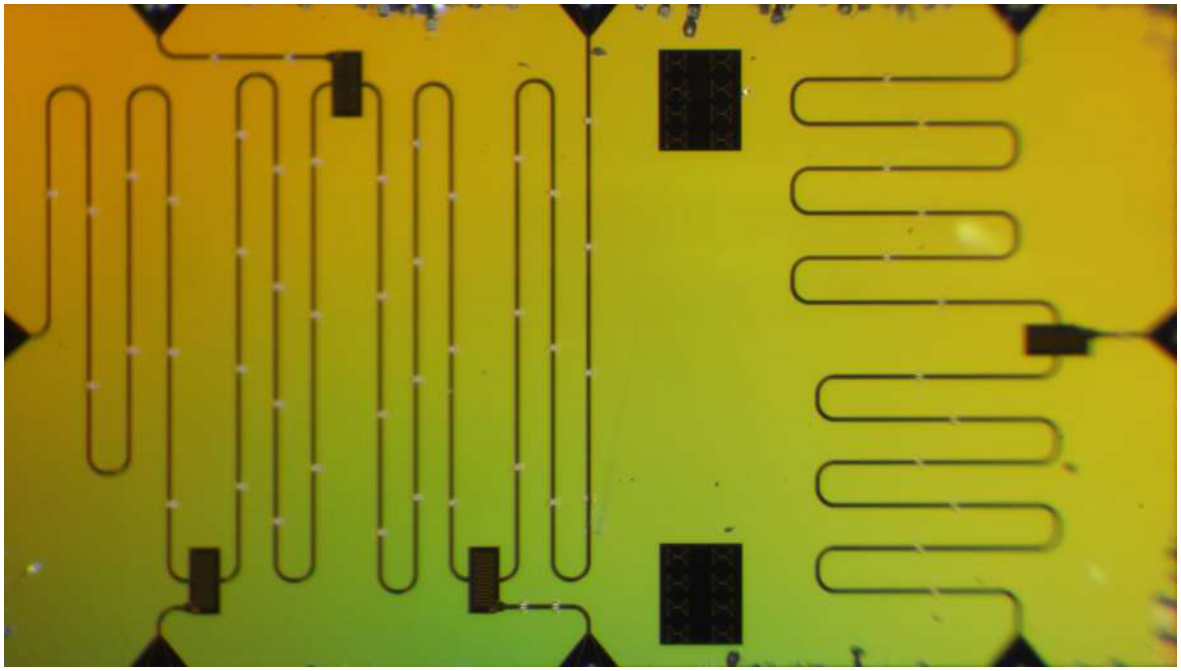

FIGURE A.1: Optical image of our second device with two Josephson crystals: one with three junctions and one with one junction.

TABLE A.1: Parameters of the CPW's

Single CPW length Δ	9 mm
width W	12 µm
gap G	4 µm
capacitance per unit length c	$0.18\,\mathrm{nF\,m^{-1}}$
inductance per unit length l	$0.46\,\mathrm{\mu H\,m^{-1}}$
phase velocity v	$1.08 \times 10^8\,\mathrm{m\,s^{-1}}$
resonance frequency $\bar{f}$	6 GHz

Appendix B

Python code

B.1 stcad additions

Below the definition of the CPW object is shown, together with the two functions we added: 'add_airbridges' and 'add_mask'.

B.1.1 CPW

```
class CPW(cad.core.Cell):

    def __init__(self,
        points,
        turn_radius = 5.,
        pin = 4.,
        gap = 2.,
        layer = 1,
        name=''):

        super(CPW, self).__init__(name)
        cad.core.default_layer = layer
        points = np.array(points)
        self.points = points
        self.length = 0.
        self.pin = pin
        self.gap = gap
        self.layer = layer
        self.turn_radius = turn_radius

        if len(points) == 2:
            self.add(double_line_polygon(points[0],points[1],gap,pin))
            self.length += norm(points[1]-points[0])
        else:
            n_last = len(points)-1
            sec = [points[0]]
            for i in range(1,n_last):
                p = np.array(points[i])
                p_before = np.array([points[i][0]+turn_radius*sign(points[i-1][0]
                    -points[i][0]),points[i][1]+turn_radius*sign(points[i-1][1]
                    -points[i][1])])
                p_after = np.array([points[i][0]+turn_radius*sign(points[i+1][0]
                    -points[i][0]),points[i][1]+turn_radius*sign(points[i+1][1]
```

```
                    -points[i][1])])
                curve_center = p_after + p_before - p
                angle_i = angle(p_before - curve_center)
                angle_delta = angle(p_after - curve_center)-angle_i
                if angle_delta < -180.:
                    angle_delta+=360.
                if angle_delta > 180.:
                    angle_delta-=360.

                sec.append(p_before)
                self.add(double_line_polygon(sec[0],sec[1],gap,pin))
                angles = np.linspace(angle_i,angle_i+angle_delta, 199).T *np.pi/180.
                self.length += norm(sec[1]-sec[0])
                self.add(double_arc_polygon(curve_center, turn_radius,gap,pin,\
                                    initial_angle=angle_i, final_angle=angle_i+angle_delta,
                            number_of_points = 199))
                self.length += 2*np.pi*turn_radius*abs(angle_delta)/360.
                sec=[p_after]
            sec.append([points[n_last][0],points[n_last][1]])
            self.add(double_line_polygon(sec[0],sec[1],gap,pin))
            self.length += norm(sec[1]-sec[0])

def add_airbridges(self, size_block, size_bridge, width, spacing, layers = [2,3]):
        rect_block_1 = cad.shapes.Rectangle( (-width/2 - size_block[0], -size_block[1]/2),
        (-width/2, size_block[1]/2), layer = layers[0] )
        rect_block_2 = cad.shapes.Rectangle( (width/2, -size_block[1]/2), (width/2 +
                size_block[0],
        size_block[1]/2), layer = layers[0] )
        rect_bridge = cad.shapes.Rectangle( (-size_bridge[0]/2, -size_bridge[1]/2),
        (size_bridge[0]/2, size_bridge[1]/2) , layer = layers[1])
        cell = cad.core.Cell('bridge')
        cell.add(rect_block_1)
        cell.add(rect_block_2)
        cell.add(rect_bridge)

        for i in range(len(self.points)-1):
            points = np.array(self.points)
            rd = ( points[i+1]-points[i] ) # relative distances between two points

            if int(rd[0]) != 0 and int( ( abs(rd[0]) - 2*self.turn_radius)/spacing ) > 0:
                for j in range(0, int( ( abs(rd[0]) - 2*self.turn_radius)/spacing )):
                    x = points[i][0] + np.sign(rd[0])*(spacing/2. + j*spacing)
                    self.add(cell, origin = ( x, points[i][1]), rotation = 90)

            elif int ((abs(rd[1]) - 2*self.turn_radius)/spacing) > 0:
                for j in range(0, int( ( abs(rd[1]) - 2*self.turn_radius)/spacing )):
                    y = points[i][1] + np.sign(rd[1])*(spacing/2. + j*spacing)

    def add_mask( self, width , layer=91):
    """
        this functions returns a mask following the centreline of  the CPW.
        This can also be used as a skirt for the holyeground
```

```
    """

        cad.core.default_layer = layer
        points = self.points
        turn_radius = self.turn_radius

        if len(points) == 2:
            self.add( line_polygon(points[0], points[1], width))
            self.length += norm(points[1]-points[0])
        else:
            n_last = len(points)-1
                sec = [points[0]]
            for i in range(1,n_last):
                p = np.array(points[i])
                p_before = np.array([points[i][0]+turn_radius*sign(points[i-1][0]-
                points[i][0]),points[i][1]+turn_radius*sign(points[i-1][1]-points[i][1])])
                p_after = np.array([points[i][0]+turn_radius*sign(points[i+1][0]-
                points[i][0]),points[i][1]+turn_radius*sign(points[i+1][1]-points[i][1])])
                curve_center = p_after + p_before - p
                angle_i = angle(p_before - curve_center)
                angle_delta = angle(p_after - curve_center)-angle_i

                if angle_delta < -180.:
                    angle_delta+=360.
                if angle_delta > 180.:
                    angle_delta-=360.

                sec.append(p_before)
                self.add(line_polygon(sec[0], sec[1],  width))
                angles = np.linspace(angle_i,angle_i+angle_delta, 199).T *np.pi/180.
                self.length += norm(sec[1]-sec[0])
                self.add(arc_polygon(curve_center, turn_radius,width,\
                                    initial_angle=angle_i, final_angle=angle_i+angle_delta,
                            number_of_points = 199))
                sec=[p_after]
            sec.append([points[n_last][0],points[n_last][1]])
            self.add( line_polygon(sec[0], sec[1], width))
```

B.1.2 Interdigitated capacitor

To make our capacitively shunted junctions in Python we wrote the interdigitated capacitor object, which can be instantiated with and without a SQUID.

```
class interdigitated_cap(cad.core.Cell):
    """
    Make a cell with interdigitated cap surrounded by a dielectric with width set
    by 'dielectric'.  A skirt can be added by setting 'add_skirt' to True.
    This class also contains a function which adds a squid inside the dielectric.

    """
    def __init__(self,
```

```
            fingers = 5,
            finger_length = 90,
            gap = 5,
            radius = 4,
            plate_width = 10,
            plate_heigth = 315,
            dielectric = 30, # thickness of surrounding dielectric layer
            pin = 12,
            layer = 1,
            add_skirt = False,
            skirt_distance = 5,
            skirt_layer = 91,
            name = 'interdigitated_cap'
           ):

    super(interdigitated_cap, self).__init__(name)
    cad.core.default_layer = layer
    self.width = gap + finger_length + 2*plate_width + 2*dielectric
    self.heigth = plate_heigth + 2*dielectric
    self.fingers = fingers
    self.dielectric = dielectric
    self.plate_width = plate_width
    self.gap = gap
    self.skirt = add_skirt
    self.skirt_layer = skirt_layer
    self.skirt_distance = skirt_distance

    # first make outerdielectric
    cell = cad.core.Cell('dielectric')
    dielec_h = dielectric + plate_heigth/2. - pin/2.
    dielec_w = 2*(dielectric + plate_width) + gap + finger_length
    contourpoints = [ (0, dielec_h ), (0,0), (dielec_w, 0),
        (dielec_w, dielec_h), (dielec_w-dielectric, dielec_h),\
                    (dielec_w-dielectric, dielectric),
                     (dielectric, dielectric), (dielectric, dielec_h) ]
    self.contourpoints = contourpoints
    self.dielec_w = dielec_w
    self.dielec_h = dielec_h

    lower_half = cad.core.Boundary( contourpoints )
    cell.add(lower_half)
    self.add(cell)
    self.add( cell, origin = (dielec_w, 2*dielec_h+pin), rotation = 180)
    # rotate lowerhalf and place above lowerhalf

    # generate intern dielectric
    finger_heigth = (plate_heigth - (2.*fingers-1.)*gap )/(2.*fingers)
    # heigth of metal fingers
    points = [[0,0]]
    sign = 1

    for i in range(0, 4*fingers-1):
```

```
            if i%2 == 0:
                if (i == 0 or i == 4*fingers-2):
                    add = [points[i][0], points[i][1] + finger_heigth + gap/2.]
                else:
                    add = [points[i][0], points[i][1] + finger_heigth + gap]
            if i%2 == 1:
                add = [points[i][0] + sign*finger_length,  points[i][1] ]
                sign = -1*sign
            points.append(add)

        inside = MeanderingLine(points, turn_radius = radius, line_width = gap)
        self.add( inside, (dielectric+plate_width+gap/2., dielectric) )

        if add_skirt == True:
            points = [(-skirt_distance, -skirt_distance), (-skirt_distance, self.heigth
                + skirt_distance), \
                      (self.width + skirt_distance, self.heigth + skirt_distance),
                  (self.width + skirt_distance, -skirt_distance)]
            skirt = cad.core.Boundary(points ,layer = skirt_layer)
            self.add(skirt)


    def add_squid(self, thickness=2, width=20, heigth=16):

        # remove lower dielectric
        if self.skirt == False:
            self.remove(self.elements[0])
        else:
            self.remove(self.elements[1])

        # generate squid
        squid = cad.core.Cell('squid')
        loop = cad.core.Boundary( [(-width/2., -heigth/2.), (-width/2., heigth/2.),
                (-1.5, heigth/2),
                                   (-1.5, heigth/2. + thickness/2. - 0.2), (-2.7, heigth/2.
                                   + thickness/2. -0.2),
                                   (-2.7, heigth/2. + thickness/2. + 0.2), (-1.5, heigth/2.
                                   + thickness/2 + 0.2),
                                   (-1.5, heigth/2. + thickness), (1.5, heigth/2.
                                   + thickness),
                                   (1.5, heigth/2. + thickness/2. + 0.2),
                                   (2.7, heigth/2. + thickness/2. + 0.2),
                                   (2.7, heigth/2. + thickness/2. - 0.2),
                                   (1.5, heigth/2. + thickness/2. - 0.2),
                                   (1.5, heigth/2.), (width/2., heigth/2.),
                                   (width/2., -heigth/2.), (1.5, -heigth/2),
                                   (1.5, -heigth/2. - thickness/2. + 0.2), (2.7,
                                   -heigth/2. - thickness/2. + 0.2),
                                   (2.7, -heigth/2. - thickness/2. - 0.2), (1.5, -heigth/2.
                                   - thickness/2 - 0.2),
                                   (1.5, -heigth/2. - thickness), (-1.5, -heigth/2.
                                   - thickness),
```

```
                                (-1.5, -heigth/2. - thickness/2. - 0.2), (-2.7, -heigth/2.
                                - thickness/2. - 0.2),
                                (-2.7, -heigth/2. - thickness/2. + 0.2), (-1.5, -heigth/2.
                                -thickness/2. + 0.2),
                                (-1.5, -heigth/2.)] )
        squid.add(loop)

        # create new dielectric for lower part
        lower_half = cad.core.Cell('lower_half')
        delta = self.plate_width - (thickness + (width-self.gap)/2.)
        self.delta = delta
        contourpoints = [ (0, self.dielec_h), (0, 67.5), (self.dielectric + delta-10,
            67.5), (self.dielectric + delta -10, 0),\
                        (self.dielec_w,0), (self.dielec_w, self.dielec_h),
                        (self.dielec_w - self.dielectric, self.dielec_h),\
                        (self.dielec_w - self.dielectric, self.dielectric),
                        (self.dielectric+2*thickness+width + delta, self.dielectric),\
                        (self.dielectric + 2*thickness+width+delta, self.dielectric
                        - 2*thickness - heigth), \
                         (self.dielectric + delta, self.dielectric -
                         2*thickness - heigth),\
                         (self.dielectric + delta, self.dielectric), (self.dielectric,
                         self.dielectric),
                         (self.dielectric, self.dielec_h)]

        contour = cad.core.Boundary(contourpoints)
        lower_half.add(contour)
        self.add(lower_half)
        self.add(squid, (self.dielectric+thickness+width/2. + delta, self.dielectric
        - thickness - heigth/2.))

        if self.skirt == True:
            self.remove(self.elements[0]) # remove old skirt
            thickness = self.skirt_distance
            points = [ ( self.dielectric + self.delta - 10 - thickness, 0),
                       ( self.dielectric + self.delta - 10 - thickness, 67.5-thickness),\
                       (-thickness, 67.5-thickness), (-thickness, self.heigth
                       + thickness), \
                       (self.width + thickness, self.heigth + thickness), (self.width
                       + thickness, -thickness),\
                       (self.dielectric + self.delta - 10 - thickness, -thickness)  ]
            skirt = cad.core.Boundary(points ,layer = self.skirt_layer)
            self.add(skirt)
```

B.2 Chip design

Below the script with the parametrized chip design.

```
import numpy as np
from stcad.source_dev.chip import Base_Chip
```

```
from stcad.source_dev.utilities import *
from stcad.source_dev import objects
from stcad.source_dev import groundplaneholes

import shapely
import gdsCAD as cad
import matplotlib.pyplot as plt
from shapely import geometry


def cpw_coor(start, coordinates, length, n_bends, turn_radius, direction = 's', ending = 'h'):
    """ This functions generates a list with points for the CPW object,
    such that we can set the total length.
    The starting  distance can be set seperately. When of this is set to 0, the beginning of
    the line will be  a bended open end, such that a tunable josephson junction can be added.
    The length specifies the total lenght, n_bends the number of bends and the turn_radius
    determines the curvature of a turn.  Finally, the direction specifies wheter the CPW
    starts in the north direction (n) or south direction (s) and the ending wheter the CPW
    should end horizontally (h) or vertically (v)
    """

    if direction == 's':
        direction = -1
    if direction == 'n':
        direction = 1

    n_bends_eff = n_bends + (start == 0)*0.5 + (ending == 'h')*0.5
    # number of bends including half bends at beginning and end
    delta_x = (coordinates[1][0] - coordinates[0][0])/(n_bends_eff*1.)
    # x-distance between a u-turn
    delta = coordinates[0][1] - coordinates[1][1];
    # y difference between begin and end point
    l_bend = np.pi*turn_radius + (delta_x-2*turn_radius)
    # length of one bend

    # this block calculates length of pieces of cpw except beginning and end pieces
    if direction* (-1)**(n_bends%2) < 0 : # approach final point from above
        if start == 0:
            length_straigth = ( length - n_bends_eff*l_bend - delta + \
            ((ending == 'h')+1)*turn_radius)/(n_bends + (1+direction)/2)
        else:
            length_straigth = ( length -(1+direction)*start - n_bends_eff*l_bend -\
            delta + (ending == 'h')*turn_radius)/(n_bends - (1+direction)/2)

    if direction* (-1)**(n_bends%2 ) > 0:
        if start == 0:
            corr = 1 + (1-direction)/2
            length_straigth = (length - 2*start - n_bends_eff*l_bend + delta +\
            ((ending == 'h')+1)*turn_radius)/(n_bends+(1-direction)/2 )
        else:
            length_straigth = (length - (1-direction)*start - n_bends_eff*l_bend +\
            delta +(start ==0)*turn_radius + (ending == 'h')*turn_radius)/(n_bends -\
```

```
            (1-direction)/2 )


    ## generate list with points
    # set starting direction
    if start == 0:
        sign = (-1)*direction
    else:
        sign = 1*direction

   # set first points, based on directions specified in outer distances
    if start == 0:
        points = [ [0,0], [ delta_x/2, 0 ] ]
        remainder = 1;  # this makes that in the next step the line goes down
    else:
        points = [ [0,0], [0,(start + turn_radius)*sign] ]
        remainder = 0 # this makes that in the next step the line goes right

    # calculate points in between
    for i in range(2, 2*n_bends + 1 + 1*(start==0)):
    # genereate points for all bends and straight lines
        if (i)%2 == remainder: # go in the x direction
            x = points[i-1][0] + delta_x
            y = points[i-1][1]
        if (i)%2 != remainder: # go in the y direction
            sign = sign*(-1)  # next time go other direction (n --> s or s --> n)
            x = points[i-1][0]
            y = points[i-1][1] + sign*(2*turn_radius+length_straigth)

        points.append( [x,y] )

    # add last point, based on distance specified in outer_distances
    if ending == 'v':
        points.append( [ coordinates[1][0] - coordinates[0][0], coordinates[1][1] -\
        coordinates[0][1]])
    elif ending == 'h':
        points.append( [ coordinates[1][0] - coordinates[0][0] - delta_x/2.,\
        coordinates[1][1] - coordinates[0][1]])
        points.append( [ coordinates[1][0] - coordinates[0][0], coordinates[1][1] - \
        coordinates[0][1]])
    return np.around(points, decimals =5)

## system parameters
path = '/home/tim/CloudStation/mep/chip_design/'
name = '7mm_4mm_5jj'

chipsize_x = 7e3
chipsize_y = 4e3
pin = 12
gap = 4
length = 9e3 # distance between junctions
turn_radius = 100
```

```
coup_gap = 12 # size of gap of outercapacitances

## cap properties
dielectric = 30
plate_heigth = 315
plate_width = 10
fingers = 8
finger_length = 90
cap_gap = 1
cap_heigth = plate_heigth + 2*dielectric
cap_width = finger_length + gap+ 2* plate_width + 2*dielectric

## launcher properties
bonding_pad_length = 100
bonding_pad_gap = 101
bonding_pad_width = 150
taper_length = 200
buffer_length = 0
input_length = 100
launcher_length = bonding_pad_length + taper_length

## fluxline properties
total_length = 60
flux_launcher_length =30
final_pad_width = 6
final_pad_gap = 23.5
cap_distance_x = 3.5
cap_distance_y = 6.5

#marker
marker_edge = 62.5
marker_mutual = 200
skirt_distance = 4

dic = {'junction_gap': 0.2, 'junction_finger_width': [0.01, 0.02], \
    'junction_finger_heigth': 0.2, 'contact_pad_width': 1.0,\
 'contact_pad_height': 2.0, 'contact_pad_overlap': 1.8, 'contact_distance': 3}

# coordinate of end of launchers
launcher_coor = [ (1029.85 - chipsize_x/2, chipsize_y/2 - launcher_length),
                  (0, chipsize_y/2 - launcher_length),
                  (5970.15 - chipsize_x/2, chipsize_y/2 - launcher_length),
                 (5970.15 - chipsize_x/2, -chipsize_y/2 + launcher_length),
                 (1029.85 - chipsize_x/2, -chipsize_y/2 + launcher_length),
                  (-chipsize_x/2 + launcher_length + 100, 100),
                  (chipsize_x/2 - launcher_length - 100, 100)
                 ]

# coordinate of caps
cap_coor = [(-1938, 1405),(-1029, -1416.174), (-120, 1405),  (789, -1416.174), (1698, 1400)]

cpw_coor = [ [ (launcher_coor[5][0], launcher_coor[5][1] + coup_gap), cap_coor[0]],
```

```
            [ (cap_coor[0][0] + cap_width, cap_coor[0][1]), cap_coor[1]],
            [ (cap_coor[1][0] + cap_width, cap_coor[1][1]), cap_coor[2]],
            [ (cap_coor[2][0] + cap_width, cap_coor[2][1]), cap_coor[3]],
            [ (cap_coor[3][0] + cap_width, cap_coor[3][1]), cap_coor[4]],
            [ (cap_coor[4][0] + cap_width, cap_coor[4][1]), (launcher_coor[6][0], \
            launcher_coor[6][1] + coup_gap)]
          ]
y_corr = 67.5-cap_distance_y-final_pad_width/2.-final_pad_gap
x_corr = total_length - dielectric + 10 + cap_distance_x

flux_coor = [ [ (0,0), (0,  cap_coor[0][1]- launcher_coor[0][1] + cap_heigth/2. -y_corr),\
               (cap_coor[0][0] - launcher_coor[0][0] -x_corr, cap_coor[0][1]-\
           launcher_coor[0][1] + cap_heigth/2. -y_corr ) ],
              [ (0,0), (0, cap_coor[2][1]- launcher_coor[1][1] + cap_heigth/2. +\
              total_length + cap_distance_x)],
              [ (0,0), ( 0, cap_coor[4][1]- launcher_coor[2][1] + \
                  cap_heigth/2. -y_corr),
              (cap_coor[4][0] - launcher_coor[2][0]  + x_corr + cap_width, cap_coor[4][1]\
          - launcher_coor[2][1] + cap_heigth/2. -y_corr )],
              [(0,0), (0, cap_coor[3][1]- launcher_coor[3][1] \
                  -cap_heigth/2. + y_corr),\
              ( cap_coor[3][0] -launcher_coor[3][0]  + x_corr + cap_width,\
          cap_coor[3][1]- launcher_coor[3][1] - cap_heigth/2. + y_corr)],
              [(0,0), (0, cap_coor[1][1]-\
                  launcher_coor[4][1] -cap_heigth/2. + y_corr),\
              (cap_coor[1][0] - launcher_coor[4][0]  -x_corr, cap_coor[1][1]- \
          launcher_coor[4][1] - cap_heigth/2. + y_corr)]
            ]

marker_coor =  [ (-chipsize_x/2 + marker_edge, chipsize_y/2 - marker_edge),
             (chipsize_x/2 - marker_edge, chipsize_y/2 - marker_edge),
             (chipsize_x/2 - marker_edge, -chipsize_y/2 + marker_edge),
             (-chipsize_x/2 + marker_edge, -chipsize_y/2 + marker_edge)]

chip = Base_Chip(name, chipsize_x, chipsize_y, label=False)

# create cpw with launchers
cpw_w = objects.CPW(  [ [0, 0],[0, -100], [-100, -100] ], pin = pin, gap = gap, \
turn_radius = turn_radius, layer = 1, name ='launcher_w')
cpw_w.add_launcher('e', bonding_pad_length, bonding_pad_gap, bonding_pad_width,\
taper_length ,buffer_length, add_skirt= True, skirt_distance=skirt_distance)
cpw_w.add_open('b', coup_gap, add_skirt=True, skirt_distance = skirt_distance)
cpw_w.add_mask(pin+2*gap+2*skirt_distance, layer=91)
chip.add( cpw_w,  launcher_coor[5])

cpw_e = objects.CPW( [ [0,0], [0, -100], [100,-100] ], pin = pin, gap = gap, turn_radius = \
turn_radius, layer = 1, name ='launcher_e')
cpw_e.add_launcher('e', bonding_pad_length, bonding_pad_gap, bonding_pad_width, taper_length ,\
buffer_length, add_skirt=True, skirt_distance=skirt_distance)
cpw_e.add_open('b', coup_gap, add_skirt=True, skirt_distance = skirt_distance)
cpw_e.add_mask(pin+2*gap+2*skirt_distance, layer=91)
chip.add( cpw_e,  launcher_coor[6])
```

```
density = [ 0.007, 0.023, 0.006, 0.002, 0.002]
flux_lines = []
for i in range(0,5):
    flux_lines.append(objects.CPW( flux_coor[i], pin = pin, gap = gap, \
    turn_radius = turn_radius, layer = 1, name ='launcher'))
    flux_lines[i].add_launcher('b', bonding_pad_length, bonding_pad_gap,\
    bonding_pad_width, taper_length ,buffer_length, add_skirt=True, \
skirt_distance=skirt_distance)
    flux_lines[i].add_flux_bias_short(total_length = total_length, launcher_length =\
        flux_launcher_length, final_pad_width = \
                                    final_pad_width, final_pad_gap = final_pad_gap, \
                                add_skirt= True, skirt_distance=skirt_distance)
    flux_lines[i].add_mask(pin+2*gap+2*skirt_distance)
    flux_lines[i].add_airbridges([40, 90], [66, 30], width = 30, density = density[i],\
    layers = [2,3])
    chip.add(flux_lines[i], launcher_coor[i])

# create cpw's
cpw = []
points= meander(1.2e3, [ cpw_coor[0][0], cpw_coor[0][1]], length, 4, turn_radius, \
direction = 'n', ending = 'h')
cpw.append(objects.CPW(points, pin = pin, gap = gap, turn_radius = turn_radius, \
layer = 1, name ='first'))
cpw[0].add_mask(pin+2*gap+2*skirt_distance,layer= 91)
cpw[0].add_airbridges([40, 90], [66, 30], width = 30, density = 0.002, layers = [2,3])
chip.add(cpw[0], cpw_coor[0][0])
print(cpw[0].length)

for i in range(len(cpw_coor) -2):
    if i%2 == 0:
        direction = 's'
    else:
        direction = 'n'
    points = meander(0, [ cpw_coor[i+1][0], cpw_coor[i+1][1]], length, 2, turn_radius,\
    direction = direction, ending = 'h')
    cpw.append(objects.CPW(points, pin = pin, gap = gap, turn_radius = turn_radius,\
    layer = 1))
    cpw[i+1].add_mask(pin+2*gap+2*skirt_distance, layer=91)
    cpw[i+1].add_airbridges([40, 90], [66, 30], width = 30, density=0.002, layers = [2,3])
    chip.add(cpw[i+1], cpw_coor[i+1][0])
    print(cpw[i+1].length)

points = meander(0, [ cpw_coor[5][0], cpw_coor[5][1]], length, 4, turn_radius, ending = 'v')
cpw.append( objects.CPW(points, pin = pin, gap = gap, turn_radius = turn_radius,\
layer = 1, name ='sixt') )
cpw[5].add_mask(pin+2*gap+2*skirt_distance, layer=91)
cpw[5].add_airbridges([40, 90], [66, 30], width = 30, density = 0.002, layers = [2,3])
chip.add(cpw[5], cpw_coor[5][0])
print(cpw[5].length)

# create transmons
```

```
angles = [0, 0, 180, 180, 180]
transmons = []
for i in range(0,5):
    transmons.append(objects.interdigitated_cap(fingers = fingers, \
            finger_length = finger_length, gap = cap_gap, plate_width = plate_width,\
            plate_heigth = plate_heigth,\
            dielectric = dielectric, layer = 1, name = 'interd', add_skirt= True,\
    skirt_distance=skirt_distance ))
    transmons[i].add_squid( width = 21, draw_junctions= True, \
    junction_dict = dic, angle = angles[i])

chip.add(transmons[0], origin = (cap_coor[0][0], cap_coor[0][1] + cap_heigth/2.),\
x_reflection = True)
chip.add(transmons[1], origin = (cap_coor[1][0], cap_coor[1][1] - cap_heigth/2.))
chip.add(transmons[2], origin = (cap_coor[2][0] + cap_width, cap_coor[2][1]+ cap_heigth/2.), \
rotation = 180)
chip.add(transmons[3], origin = (cap_coor[3][0] + cap_width, cap_coor[3][1]- cap_heigth/2.), \
rotation = 180, x_reflection = True)
chip.add(transmons[4], origin = (cap_coor[4][0] + cap_width, cap_coor[4][1]+ cap_heigth/2.),\
rotation = 180)


# add markers, mask around launchers and dielectric surrounding the chip
markers = cad.core.Cell('marker')
markers.add( cad.shapes.Rectangle((-10, -10), (10, 10), layer = 1 ) )
markers.add( cad.shapes.Rectangle((-10-marker_mutual, -10), (10-marker_mutual, 10),\
layer = 4 ))

for i in range(0,4):
    if i == 1 or i == 2:
        angle = 180
    else:
        angle = 0
    ref = cad.core.CellReference(markers, marker_coor[i], rotation = angle)
    chip.add(ref)

launcher_mask = cad.core.Boundary(((-chipsize_x/2 + bonding_pad_length, 0),
                                   (-chipsize_x/2 + bonding_pad_length, chipsize_y/2 - \
                                   bonding_pad_length),
                                   (chipsize_x/2 -  bonding_pad_length, chipsize_y/2 -\
                                   bonding_pad_length),
                                   (chipsize_x/2 -  bonding_pad_length, -chipsize_y/2 +\
                                   bonding_pad_length),
                                   (-chipsize_x/2 + bonding_pad_length, -chipsize_y/2 +\
                                   bonding_pad_length),
                                   (-chipsize_x/2 + bonding_pad_length, 0),
                                   (-chipsize_x/2, 0),
                                   (-chipsize_x/2, -chipsize_y/2),
                                   (chipsize_x/2, -chipsize_y/2),
                                   (chipsize_x/2, chipsize_y/2),
                                   (-chipsize_x/2, chipsize_y/2),
                                   (-chipsize_x/2, 0)), layer = 91)
```

```
cad.shapes.Box((-chipsize_x/2 + 0.5*bonding_pad_length, -chipsize_y/2 +\
    0.5*bonding_pad_length), (chipsize_x/2 - 0.5*bonding_pad_length, chipsize_y/2 - \
    0.5*bonding_pad_length),
                       width=100, layer =91)
chip.add(launcher_mask)
outer_dielec = cad.core.Boundary(((-chipsize_x/2, 0),
                                  (-chipsize_x/2, chipsize_y/2),\
                                  (chipsize_x/2, chipsize_y/2),\
                                  (chipsize_x/2, -chipsize_y/2),\
                                  (-chipsize_x/2, -chipsize_y/2),\
                                  (-chipsize_x/2, 0),\
                                  (-chipsize_x/2 - marker_mutual + marker_edge - 60, 0),\
                                  (-chipsize_x/2 - marker_mutual + marker_edge - 60, \
                                  -chipsize_y/2 - 25),\
                                  (chipsize_x/2 + marker_mutual - marker_edge + 60, \
                                  -chipsize_y/2 - 25),\
                                  (chipsize_x/2 + marker_mutual - marker_edge + 60, \
                                  chipsize_y/2 + 50),\
                                  (-chipsize_x/2 - marker_mutual + marker_edge - 60, \
                                  chipsize_y/2 + 50),\
                                  (-chipsize_x/2 - marker_mutual + marker_edge - 60, 0)),\
                               layer=1)
chip.add(outer_dielec)

#holey ground
groundplane = groundplaneholes.GroundPlaneHoles('holes', {'ydim': chipsize_y -150, 'xdim': \
chipsize_x -150, 'smallx': 70, 'smally' : 70, 'holes': [2., 2.], 'streets': [1., 1.]})
holes = groundplane.gen_full()
chip.add(holes)

chip.save_to_gds(show=False, save=True,loc=path)
```

Appendix C

Numerical instability

Close to jump-down frequency we sometimes observed a peak appearing in the phase of the upper branch , depending on the number of frequency steps and time step h. An example is shown in fig. C.1

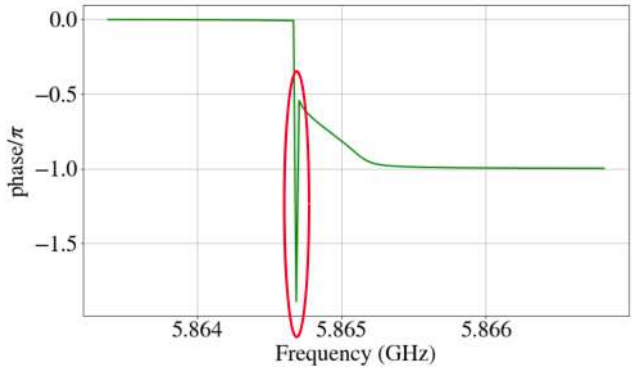

FIGURE C.1: Close to the jump-down frequency, we a peak appears in the steady-state phase of the upper branch, marked with a red circle. This is not always the case and depends on the number of frequency steps and time step.

We suspect this is because at the switching point it takes a long time for the model to converge. When we plot the phase of the peak as a function of time, shown in fig. C.2, we see that this indeed the case.

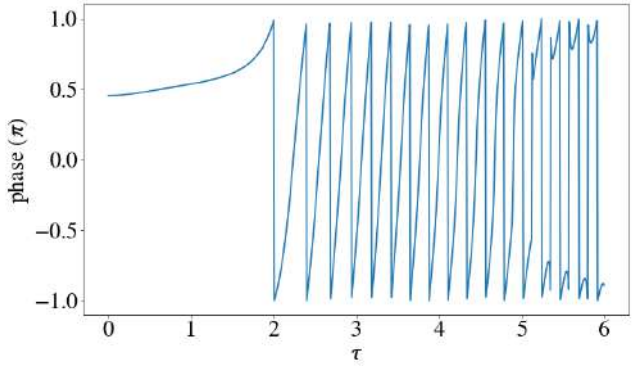

FIGURE C.2: Time trace of the peak marked by the red circle in fig. C.2 in units of the characteristic time $\tau = \frac{\tilde{Q}}{\pi f}$. The model does not converge, explaining the appearance of the peak in the steady-state plot.

For comparison, we plot the time traces in the van der Pol phase plane for the peak, and for a point just before the peak. Whereas the point just before peak converges, we see that time trace of the peak converges much slower and does not reach steady-state. Therefore, we removed the peaks for plotting purposes.

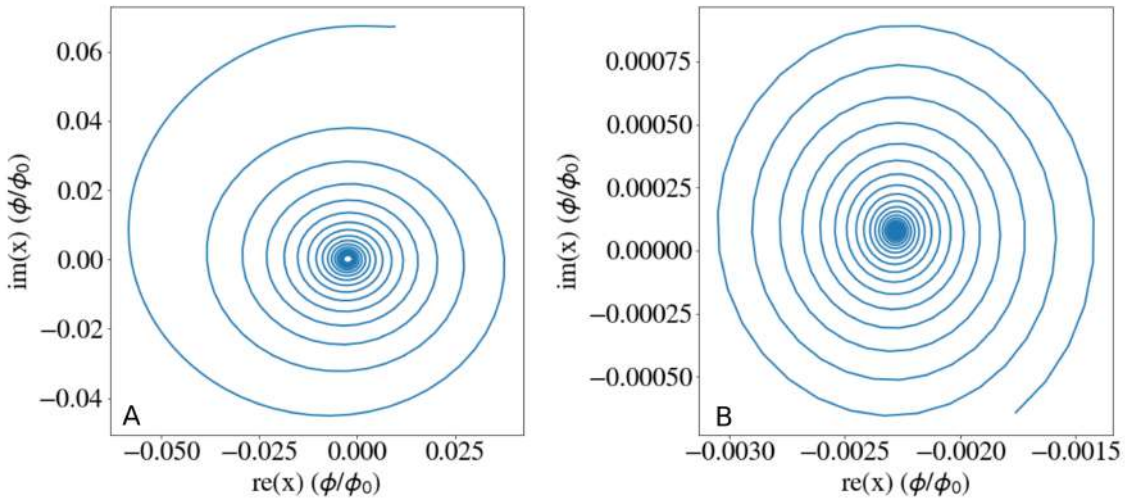

FIGURE C.3: **A** Time traces of the peak marked by the red circle in fig. C.2 plotted in the phase plane. The open circle in the middle indicates that it has not converged to steady-state yet. **B** Time trace of point point just before the peak. This point does converge to steady-state.

Appendix D

Peak in reflection parameters in classical non-linear model

Plotting the S_{11} parameters for the non-linear classical model of the one junction device, we observed the appearance of an extra peak both in the amplitude and the phase of the lower branch above the bifurcation point. This is shown in fig. D.1. We did not expect this, and in the following we trace back its origin.

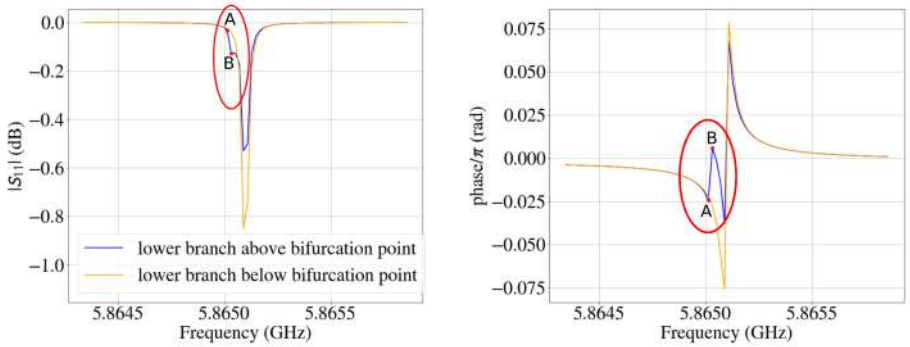

FIGURE D.1: S_{11} parameters below and above the bifurcation point ($P = -170\,\text{dBm}$ and $P = -149\,\text{dBm}$). Above the bifurcation point we observe a small second peak in the lower branch, marked with a red circle.

The S_{11} parameters were calculated using eq. (2.6) with $Z_0 = 50\,\Omega$. The impedance of the circuit Z is calculated as follows:

$$Z = \frac{V}{I} = \frac{\dot{\phi}_d}{I} = \frac{i\omega_d \Phi}{C_c\left(\ddot{\phi}_d - \ddot{\phi}_1\right)} = \frac{i\Phi}{C_c\omega_d\left(\frac{1}{2}(\phi_+ + \phi_-) - \Phi\right)} \tag{D.1}$$

In fig. D.2 we plot $\phi_1 = \frac{\phi_+ + \phi_-}{2}$ above the bifurcation point. We see the same peak appearing.

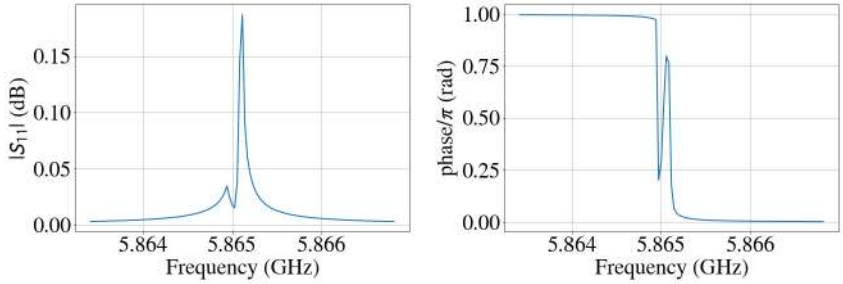

FIGURE D.2: ϕ_1 above the bifurcation point. The same peak is observed as with the reflection parameters.

As ϕ_1 is the sum of ϕ_+ and ϕ_-, we plot them separately, below and above the bifurcation point in fig. D.3 and fig. D.4.

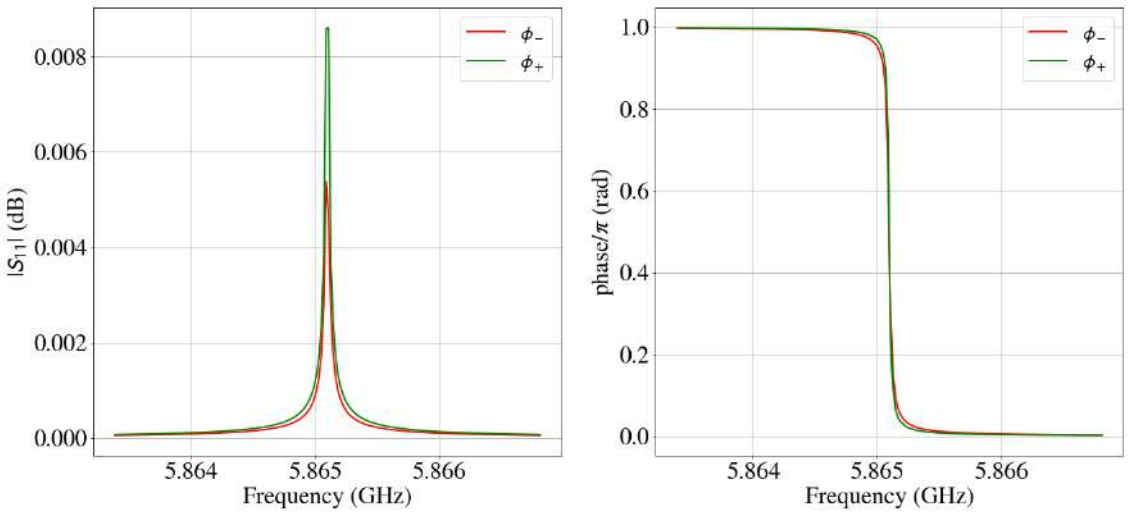

FIGURE D.3: Amplitude and phase of ϕ_+ and ϕ_- below the bifurcation point ($P = -170\,\mathrm{dBm}$). As expected for low powers, ϕ_- has the same shape as the harmonic solution.

Below the bifurcation point ϕ_- has the same shape as the harmonic solution ϕ_+. The only difference is its lower amplitude, as it has a weaker coupling to the drive.

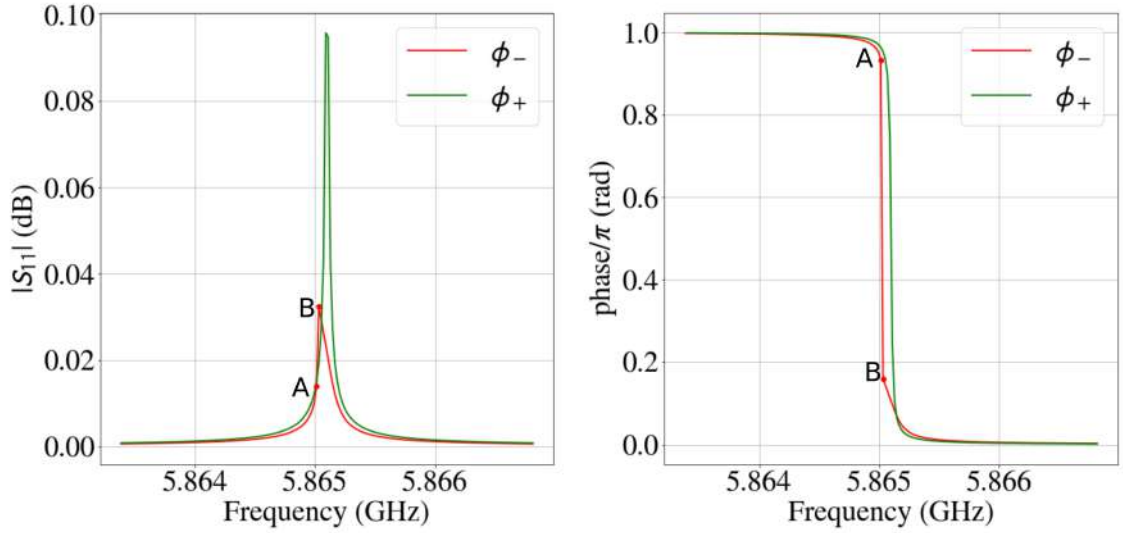

FIGURE D.4: Amplitude and phase of ϕ_+ and ϕ_-, above the bifurcation point ($P = -149\,\mathrm{dBm}$). Now ϕ_- starts to differ from the harmonic solution as its amplitude and phase are shifted to the left. This is the origin of the peak in the reflection parameters.

Above the bifurcation point however, ϕ_- starts to differ from ϕ_+ as both its amplitude and its phase get shifted to the left. So we can trace back the appearance of the peak in the S_{11} parameters to the distortion of ϕ_- at higher powers.

To test if the peak is numerically and converges to a steady-state value we plot the time trace of point B in the phase plane. This is shown in fig. D.5. We see this is indeed the case.

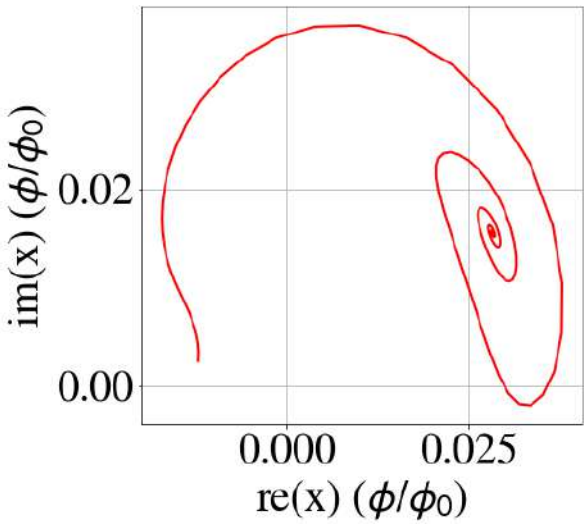

FIGURE D.5: Time trace plotted in phase plane of point B in fig. D.1. The trace converges to a steady-state value

In fig. D.6 we plot time traces of ϕ_- at the frequency of point A for different initial conditions, and compare it with point B. In red we show the time traces for the actual initial conditions leading to the steady-state values of points A and B. At A we see that some initial conditions lead to the low amplitude state L, and other to the high amplitude state U. From fig. 5.19 we know that the state marked by L belongs to the lower branch and the state marked by U belongs to the upper branch. At point B we were not able to find an initial conditions leading the steady-state L.

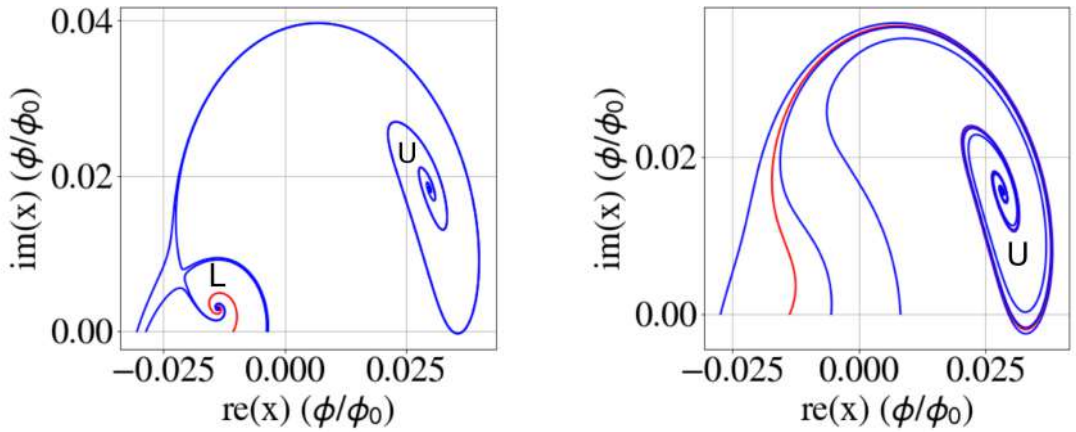

(A) (B)

FIGURE D.6: Time traces of point A and B in fig. D.1 (red) together with time traces with different initial conditions (blue). At point A all traces lead to U, and we were not able to find any condition leading to L.

This suggest that close to the peak , it is very difficult to stay at the low branch, as nearly all initial conditions lead to the upper branch.

Finally, we look at the effect of increasing the power, shown in fig. D.7.

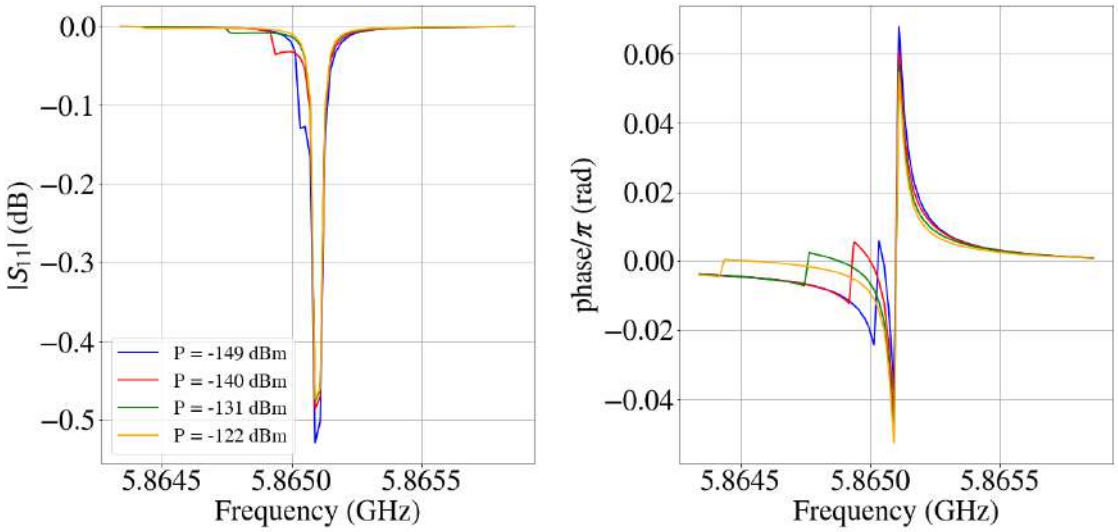

FIGURE D.7: Lower branch of ϕ_- for different powers above bifurcation point. The small peak shifts to the left and becomes shallower with increasing power.

We see that both in amplitude and phase the peak shifts to the left with increasing power, and becomes shallower.

Bibliography

[1] J.-M. Raimond and S. Haroche, *Exploring the quantum*. Oxford University Press, Oxford, 2006.

[2] K. J. Vahala, "Optical microcavities", *nature*, vol. 424, no. 6950, p. 839, 2003.

[3] R. Schoelkopf and S. Girvin, "Wiring up quantum systems", *Nature*, vol. 451, no. 7179, p. 664, 2008.

[4] R. Thompson, G. Rempe, and H. Kimble, "Observation of normal-mode splitting for an atom in an optical cavity", *Physical Review Letters*, vol. 68, no. 8, p. 1132, 1992.

[5] J.-M. Raimond, M. Brune, and S. Haroche, "Manipulating quantum entanglement with atoms and photons in a cavity", *Reviews of Modern Physics*, vol. 73, no. 3, p. 565, 2001.

[6] A. Wallraff, D. I. Schuster, A. Blais, L. Frunzio, R.-S. Huang, J. Majer, S. Kumar, S. M. Girvin, and R. J. Schoelkopf, "Strong coupling of a single photon to a superconducting qubit using circuit quantum electrodynamics", *Nature*, vol. 431, no. 7005, p. 162, 2004.

[7] J. You and F. Nori, "Atomic physics and quantum optics using superconducting circuits", *Nature*, vol. 474, no. 7353, p. 589, 2011.

[8] J. Clarke and A. I. Braginski, *The SQUID handbook: Applications of SQUIDs and SQUID systems*. John Wiley & Sons, 2006.

[9] M. Leib and M. J. Hartmann, "Synchronized switching in a josephson junction crystal", *Physical review letters*, vol. 112, no. 22, p. 223 603, 2014.

[10] D. M. Pozar, *Microwave engineering*, 2012.

[11] M. Riaziat, R. Majidi-Ahy, and I.-J. Feng, "Propagation modes and dispersion characteristics of coplanar waveguides", *IEEE Transactions on microwave theory and techniques*, vol. 38, no. 3, pp. 245–251, 1990.

[12] M. Göppl, A. Fragner, M. Baur, R. Bianchetti, S. Filipp, J. Fink, P. Leek, G. Puebla, L. Steffen, and A. Wallraff, "Coplanar waveguide resonators for circuit quantum electrodynamics", *Journal of Applied Physics*, vol. 104, no. 11, p. 113 904, 2008.

[13] R. Barends, "Photon-detecting superconducting resonators", PhD thesis, TU Delft, Delft University of Technology, 2009.

[14] R. E. Collin, *Foundations for microwave engineering*. John Wiley & Sons, 2007.

[15] M. Tinkham, *Introduction to superconductivity*. Courier Corporation, 2004.

[16] M. J. Hartmann, "Quantum simulation with interacting photons", *Journal of Optics*, vol. 18, no. 10, p. 104 005, 2016.

[17] M. Kounalakis *et al.*, "Modelling digital quantum simulation of the rabi model in circuit qed: Towards an experimental implementation of deep-strong coupling dynamics", Master's thesis, 2015.

[18] U. Vool and M. Devoret, "Introduction to quantum electromagnetic circuits", *International Journal of Circuit Theory and Applications*, vol. 45, no. 7, pp. 897–934, 2017.

[19] R. Feynman, R. Leighton, and M. Sands, *The Feynman Lectures on Physics*, ser. The Feynman Lectures on Physics v. 1. Addison-Wesley, 1963, ISBN: 9780201021165. [Online]. Available: https://books.google.nl/books?id=UtJEAAAAIAAJ.

[20] L. Novotny, "Strong coupling, energy splitting, and level crossings: A classical perspective", *American Journal of Physics*, vol. 78, no. 11, pp. 1199–1202, 2010.

[21] H. J. Korsch, H.-J. Jodl, and T. Hartmann, *Chaos: a program collection for the PC*. Springer Science & Business Media, 2007.

[22] D. W. Jordan and P. Smith, *Nonlinear ordinary differential equations: an introduction to dynamical systems*. Oxford University Press, USA, 1999, vol. 2.

[23] M. Brennan, I. Kovacic, A. Carrella, and T. Waters, "On the jump-up and jump-down frequencies of the duffing oscillator", *Journal of Sound and Vibration*, vol. 318, no. 4-5, pp. 1250–1261, 2008.

[24] J. Koch, M. Y. Terri, J. Gambetta, A. A. Houck, D. Schuster, J. Majer, A. Blais, M. H. Devoret, S. M. Girvin, and R. J. Schoelkopf, "Charge-insensitive qubit design derived from the cooper pair box", *Physical Review A*, vol. 76, no. 4, p. 042 319, 2007.

[25] S. Bader, "The transmon qubit", 2013.

[26] M. Born and V. Fock, "Beweis des adiabatensatzes", *Zeitschrift für Physik*, vol. 51, no. 3-4, pp. 165–180, 1928.

[27] D. J. Griffiths and D. F. Schroeter, *Introduction to quantum mechanics*. Cambridge University Press, 2018.

[28] P. Calabrese and J. Cardy, "Time dependence of correlation functions following a quantum quench", *Physical review letters*, vol. 96, no. 13, p. 136 801, 2006.

[29] E. Barouch, B. M. McCoy, and M. Dresden, "Statistical mechanics of the xy model. i", *Physical Review A*, vol. 2, no. 3, p. 1075, 1970.

[30] F. Iglói and H. Rieger, "Long-range correlations in the nonequilibrium quantum relaxation of a spin chain", *Physical review letters*, vol. 85, no. 15, p. 3233, 2000.

[31] A. Mitra, "Quantum quench dynamics", *Annual Review of Condensed Matter Physics*, vol. 9, pp. 245–259, 2018.

[32] M. Greiner, O. Mandel, T. Esslinger, T. W. Hänsch, and I. Bloch, "Quantum phase transition from a superfluid to a mott insulator in a gas of ultracold atoms", *nature*, vol. 415, no. 6867, p. 39, 2002.

[33] K. Sengupta, S. Powell, and S. Sachdev, "Quench dynamics across quantum critical points", *Physical Review A*, vol. 69, no. 5, p. 053 616, 2004.

[34] C. Kollath, A. M. Läuchli, and E. Altman, "Quench dynamics and nonequilibrium phase diagram of the bose-hubbard model", *Physical review letters*, vol. 98, no. 18, p. 180 601, 2007.

[35] R. Islam, R. Ma, P. M. Preiss, M. E. Tai, A. Lukin, M. Rispoli, and M. Greiner, "Measuring entanglement entropy in a quantum many-body system", *Nature*, vol. 528, no. 7580, p. 77, 2015.

[36] A. Polkovnikov, K. Sengupta, A. Silva, and M. Vengalattore, "Colloquium: Nonequilibrium dynamics of closed interacting quantum systems", *Reviews of Modern Physics*, vol. 83, no. 3, p. 863, 2011.

[37] M. Leib and M. J. Hartmann, "Bose–hubbard dynamics of polaritons in a chain of circuit quantum electrodynamics cavities", *New Journal of Physics*, vol. 12, no. 9, p. 093 031, 2010.

[38] A. A. Houck, H. E. Türeci, and J. Koch, "On-chip quantum simulation with superconducting circuits", *Nature Physics*, vol. 8, no. 4, p. 292, 2012.

[39] J. Eisert, M. Friesdorf, and C. Gogolin, "Quantum many-body systems out of equilibrium", *Nature Physics*, vol. 11, no. 2, p. 124, 2015.

[40] QUCS team, *Qucs*, 2017-02-22. [Online]. Available: `http://qucs.sourceforge.net/index.html`.

[41] X. Ma and W. Rhodes, "Squeezing in harmonic oscillators with time-dependent frequencies", *Physical Review A*, vol. 39, no. 4, p. 1941, 1989.

[42] M. Leib, "Many-body physics with circuit quantum electrodynamics", PhD thesis, Technische Universität München, 2015.

[43] A. G. Mark, *Gdscad (0.4.5)*, Feb. 15, 2015. [Online]. Available: `https://pythonhosted.org/gdsCAD`.

[44] Sonnet Software, Inc., *Sonnet (v. 14)*. [Online]. Available: `http://www.sonnetsoftware.com`.

[45] F. E. Schmidt, S. R. Peiter, M. F. Gely, T. van de Veen, and M. D. Jenkins, *Stcad*, Jul. 5, 2018. [Online]. Available: `https://github.com/feschmidt/stcad`.

[46] G. Dolan, "Offset masks for lift-off photoprocessing", *Applied Physics Letters*, vol. 31, no. 5, pp. 337–339, 1977.

[47] V. Ambegaokar and A. Baratoff, "Tunneling between superconductors", *Physical Review Letters*, vol. 10, no. 11, p. 486, 1963.

[48] C. Schuster and W. Fichtner, "Parasitic modes on printed circuit boards and their effects on emc and signal integrity", *IEEE Transactions on Electromagnetic compatibility*, vol. 43, no. 4, pp. 416–425, 2001.

[49] H.-J. Liaw and H. Merkelo, "Crossing the planes at high speed. signal integrity issues at split ground and power planes", *IEEE Circuits and Devices Magazine*, vol. 13, no. 6, pp. 22–26, 1997.

[50] R. Gross, A. Marx, and F. Deppe, *Applied Superconductivity: Josephson Effect and Superconducting Electronics*, ser. De Gruyter Textbook Series. Walter De Gruyter Incorporated, 2016, ISBN: 9783110417067.

[51] T. Van Duzer and C. W. Turner, "Principles of superconductive devices and circuits", 1981.

[52] M. Kounalakis, C. Dickel, A. Bruno, N. K. Langford, and G. A. Steele, "Tuneable hopping and nonlinear cross-kerr interactions in a high-coherence superconducting circuit", *npj Quantum Information*, vol. 4, no. 1, p. 38, 2018, ISSN: 2056-6387. DOI: `10.1038/s41534-018-0088-9`. [Online]. Available: `https://doi.org/10.1038/s41534-018-0088-9`.

[53] M. Gubrud, M. Ejrnaes, A. Berkley, R. Ramos, I. Jin, J. Anderson, A. Dragt, C. Lobb, and F. Wellstood, "Sub-gap leakage in nbalosub xnb and alalosub xal josephson junctions", *IEEE transactions on applied superconductivity*, vol. 11, no. 1, pp. 1002–1005, 2001.

[54] R. Barends, J. Wenner, M. Lenander, Y. Chen, R. C. Bialczak, J. Kelly, E. Lucero, P. O'Malley, M. Mariantoni, D. Sank, *et al.*, "Minimizing quasiparticle generation from stray infrared light in superconducting quantum circuits", *Applied Physics Letters*, vol. 99, no. 11, p. 113 507, 2011.

[55] R. Schouten. (2003). Measured b- and e-field in a room, [Online]. Available: `http://qtwork.tudelft.nl/~schouten/meas/fields.htm` (visited on 12/23/2018).

[56] M. Dykman and M. Krivoglaz, "Theory of fluctuational transitions between stable states of a nonlinear oscillator", *Sov. Phys. JETP*, vol. 50, no. 1, pp. 30–37, 1979.

[57] ——, "Fluctuations in nonlinear systems near bifurcations corresponding to the appearance of new stable states", *Physica A: Statistical Mechanics and its Applications*, vol. 104, no. 3, pp. 480–494, 1980.